A Segmented Model for Studying Water Transport in a PEM Fuel Cell

by

Yong-Song Chen

A dissertation submitted in partial fulfillment
of the requirements for the degree of
Doctor of Philosophy
(Mechanical Engineering)
in The University of Michigan
2009

Doctoral Committee:

Professor Huei Peng, Chair
Professor Levi T. Thompson, Jr.
Professor Jing Sun
Associate Professor Claus Borgnakke

To my parents

ACKNOWLEDGEMENTS

First and foremost I would like to express my appreciation to Professor Huei Peng for his advice and guidance. Without his support this study may not be done. I would like also express my gratitude to my committee members, Professors Levi Thompson, Jing Sun, and Claus Borgnakke for their invaluable comments and suggestions.

I would like to acknowledge National Science Foundation for the financial support (NSF0408664), Dr. B.J. Weng of the Chung-Shan Institute of Science and Technology, Taiwan, for manufacturing the fuel cell components, Mr. Rob Privette of Umicore for providing the membrane electrode assemblies, and Dr. Daniel Hussy and Dr. David Jacobson at the NIST for their technical support of neutron radiography experiments.

I also thank my fellow graduate students in Vehicle Dynamics Lab for their friendship and help, particularly to Jinming, Jing, Min-Joong, Youseok, Dangseok, Sean, Chiao-Ting, Changsun, and Zhenzhong. I appreciate the help and suggestions regarding my work from Jeongseok.

My special thanks also go to my parents and parents-in-law, who have been supportive for my study. I would also like to thank my sister Yu-Jong and her family for their love and support.

Last but not least, I would like to express my deepest thanks to my wife, Li-Wen, for her love, support, and encouragement and my lovely daughters, Shannon and Eileen, for the happiness they brought to my life.

TABLE OF CONTENTS

LIST OF FIGURES

LIST OF TABLES

ABSTRACT

A Segmented Model for Studying Water Transport in a PEM Fuel Cell

by

Yong-Song Chen

Chair: Huei Peng

Fuel Cells are devices that generate electricity by electrochemically combining hydrogen and oxygen. Water management plays an important role in the durability and efficiency of a proton exchange membrane fuel cell (PEMFC). In this study, single cells are modeled as lumped models consisting of 15 interconnected segments, which are linked according to the flow field patterns of the anode and cathode but they are treated as individual lumped elements. Parameters of this model were calibrated based on neutron radiography experimental results obtained at the NIST Center for Neutron Research (NCNR). Three special single cells were designed for the purpose of detecting liquid water and water vapor simultaneously. The major difference between our design and traditional flow field designs is the fact the anode channels and cathode channels were shifted sideways, so that the anode and cathode channels do not overlap in the majority of the active areas. The liquid water is measured by using neutron radiography. The water vapor is measured by the twenty relative humidity sensors embedded in the anode and the cathode flow field plates.

The effects of relative humidity and stoichiometry of cathode inlet on relative humidity distribution in the channels and on water accumulation in the GDLs were investigated in this study. The liquid water accumulation at steady-state was calculated by using imaging mask techniques and least-squares method. It is demonstrated that liquid water tends to accumulates in the gas diffusion layers under the rib. Modeling results suggest that opposite flow direction improve the cell performance at low humidity conditions. Accordingly, this segmented model is useful in designing flow field patterns and comparing the influence of different flow field patterns before they are machined on the flow field plates. That reduces the cost of developing and designing a fuel cell.

CHAPTER 1
BACKGROUND AND INTRODUCTION

Fuel Cells are devices that generate electricity by combining hydrogen and oxygen electrochemically. Because the efficiency of fuel cells is higher than the internal combustion engine and the only by-products are water and heat, fuel cells are considered as prominent power sources for the future. There are different types of fuel cells classified mainly by the type of the electrolyte used. They are proton exchange membrane fuel cells (PEMFCs), alkaline fuel cells (AFCs), phosphoric acid fuel cells (PAFCs), molten carbonate fuel cells (MCFCs), and solid oxide fuel cells (SOFCs). The operating temperature depends on the electrolyte used in the fuel cell. The applications of fuel cells can be classified into portable power, transportation, or stationary uses. Among the above five types of fuel cells, the PEMFC operating at low temperature has proved its potential for wide applications.

1.1 Principle of PEM Fuel Cells

A single PEMFC consists of a membrane electrode assembly (MEA), flow field plates with flow channels, current collectors, and end plates, as shown in Figure 1-1. The MEA is a polymer electrolyte membrane sandwiched between two electrodes. The macromolecules of the membrane material typically have a fluorocarbon backbone with a sulfonic acid group attached to it. Such material is an electrical insulator but a conductor for hydrogen ions. The electrodes are made of porous carbon paper or carbon cloth with a layer of carbon-supported platinum catalysts on the surface adjacent to the membrane. The porous carbon paper or carbon cloth ensures effective diffusion of the reactant gases to the catalyst layer, and is commonly referred as gas diffusion layer (GDL). The flow field plates guide the reactant gases throughout the active area and conduct current

generated by the reaction. The plates are often made of graphite or metal sheets, which are light-weight, gas impermeable, electron and thermal conducting, and corrosion resistant. The current collectors are made of gold-plated copper plates. End plates are typically made of aluminum alloy, chosen to compress MEAs, flow field plates and current collectors together precisely.

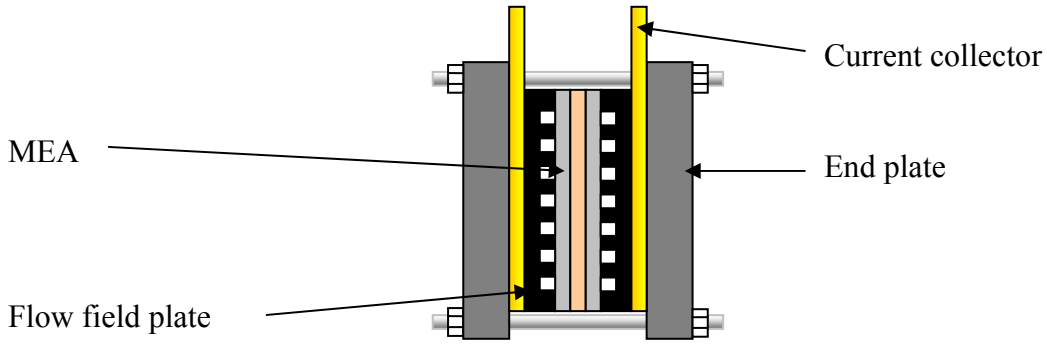

Figure 1-1: Schematic of PEM fuel cell.

During fuel cell operation, hydrogen is supplied through anode flow field. Hydrogen flows across the GDL and is decomposed into hydrogen ions and electrons by the Platinum catalyst.

$$2H_2 \rightarrow 4H^+ + 4e^- \tag{1.1}$$

The hydrogen ions go to the cathode side through the electrolyte, whereas electrons go through an external circuit. In the cathode, oxygen is combined with hydrogen ions and electrons catalytically to form water.

$$O_2 + 4H^+ + 4e^- \rightarrow 2H_2O \tag{1.2}$$

The overall reaction is then

$$2H_2 + O_2 \rightarrow 2H_2O \tag{1.3}$$

The schematic reaction of a fuel cell is shown in Figure 1-2. A fuel cell with only one MEA is called a single cell. Several single cells can be connected in series to form a fuel cell stack. In the stack, a flow field plate serves as the anode flow field of one MEA and as the cathode flow field of next MEA. The number of cells in one fuel cell stack varies depending on the power requirement of the applications.

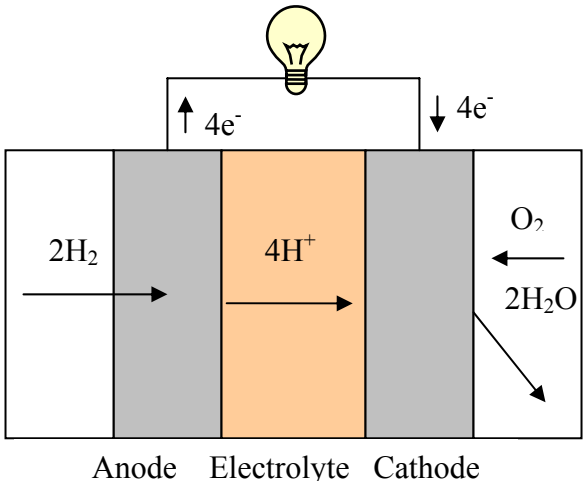

Figure 1-2: Schematic of fuel cell reaction.

PEMFCs convert chemical energy to electrical energy directly, so they have higher efficiency when compared to heat engines. Ideally, the maximum amount of electrical energy that can be obtained from a fuel cell during the chemical reaction equals the change in the Gibbs free energy. However, this is available when the cell operates under no electrical load. When there is an electrical load, the energy loss associated with the reaction lowers the overall efficiency of the fuel cell.

The power loss of a fuel cell can be represented by a polarization curve to characterize the relationship between the cell voltage and current density under different operating conditions. Parameters that significantly influence fuel cell operations include pressures of the reactant gases, relative humidity of reactant gases, and fuel cell temperature.

The typical polarization curve of a fuel cell, as shown in Figure 1-3, can be divided into three regions. Each of these regions is dominated by different overpotentials. There are three types of overpotentials: activation overpotential, ohmic overpotential and concentration overpotential. The activation overpotential is a result of the energy needed for breaking chemical bonds at the anode, transferring electrons, and reforming them into water at the cathode. The ohmic overpotential is due to the resistance of the polymer membrane to the transfer of protons and the resistance of the electrodes and the collector plates to the transfer of electrons. The concentration overpotential is caused by the

inadequate concentration of the reactant gases as they are consumed in the reaction. The combination of these three overpotentials affects the overall fuel cell efficiency.

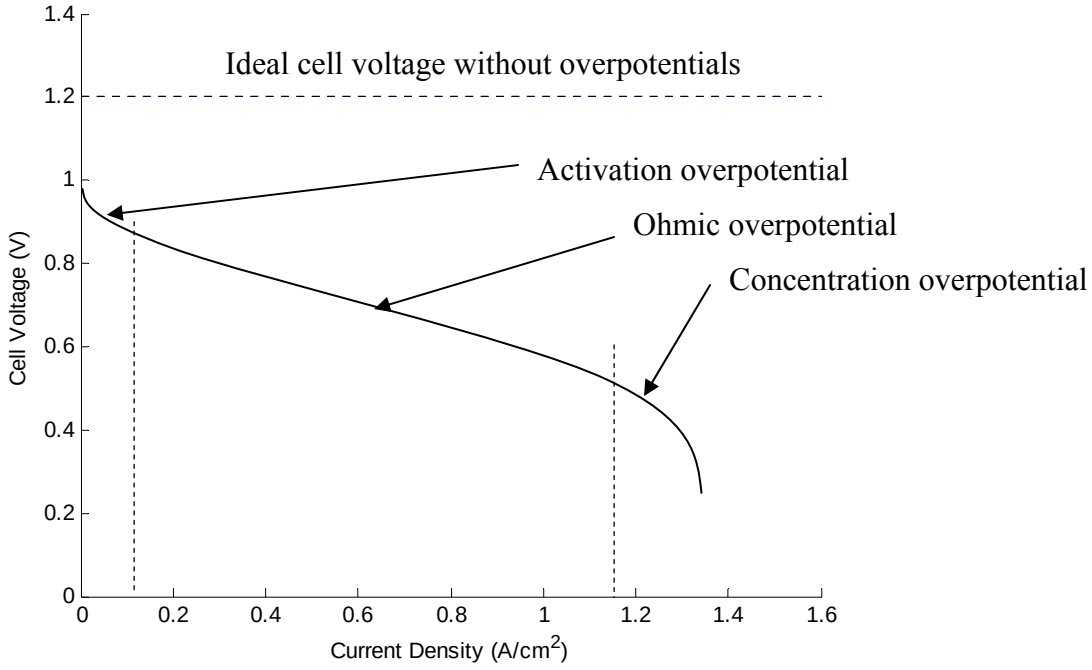

Figure 1-3: Typical polarization curve of a fuel cell.

To maintain high efficiency, a fuel cell usually works in the ohmic overpotential region. In this region, the membrane resistance is the major ohmic resistance and varies with water content in the membrane. The flow rate and the relative humidity of reactant affect the humidity of membrane. Dry membrane results in low membrane conductivity; however, too much water in the fuel cell causes flooding and high overpotential. Therefore, water management is an important issue in controlling a fuel cell and a model that can describe influence of water on cell performance is needed.

1.2 Literature Review

The performance of a PEMFC is determined by cell design and operating conditions. For cell design, the flow field pattern in the bipolar plates plays an important role in distributing reactant and removing generated water. For operating conditions,

relative humidity of reactants is considered one of the key factors that affect membrane hydration level.

Existing research related to PEMFCs can be divided into four areas: modeling of fuel cell performance, experiments about water transport, dynamic fuel cell models, and flow field design. The following sections provide a brief review on each of these areas.

1.2.1 Modeling of Fuel Cell Performance

Many factors influence the performance of proton exchange membrane fuel cells (PEMFCs), including membrane material and thickness, platinum loading, flow field designs, temperature, reactant partial pressure, etc. In addition, a critical issue that has severely limited the application of PEMFC is its poor reliability under cyclic temperature and humidity operations. An important factor that influences both the nominal performance and life under transient loading is the water accumulation and distribution in a PEMFC. When the fuel cell has too little or too much water, both performance and reliability suffers. Water accumulation also influences the warm-up and shut-down procedure for PEMFC that need to work in below-freezing temperature. It is fair to say that in addition to the cost issue, water management is one of the most important remaining issues for the adoption of PEMFC. Many models have been developed over the past several years for the water/humidity behavior inside a PEMFC.

Bernardi and Verbrugge [1, 2] developed one of the early mathematical models. They developed a steady-state, one-dimensional model which described the reactant transports in gas diffusion layer and water balance in PEMFCs. The membrane in their model was assumed fully hydrated, which is far from the real operation of PEMFCs. Okada et al. [3] used analytical approach to get the water concentration profiles in the membrane. Marr et al. [4] developed a model to investigate the catalyst utilization of the cathode, including the electrochemical reaction and mass transport process.Springer et al. [5] developed a model with partially hydrated membrane. They empirically related the membrane conductivity to the water content in Nafion membrane. Many of the subsequently developed models used the relation to determine the conductivity of the Nafion membrane. Fuller and Newman [6] developed a two-dimensional model to discuss water management, thermal management and fuel utilization in a PEMFC. Gurau

et al. [7] developed a two-dimension model which discussed reactant concentrations in the through-MEA direction and along the flow channel direction. Wang et al. [8] and Um et al. [9] developed models based on computational fluid dynamics (CFD) and solved the equations numerically. Um et al. [10] also extended their work to a three-dimensional model to study the performance of an interdigitated flow field design. Their results show that forced convection of gases through GDL helps to improve performance at high current densities. None of the models discussed above considered the effect of water accumulation on cell performance.

Starting from around the turn of the century, models that include the water/humidity behavior start to appear in the literature. Baschuk et al. [11] developed a model with the effect of variable degree of water flooding in the cathode catalyst layer and the cathode GDL on cell performance. Wang et al. [12] developed a model which handles the situation where two-phase flow exists in the cathode. Pasaogullari et al. [13] applied the two-phase flow model in the cathode GDL and investigated the effect of liquid saturation on cell performance. Wang [12] and Pasaogullari [13] related capillary pressure with the Leveretts function. The two-phase flow model successfully described water vapor distribution and liquid water accumulation in the GDL and in the flow channel.

Natarajan et al. [14] from the University of Kansas proposed a model that included the effect of water accumulation in the GDL under the rib and under the channel on cell performance. In their model, instead of using the Leveretts function, they suggested another empirical equation to describe the capillary pressure. Later, the same group [15, 16] further simplified capillary pressure gradient in their models as a constant. Their results showed significant difference with studies using the Leveretts function. Thus, experimental data that clearly describe water accumulation in the GDL, for both along the flow direction and across the GDL direction is needed. Recently, several studies used neutron radiography to detect liquid water distribution in PEMFCs [17, 18]. Neutron images showed that significant amount of liquid water could accumulate in the GDL under the channel ribs. Most of above models focus on water accumulation in the GDL under the channel and the developed formula do not apply readily to the subspace

under the ribs. Water distribution in the GDL under the ribs as well as under the flow channels should be considered and will be included in our model.

Because the reactant concentration varies along the flow channels, it causes variations in current density, water content, and temperature [19-21]. Therefore, the water generation and distribution in a PEMFC is not uniform. In addition, different anode and cathode flow field patterns were designed for different applications or working conditions [22]. Many CFD models have difficulties simulating PEMFCs with complex flow fields due to requirement of heavy computation load. Currently published CFD models simulate the reaction either in a straight flow channel or in a simple flow field. Lumped models [23-25] commonly assume a uniform reaction within fuel cells and do not consider the spatial distribution of reactants. Therefore, pure CFD models or pure lumped models may not be the best modeling choice.

1.2.2 Water Transport Experiments

Achieving and maintaining proper water balance at all load levels are critical for optimal performance of PEMFCs. Conducting experiments to measure water distribution inside an operating PEMFC is non-trivial because these experiments need special facilities. The water vapor in the flow channels can be measured by relative humidity sensors. Nishikawa et al. [26] used a relative humidity (RH) sensor to measure RH along the cathode flow channels. However, RH sensors can measure water vapor but not liquid water. In addition, a major issue with relative humidity sensors is the fact when they are exposed to a near-saturated gas, the reading saturates and even when it is subsequently exposed to under-saturated gases, the sensor reading may stay saturated for up to several minutes. Since it is desirable to operate a PEMFC near saturated condition, RH sensor alone is not a good solution. Mench et al. [27] measured the in-situ water vapor distribution in a working PEMFC by using gas chromatography. These methods can detect water vapor in the flow channels only. However, in a working fuel cell, liquid water is generated in the cathode catalyst layer of the cell due to chemical reaction. And it is mainly the liquid water in the GDL that affects cell performance through catalyst and flow blockage. Therefore, it is more important to measure liquid water accurately than to measure water vapor.

Tüber et al. [28] designed a fuel cell with its cathode covered by transparent plexiglass to observe the liquid water in the flow channels. They used a digital camera to record the images of liquid water generated in the cathode side of flow channels. However, this optical method cannot observe the liquid water in the GDL and quantifying liquid water accurately is also a challenge.

Neutron radiography techniques have been used for an in-situ and non-destructive visualization and measurement technique for liquid water in working fuel cells [29- 39] because neutron transmissibility is sensitive to hydrogen, which is an element of water molecular. Bellows et al. [29] used neutron radiography to measure water transport profiles across membrane in a working fuel cell. The cell in their experiments had a membrane thickness of 500 μm, which enabled visualizing the through-plane water profile across the membrane. Bellows' results showed that the water content in the membrane varied with operating conditions, but no significant water gradient across the membrane was observed. Using the same neutron facility, Satija et al. [30] demonstrated the use of neutron radiography to observe water distribution inside the fuel cell. A four-cell commercial stack was used in their study. An image-masking technique was used to isolate water formation in the anode channels, the cathode channels, and the gas diffusion layer (GDL). However, due to the multi-cell stack and overlap of anode channels and cathode channels, it was not easy to differentiate water in the anode side from that in the cathode side.

Kramer et al. [31, 32] applied statistical methods, including interpretation of the probability density function of the relative neutron transmission, to quantify the liquid water volume in an operating PEMFC and a direct methanol fuel cell (DMFC) and to compare serpentine and interdigitated flow field designs. Pekula et al. [33] used a facility at the Pennsylvania State University to obtain neutron images. Liquid droplets were observed in the final two-thirds of the flow field at higher current densities, and mostly in the corners. The liquid droplet velocity was not constant due to interactions with the channel walls and other droplets. Chuang et al. [34] quantified liquid water in the GDLs and flow channels of PEMFCs under both flooded and non-flooded conditions. Their results show that cell performance was affected by a few tenths of a milligram of liquid water in the fuel cell. Turhan et al. [17] conducted neutron imaging experiments to study

the influence of operating parameters on the liquid water distribution and accumulation. Their results indicated that liquid water accumulation in the fuel cell decreases with increasing gas flow rate of inlet. Ludlow et al. [35] also used neutron radiography to quantify the liquid water within an operating fuel cell under various gas flow conditions.

Geiger et al. [36] used neutron radiography to observe liquid water distribution in a PEMFC after it was shut down and cooled to ambient temperature. The liquid water was observed to accumulate in the bottom part of the flow field. Zhang et al. [18] studied the impact of GDL materials on liquid water accumulation inside a PEMFC.

Many researchers used the neutron imaging facility in the National Institute of Standards and Technology (NIST) to investigate the water content in an operating fuel cell. Trabold et al. [37] discussed the water accumulation in a serpentine flow field and the effects of current density and cathode stoichiometry on water accumulation. Owejan et al. [38] used a fuel cell with an interdigitated cathode flow field to study the effect of cathode inlet RH on water accumulation. Hickner et al. [39] focused on the transient behavior of liquid water transport inside a PEMFC and effect of local heating on the accumulation and distribution of liquid water.

These earlier studies [29-39] captured neutron images when fuel cells were at steady-state conditions and they mostly used fuel cells that have overlapped and identical anode and cathode flow fields, making it difficult to differentiate liquid water between anode and cathode in neutron images. It is known that the reaction in the cathode side is considered the rate determining step because of the slow kinetics of oxygen reduction. Liquid water in the channels does not influence cell performance unless the channel is filled with liquid water. It is the liquid water accumulation in the cathode catalyst layer or in the cathode GDL that could impede mass-transfer of oxygen. Pasaogullari [13] and Djilali [14] proposed different mechanisms of liquid water transport in the GDL. However, their hypotheses described the GDL under the channels without considering the GDL under the ribs. Turhan's [17] and Zhang's [18] studies showed that more liquid water accumulates in the GDL under the rib than in the GDL under the channel. Thus, the influence of liquid water in the GDL under the rib cannot be neglected. We will design single cells and conduct neutron radiography experiment to differentiate liquid water in different locations and use the results to calibrate our fuel cell model.

1.2.3 Dynamic Fuel Cell Models

Different from steady-state models, dynamic fuel cell models are usually control oriented. Amphlett et al. [23] developed a transient PEMFC model based on coupling the steady-state electrochemical model with a transient thermal model to predict the performance and heat loss of a fuel cell stack. Their model did not consider the water transport within the fuel cell stack. Pukrushpan et al. [24] developed a nonlinear dynamic model using electrochemical, thermodynamic, and fluid flow principles. Their model was used to analyze and design an air flow controller for a PEMFC stack. However, Pukrushpan's [40] model does not consider the effects of GDL. Shan et al. [25] used a one-Dimensional single-phase model to represent the dynamics present in the GDL. Ceraolo et al. [41] used partial differential equations to describe both static and dynamic behaviors of a PEMFC. Pathapati et al. [42] considered the effects of charge double layer capacitance, dynamics of flow, and mass/heat transfer transient features in the fuel cell to develop a dynamic model. Their model can predict the transient behavior of cell voltage, temperature, reactant flow rates and pressure under a load change.

The above dynamic fuel cell models are lumped models, which assume uniform reactions within the fuel cells and do not consider the spatial distribution of reactants. Golbert el al. [43] developed a dynamic fuel cell model, which accounts for spatial dependencies of voltage, current, reactant flows, and temperatures in the flow channel. However, their model can only describe the transient behavior within a single straight flow channel. In practical, the fuel cell performance and water distribution depend on flow field design, and water distribution inside fuel cells is an important issue. So far, we are not aware of any model that can describe the distributed properties of a single cell.

1.2.4 Flow Field Designs

PEMFC stacks are constructed with multiple cells connected by bipolar plates. Bipolar plates account for the major volume and weight of a PEMFC stack. They play the roles of constructing a PEMFC stack, separating individual cells, conducting electrons, distributing reactants, and expelling generated liquid water. The power density of a PEMFC can be significantly influenced by the flow patterns on the bipolar plates. Appropriate flow field design can increase the power density and improve water and heat

management. In some designs, cooling channels are integrated on the bipolar plates [44, 45]. Thus, the flow field pattern on the bipolar plates is an important factor in designing a PEMFC stack.

Common flow field pattern includes parallel, serpentine, interdigitated as well as their combinations. Many studies have compared the performance of fuel cells with different flow field designs. Aricò et al. [46] conducted an experiment to compare the influence of flow field design on direct methanol fuel cell. Dohle et al. [47] and Bewer et al. [48, 49] also investigated the influence of flow field design on the performance of PEMFCs and DMFCs. They concluded that flow distribution and power density were influenced by flow fields.

Kumar and Reddy [50] developed a three dimensional single phase isothermal model to describe the steady-state and transient response of four PEMFCs with different flow field designs, including serpentine, parallel, multi-parallel, and interdigitated types. Their modeling results showed that transient responses of serpentine and parallel designs were faster but performances were lower than the other two designs. However, Kumar's study did not consider water accumulation in the GDLs and due to heavy computational method, their model was not able to simulate PEMFCs with different anode and cathode flow field designs.

1.3 Motivation and Tasks

From the background introduction above, we clearly see the importance of understanding the membrane humidity phenomenon of PEMFCs. Unfortunately, due to the lack of reliable sensors and comprehensive models, membrane humidity modeling and control remain to be a weak link in fuel cell research. The development of an accurate humidity/thermal model is challenging because (i) the difficulty in placing humidity sensors inside the cell to verify model validity; (ii) the highly-coupled nature of humidity and temperature; (iii) the constant generation of product water due to the fuel cell reaction; and (iv) the process of water transport across the fuel cell membrane was poorly understood.

Water distribution inside a fuel cell is affected by the flow field patterns of the anode and cathode. From the literature review, we learned that both CFD model and lumped models were not able to describe the performance or the dynamic phenomena in a fuel cell with complicated flow field patterns. Besides, most fuel cell models do not consider the rib effect on water accumulation in the GDLs. Thus, a mathematical model that can predict water accumulation in the GDL under the ribs and can be applied on practical fuel cell is needed.

In this research both experimental and analytical studies for the water generation and transport phenomena inside a single-cell fuel cell were conducted. A steady-state, segmented mathematical model describing the distribution of humidity and current density was developed. The active area is divided into 15 segments according to the flow field designs. This model approach allows the distribution of current, water, and RH to be investigated more accurately. The segment model contains 6 sub-models, which are the cathode/anode channel model, the cathode/anode gas diffusion layer model, the membrane hydration model, and the segment voltage model. This model will then be used for analysis and control for improved water management of fuel cells.

Three single cells with different flow fields were designed and fabricated. These fuel cells are embedded with relative humidity (RH) sensors to detect the relative humidity within the flow channels. In addition, neutron radiography experiments conducted at the National Institute of Standards and Technology (NIST) visualized and quantified the liquid water within the fuel cells. The experimental data from RH sensors and neutron radiography was used to calibrate and validate the fuel cell model.

The segmented model in this studied will provide distributed characteristics of current density, water content in the membrane, relative humidity in the flow channel, and water accumulation in the GDLs. These distributed results provide useful information of a working fuel cell. That information tells which part of the cell is drying and which part of the cell is flooding and helps improve the flow field design.

1.4 Contributions

The major achievements of this study are summarized below:

- A segmented PEMFC model was developed. This model mainly captures the distributions of current density, water accumulation in the GDL both under the ribs and under the channels, water content in the membrane, and relative humidity in the flow channels.
- The modeling results provide information of drying and flooding levels of a fuel cell. By reconnecting the segments of this model, it predicts those distributed properties and performance of a single cell with complicated flow field patterns and helps improve the design of flow field patterns
- Conducted neutron radiography experiments for three single cells at the NIST. By applying the least-squares method, the average liquid water thicknesses in the GDL under the channel, in the GDL under the ribs, and in the channels can be calculated. In this study, both steady-state and transient behaviors of water accumulation were studied at different cathode inlet conditions.
- Compared the influence of flow field designs on cell performance and water accumulation with calibrated model and provided suggestion of designing flow field patterns.

CHAPTER 2
SEGMENTED FUEL CELL MODEL

As discussed in Chapter 1, most models that use partial differential equations cannot be easily applied to describe complicated flow fields, and lumped models that assume uniform reaction throughout the active area cannot present distributed properties accurately. In order to understand the details of water distribution, this study takes the advantages of lumped models to develop a steady-state model obtained from simplified two-dimensional mathematical equations; the model describes the distribution of water humidity and current density. The liquid water distribution model was developed according to the neutron experimental data discussed in Chapter 3.

2.1 Lumped Segments in a Single Cell

To capture distributed characteristics of a PEMFC, the active area is divided into fifteen segments that are connected according to flow fields, as shown in Figure 2-1. Each segment is viewed as a small lumped model, i.e. reactant/membrane properties and reaction in each segment are assumed to be uniform. The segments are connected together based on the flow direction of the reactants. Since each is regarded as a lumped model, it cannot account for the rib effects on gas transport. However, we will introduce semi-empirical correlation to describe the rib effects on water accumulation.

The inputs of a segment are the outputs of the preceding segments. For the overall cell, input variables are stoichiometry value, relative humidity (RH), and temperatures of the inflow gas and cell temperature. In order to simplify our model, we make assumptions as the following:

1. The model describes steady-state conditions.
2. The ideal gas law was employed for gas mixture.

3. Temperature throughout the single cell is uniformly distributed.
4. Chemical reaction throughout the segment is uniform.
5. Rib effects on gas transport and gas transport in the flow channel direction are neglected. Only gas transport through the MEA direction is considered in each segment.

According to the experiment of Wang et al. [51], temperature difference between upper stream and down stream is less than 2 °C when cell current density is 0.74 A cm^{-2}. In addition, our experiments also showed uniformly distributed temperature in a single cell, which will be discussed in Chapter 3; thus, all segment temperatures are assumed to be constant and the same as operating temperature.

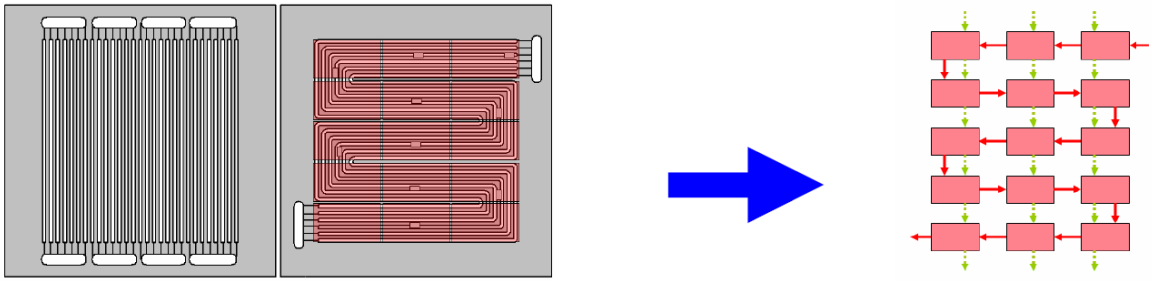

Figure 2-1: Schematic of a single cell modeled as several small segments

Based on the desired cell current and operating conditions, the molar flow rates of inflow hydrogen and oxygen for a single cell are evaluated, respectively as

$$N_{\mathrm{an,H_2,in}} = \frac{I_{\mathrm{cell}}}{2F}\zeta_{\mathrm{an}} \tag{2.1}$$

$$N_{\mathrm{ca,O_2,in}} = \frac{I_{\mathrm{cell}}}{4F}\zeta_{\mathrm{ca}} \tag{2.2}$$

where N is the molar flow rate in mol s^{-1}, I_{cell} is the cell current, ζ_{an} and ζ_{ca} are stoichiometry of anode and cathode, respectively, and F is the Faraday constant. The Nomenclature for the variables used in this study is shown in the Appendix.

If air is used as the cathode reactant, the nitrogen molar flow rate is calculated from

$$N_{\mathrm{ca,N_2,in}} = N_{\mathrm{ca,O_2,in}} \frac{1 - y_{\mathrm{O_2}}}{y_{\mathrm{O_2}}} \tag{2.3}$$

where y_{O_2} is the percentage of oxygen in the air. For an operating condition at selected inlet relative humidity φ and pressure P, the inlet vapor molar fraction can be calculated from

$$x_{\text{an,v,in}} = \frac{\varphi_{\text{an,in}} P_{\text{v,sat}}}{P_{\text{an,in}}} \tag{2.4}$$

$$x_{\text{ca,v,in}} = \frac{\varphi_{\text{ca,in}} P_{\text{v,sat}}}{P_{\text{ca,in}}} \tag{2.5}$$

where $P_{\text{v,sat}}$ is the saturated vapor pressure, which is a function of temperature. The value of $P_{\text{v,sat}}$ can be found in the thermodynamics table [52], or calculated from the following equation, given in [5]:

$$P_{\text{v,sat}} = 1.013 \times 10^5 \times 10^{\left[-2.1794+0.02953 T_{\text{seg}} - 9.1837\times10^{-5} T_{\text{seg}}^2 + 1.4454\times10^{-7} T_{\text{seg}}^3\right]} \tag{2.6}$$

The inlet water molar flow rate can then be calculated from

$$N_{\text{an,w,in}} = \frac{x_{\text{an,v,in}}}{1 - x_{\text{an,v,in}}} N_{\text{an,H}_2\text{,in}} \tag{2.7}$$

$$N_{\text{ca,w,in}} = \frac{x_{\text{ca,v,in}}}{1 - x_{\text{ca,v,in}}} \left(N_{\text{ca,O}_2\text{,in}} + N_{\text{ca,N}_2\text{,in}} \right) \tag{2.8}$$

Equations (2.1) - (2.8) describe the required amount of inflow species. After fed into the first segment of a fuel cell, gases flow through each segment based on the flow fields of anode and cathode to the subsequent segment.

Species flow in each segment is shown in Figure 2-2. Each segment itself consists of six interacting sub-models: cathode flow channel, anode flow channel, cathode GDL, anode GDL, membrane hydration, and segment voltage. Theses models will be described in the following sections.

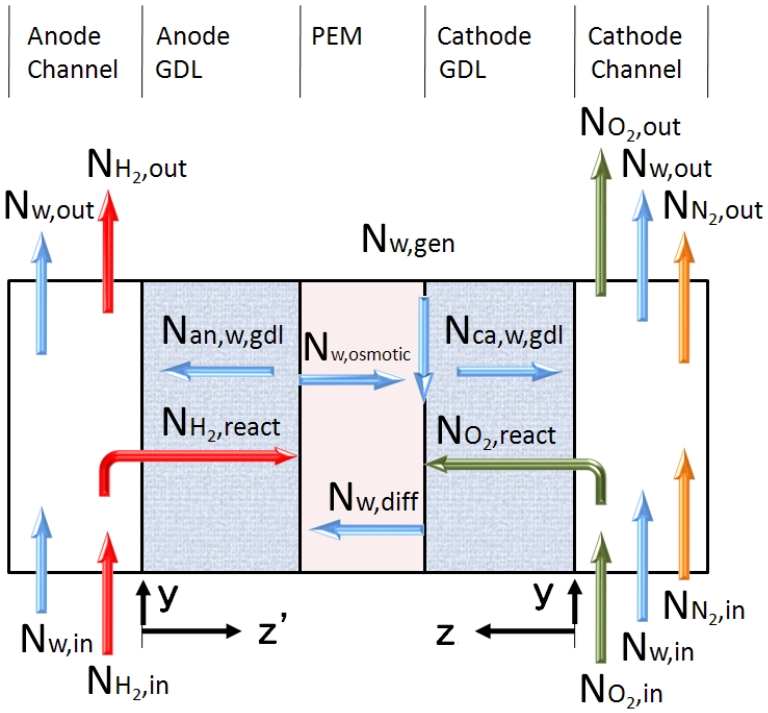

Figure 2-2: Species flow in a segment

2.2 Anode/Cathode Channel Model

The channel model describes the reactant flow behavior inside the anode and cathode of a segment. The model uses the molar conservation principle and fluid dynamic properties to calculate the outflow properties and pressure drop along the flow channels. The pressure drop of the gas mixture in the fuel cell flow channels was rarely considered in earlier models; however, in practical it is one of the key parameters in designing a fuel cell because it is related to the selection of the air pump and the efficiency of a fuel cell system.

The segment current, I_{seg}, is an input based on which the segment model can be simulated. The amount of consumed reactants in the segment can be determined by the fundamental equations:

$$N_{H_2,react} = \frac{I_{seg}}{2F} \tag{2.9}$$

$$N_{O_2,react} = \frac{I_{seg}}{4F} \tag{2.10}$$

The amount of water generation at the cathode catalyst layer can be expressed as

$$N_{\mathrm{w,gen}} = \frac{I_{\mathrm{seg}}}{2\mathrm{F}} \tag{2.11}$$

Then the molar outflow rates can be calculated from

$$N_{\mathrm{H_2,out}} = N_{\mathrm{H_2,in}} - N_{\mathrm{H_2,react}} \tag{2.12}$$

$$N_{\mathrm{O_2,out}} = N_{\mathrm{O_2,in}} - N_{\mathrm{O_2,react}} \tag{2.13}$$

$$N_{\mathrm{an,w,out}} = N_{\mathrm{an,w,in}} - N_{\mathrm{an,w,gdl}} \tag{2.14}$$

$$N_{\mathrm{ca,w,out}} = N_{\mathrm{ca,w,in}} - N_{\mathrm{ca,w,gdl}} \tag{2.15}$$

The water molar flow rates $N_{\mathrm{an,w,gdl}}$ and $N_{\mathrm{ca,w,gdl}}$ through GDL in Equations (2.14) and (2.15) are calculated by the gas diffusion layer model, which will be discussed in the next section.

The pressure drop due to friction for a continuous, straight channel with length L can be calculated from the following equation [53]:

$$\Delta P = 32\int_0^L \frac{\mu(y)Q(y)}{A_{ch}d_{ch}^2}dy \tag{2.16}$$

Since the reactant is consumed along the flow channel direction y, as a first-order approximation, we assume that dynamic viscosity $\mu(y)$ and flow rate $Q(y)$ vary linearly along the flow channel:

$$\mu(y) = \mu_{\mathrm{in}} - \frac{y}{L}\left(\mu_{\mathrm{in}} - \mu_{\mathrm{out}}\right) \tag{2.17}$$

$$Q(y) = Q_{\mathrm{in}} - \frac{y}{L}\left(Q_{\mathrm{in}} - Q_{\mathrm{out}}\right) \tag{2.18}$$

where μ_{in} and μ_{out} are the dynamic viscosities of the mixture at the inlet and outlet, respectively, and can be calculated by the mixture properties

$$\mu = \sum_i x_i\mu_i \tag{2.19}$$

where x_{i} is the molar fraction of species i. Similarly, the mixture flow rates at inlet Q_{in} and outlet Q_{out} can be expressed in terms of the ideal gas law:

$$Q = \frac{RT}{P}\sum_i N_i \tag{2.20}$$

After substituting Equation (2.17) and Equation (2.18) into Equation (2.16), and integrating the equation, the pressure drop along the channel can be expressed as:

$$P_{\text{in}} - P_{\text{out}} = \frac{16L}{3A_{\text{ch}}d_{\text{ch}}^2}\left[Q_{\text{in}}\left(2\mu_{\text{in}} + \mu_{\text{out}}\right) + Q_{\text{out}}\left(\mu_{\text{in}} + 2\mu_{\text{out}}\right)\right] \tag{2.21}$$

The outflow pressure can be determined by Equation (2.21), and the average pressure in a segment can be calculated by

$$P_{\text{avg}} = \frac{1}{2}\left(P_{\text{in}} + P_{\text{out}}\right) \tag{2.22}$$

From the discussion above, the molar flow rates of every species and pressure at the segment outlet are determined. These properties are used as inflow properties for the next segment.

2.3 Anode/Cathode Gas Diffusion Layer Model

Because GDLs are porous media, and more than one species move through GDLs, we need to consider the effect of porous media on the diffusion of gas mixtures. Each species has different diffusivity, so the molar fraction of the species will vary along the diffusion path. The purpose of the GDL model is to calculate the molar fraction at the GDL/membrane interface. Furthermore, by knowing the average pressure, we can determine the partial pressure of hydrogen (using the anode GDL model), oxygen (cathode GDL model) as well as water activity for both. The hydrogen and oxygen partial pressures are used in the segment voltage model. Water activity is used in membrane hydration model to determine the water transport through membrane.

Water transport from membrane to channel via the GDL could be in two forms, gas and liquid; therefore, we need to consider the under-saturated and saturated conditions separately. At under-saturated conditions, water vapor transport direction depends on the relative humidity in the channel and at the membrane/GDL interface. At saturated condition, water generated in the catalyst layer will transport through the GDL in the liquid form. The presence of liquid water in the GDL not only induces more resistance to gas diffusion but also covers part of the activation sites on the catalyst layer.

The Stefan-Maxwell equation is used to describe multi-component gas mixtures diffusion through the GDL [54]. For n-component gas diffusion through a porous medium, the molar fraction gradient of species *i*, is in the form:

$$\nabla x_i = RT\sum_j^n \frac{x_i N_j - x_j N_i}{PD_{i-j}^{\text{eff}}} \tag{2.23}$$

where N_i and N_j are molar flux of species *i* and *j*. PD_{i-j}^{eff} is the effective pressure diffusivity product of the mixture *i-j* in the porous medium, and it is related to that in a nonporous system PD_{i-j} by [55]

$$PD_{i-j}^{\text{eff}} = PD_{i-j}\varepsilon^{1.5} \tag{2.24}$$

where ε is the porosity of the GDL. The pressure diffusivity PD_{i-j} is dependent only on temperature *T*, and can be estimated from critical temperature T_c, critical pressure P_c and molecular weight *M* of components *i* and *j* with the following equation [54].

$$PD_{i-j} = a\left(\frac{T}{\sqrt{T_{ci}T_{cj}}}\right)^b \left(P_{ci}P_{cj}\right)^{1/3}\left(T_{ci}T_{cj}\right)^{5/12}\left(\frac{1}{M_i}+\frac{1}{M_j}\right)^{1/2} \tag{2.25}$$

N_i and N_j in Equation (2.23) can be the molar flux of hydrogen, oxygen, or water vapor through the GDL, and can be calculated from the segment current or the membrane hydration model.

2.3.1 Under-Saturated Condition

In the anode GDL, which contains hydrogen and water vapor, the water vapor molar fraction gradient is also expressed by the Stefan-Maxwell equation

$$\frac{dx_{\text{v,gdl}}}{dz'} = \frac{RT_{\text{seg}}}{P_{\text{an,avg}}D_{\text{H}_2\text{-v}}}\left(x_{\text{v,gdl}}N_{\text{H}_2\text{,gdl}} - x_{\text{H}_2\text{,gdl}}N_{\text{v,gdl}}\right) \tag{2.26}$$

The direction z' is defined in Figure 2-2.

Since the sum of the molar fractions of all species is equal to 1, for anode we have

$$x_{\text{v,gdl}} + x_{\text{H}_2\text{,gdl}} = 1 \tag{2.27}$$

In Equation (2.26), $N_{\text{v,gdl}}$ is the molar water transport determined by the membrane hydration model, and hydrogen molar flux through the GDL is equal to the reacted hydrogen rate and is calculated bye Equation (2.9).

Equation (2.26) can be simplified by defining

$$\mathrm{B}_1 \equiv -\frac{RT_{\text{seg}}}{P_{\text{an,avg}} D_{\text{v-H}_2}} \left(N_{\text{H}_2,\text{gdl}} + N_{\text{v,gdl}} \right), \tag{2.28}$$

$$\mathrm{B}_2 \equiv \frac{RT_{\text{seg}}}{P_{\text{an,avg}} D_{\text{v-H}_2}} N_{\text{v,gdl}} \tag{2.29}$$

Given the boundary condition $x = x_{\text{v,c/g}}$ at $z' = 0$, the water vapor molar fraction profile in the GDL can be solved:

$$x_{\text{v,gdl}}(z') = \frac{\mathrm{B}_2}{\mathrm{B}_1} + \exp(-\mathrm{B}_1 z') \left(x_{\text{v,c/g}} - \frac{\mathrm{B}_2}{\mathrm{B}_1} \right) \tag{2.30}$$

The above equation describes the water vapor molar fraction distribution across the anode GDL due to water vapor flux and hydrogen flux. At the GDL/membrane interface, $z' = t_{\text{gdl}}$, the value of the water vapor molar fraction is

$$x_{\text{v,g/m}} = \frac{\mathrm{B}_2}{\mathrm{B}_1} + \exp(-\mathrm{B}_1 t_{\text{gdl}}) \left(x_{\text{v,c/g}} - \frac{\mathrm{B}_2}{\mathrm{B}_1} \right) \tag{2.31}$$

After knowing the water vapor molar fraction at the GDL/membrane interface, we can calculate the water activity at the same interface:

$$a_{\text{an,v,g/m}} = \frac{x_{\text{v,g/m}} P_{\text{an,avg}}}{P_{\text{v,sat}}} \tag{2.32}$$

The hydrogen partial pressure at the GDL/membrane interface is an important parameter to calculate segment voltage and it is determined from

$$P_{\text{an,H}_2,\text{g/m}} = P_{\text{an,avg}} \left(1 - x_{\text{v,g/m}} \right) \tag{2.33}$$

If the relative humidity of gas flow in the channel is different from that at the GDL/channel interface, there will be water vapor flux in between. The molar flux of water vapor at the GDL/channel interface depends on the inflow relative humidity and is obtained from

$$N_{\text{v,conv}} = K_{\text{conv}} \left(x_{\text{c/g}} - x_{\text{in}} \right) A_{\text{seg,conv}} \tag{2.34}$$

where the convective mass transfer coefficient K_{conv} is defined by the Sherwood number.

$$K_{\text{conv}} = Sh \cdot c \cdot D_{ij} \cdot d_{\text{ch}} \tag{2.35}$$

In the above equation, D_{ij} is the diffusivity of species i in the flow gas j. For the laminar flow and constant surface temperature conditions in a fuel cell, the Sherwood number Sh is constant and is equal to 3.21 [56].

In the cathode, three species are flowing in the channel and their molar fraction gradients across the GDL are calculated from the Stefan-Maxwell equation:

$$\frac{dx_{\mathrm{O_2,gdl}}}{dz}=\frac{RT_{\mathrm{seg}}}{P_{\mathrm{ca,avg}}}\left(\frac{x_{\mathrm{O_2,gdl}}N_{\mathrm{v,gdl}}-x_{\mathrm{v,gdl}}N_{\mathrm{O_2,gdl}}}{D_{\mathrm{O_2\text{-}v}}}+\frac{x_{\mathrm{O_2,gdl}}N_{\mathrm{N_2,gdl}}-x_{\mathrm{N_2,gdl}}N_{\mathrm{O_2,gdl}}}{D_{\mathrm{O_2\text{-}N_2}}}\right) \tag{2.36}$$

$$\frac{dx_{\mathrm{v,gdl}}}{dz}=\frac{RT_{\mathrm{seg}}}{P_{\mathrm{ca,avg}}}\left(\frac{x_{\mathrm{v,gdl}}N_{\mathrm{O_2,gdl}}-x_{\mathrm{O_2,gdl}}N_{\mathrm{v,gdl}}}{D_{\mathrm{O_2\text{-}v}}}+\frac{x_{\mathrm{v,gdl}}N_{\mathrm{N_2,gdl}}-x_{\mathrm{N_2,gdl}}N_{\mathrm{v,gdl}}}{D_{\mathrm{v\text{-}N_2}}}\right) \tag{2.37}$$

$$\frac{dx_{\mathrm{N_2,gdl}}}{dz}=\frac{RT_{\mathrm{seg}}}{P_{\mathrm{ca,avg}}}\left(\frac{x_{\mathrm{N_2,gdl}}N_{\mathrm{v,gdl}}-x_{\mathrm{v,gdl}}N_{\mathrm{N_2,gdl}}}{D_{\mathrm{v\text{-}N_2}}}+\frac{x_{\mathrm{N_2,gdl}}N_{\mathrm{O_2,gdl}}-x_{\mathrm{O_2,gdl}}N_{\mathrm{N_2,gdl}}}{D_{\mathrm{O_2\text{-}N_2}}}\right) \tag{2.38}$$

where the direction z is defined in Figure 2-2.

Since Nitrogen does not react, there is no Nitrogen molar flux through the GDL, i.e., $N_{\mathrm{N_2,gdl}}=0$. Define

$$\mathrm{B}_3=\frac{RT_{\mathrm{seg}}}{P_{\mathrm{ca,avg}}}\frac{N_{\mathrm{v,gdl}}}{D_{\mathrm{O_2\text{-}v}}},\ \mathrm{B}_4=\frac{RT_{\mathrm{seg}}}{P_{\mathrm{ca,avg}}}\frac{N_{\mathrm{O_2,gdl}}}{D_{\mathrm{O_2\text{-}v}}},\ \mathrm{B}_5=\frac{RT_{\mathrm{seg}}}{P_{\mathrm{ca,avg}}}\frac{N_{\mathrm{O_2,gdl}}}{D_{\mathrm{O_2\text{-}N_2}}},\ \mathrm{B}_6=\frac{RT_{\mathrm{seg}}}{P_{\mathrm{ca,avg}}}\frac{N_{\mathrm{v,gdl}}}{D_{\mathrm{v\text{-}N_2}}} \tag{2.39}$$

Equations (2.36) to (2.38) then can be expressed in the matrix form

$$\frac{d}{dz}\begin{bmatrix}x_{\mathrm{O_2,gdl}}\\x_{\mathrm{v,gdl}}\\x_{\mathrm{N_2,gdl}}\end{bmatrix}=\begin{bmatrix}\mathrm{B}_3 & -\mathrm{B}_4 & -\mathrm{B}_5\\-\mathrm{B}_3 & \mathrm{B}_4 & -\mathrm{B}_6\\0 & 0 & (\mathrm{B}_5+\mathrm{B}_6)\end{bmatrix}\begin{bmatrix}x_{\mathrm{O_2,gdl}}\\x_{\mathrm{v,gdl}}\\x_{\mathrm{N_2,gdl}}\end{bmatrix} \tag{2.40}$$

or

$$\frac{d\mathbf{x}}{dz}=\mathbf{B}\cdot\mathbf{x} \tag{2.41}$$

The solution of Equation (2.41) can be solved by finding the state transition matrix

$$\mathbf{\Phi}(z)=\exp\left(\mathbf{B}\cdot z\right) \tag{2.42}$$

and the boundary condition at $z=0$:

$$\mathbf{x}(0)=\begin{bmatrix}x_{\mathrm{O_2,c/g}}\\x_{\mathrm{v,c/g}}\\x_{\mathrm{N_2,c/g}}\end{bmatrix} \tag{2.43}$$

The molar fraction at the GDL/membrane interface is

$$\mathbf{x}(t_{\text{gdl}}) = \mathbf{\Phi}(t_{\text{gdl}}) \cdot \mathbf{x}(0) \tag{2.44}$$

Once the molar fractions of reactants at the GDL/membrane interface are determined, the partial pressures of reactants can be calculated and used in the segment voltage model to determine the segment voltage.

2.3.2 Saturated Condition

When water vapor pressure reaches the saturation pressure, condensation occurs. Under this condition, all additional water generated in the cathode catalyst layer appears in the liquid form. Because the GDL is commonly Teflonized to provide a hydrophobic surface for easy removal of liquid water, the liquid water moves through the porous GDL to the surface of GDL, forming liquid droplets, and is removed by gas flow. The liquid water generation and electro-osmotic drag flux increase with current density, so at high current density, the cathode side could have a flooding problem. Pasaogullari and Wang [13] described liquid water transport in the GDL by using a capillary pressure model. Since flooding could occur on the cathode side, in the GDL model presented here, we must consider the effect of liquid water on diffusivity and cell performance; we will also include capillary pressure to model the saturated condition in the cathode GDL.

For saturated conditions in the anode, we assume the vapor pressures in the channel and in the GDL are both equal to the saturated water vapor pressure. The vapor pressure is proportional to the molar fraction, so the water vapor molar fraction in the GDL is equal to the saturated vapor molar fraction and is constant:

$$x_{\text{v,gdl}}(z') = x_{\text{v,sat}} = \frac{P_{\text{v,sat}}}{P_{\text{an,avg}}} \tag{2.45}$$

Since the molar fraction of water vapor is constant, its gradient is zero, and the hydrogen molar fraction is determined from

$$x_{\text{H}_2,\text{gdl}}(z') = 1 - x_{\text{v,sat}} \tag{2.46}$$

Hence the hydrogen partial pressure is

$$P_{\text{H}_2,\text{g/m}} = x_{\text{H}_2,\text{gdl}}(z') \cdot P_{\text{an,avg}} \tag{2.47}$$

Similarly, when the cathode is saturated, water vapor molar fraction is equal to the saturated molar fraction and is constant, therefore:

$$\frac{dx_{\mathrm{v,gdl}}}{dz} = 0 \tag{2.48}$$

Since the sum of the molar fraction of all species is equal to one:

$$x_{\mathrm{O_2,gdl}} + x_{\mathrm{v,gdl}} + x_{\mathrm{N_2,gdl}} = 1 \tag{2.49}$$

Given that $x_{\mathrm{v,gdl}}$ is constant, if we know nitrogen molar fraction, the Oxygen molar fraction can be determined. Then we use Equation (2.38) to calculate the Nitrogen molar fraction from the linear equation

$$\frac{dx_{\mathrm{N_2,gdl}}}{dz} = \mathrm{B}_5 x_{\mathrm{N_2,gdl}} \tag{2.50}$$

Given the boundary condition, $x_{\mathrm{N_2,gdl}} = x_{\mathrm{N_2,c/g}}$ at $z = 0$, the nitrogen molar fraction in the cathode GDL can be expressed as

$$x_{\mathrm{N_2,gdl}}(z) = x_{\mathrm{N_2,c/g}} \exp\left(\mathrm{B}_5 z\right) \tag{2.51}$$

At $z = t_{\mathrm{gdl}}$, the molar fraction of Nitrogen at the GDL/membrane interface is calculated as

$$x_{\mathrm{N_2,g/m}} = x_{\mathrm{N_2,c/g}} \exp\left(\mathrm{B}_5 t_{\mathrm{gdl}}\right) \tag{2.52}$$

The partial pressure of oxygen at the same interface is then determined from

$$P_{\mathrm{ca,O_2,g/m}} = P_{\mathrm{ca,avg}}\left(1 - x_{\mathrm{v,sat}} - x_{\mathrm{N_2,g/m}}\right) \tag{2.53}$$

On the cathode side, the presence of liquid water will influence the effective diffusivity of a porous GDL. The effective diffusivity D_i^{eff} is correlated with porosity ε and saturation s by

$$D_i^{eff} = D_i f(\varepsilon) g(s) \tag{2.54}$$

The saturation s in Equation (2.54) is defined as the ratio of liquid water volume and pore volume:

$$s = \frac{V_w}{V_p} \tag{2.55}$$

Earlier studies [7, 12, 17, 57-60] suggest the influence of porosity on diffusivity to be approximated by a polynomial relationship:

$$f(\varepsilon) = \varepsilon^{1.5} \tag{2.56}$$

The presence of liquid water reduces the diffusion area in the GDL and its effect is commonly modeled by a normalized function as

$$g(s) = (1-s)^m \tag{2.57}$$

Mezedur et al. [61] suggests $m = 0.71$ for their porous medium, whereas Nam et al. [62] suggested $m = 2$, which is used in this study.

Inside the GDL, liquid water is driven by capillary pressure, which is defined as the difference between liquid and gas-phase pressures.

$$P_c = P_g - P_w \tag{2.58}$$

In hydrophobic GDLs, the capillary pressure is negative and drives the liquid water from the reaction sites to the surface of the GDL. The capillary pressure between the two phases is expressed as

$$P_c = \sigma \cos\theta_c \left(\frac{\varepsilon}{K}\right)^{1/2} J(S) \tag{2.59}$$

where $J(S)$ is a function of liquid saturation explained below in Equation (2.61). σ is the surface tension and is taken as 0.0625 N m^{-1} for liquid water-air systems, θ_c is the contact angle, and K is the permeability of the GDL. Both θ_c and K are GDL dependant.

In Pasaogullari's [13] and Nam's [62] studies, they used Leverett's function for $J(S)$:

$$J(S) = 1.417S - 2.120S^2 + 1.263S^3 \tag{2.60}$$

where S is the reduced water saturation and is defined as

$$S = \frac{s - s_{im}}{1 - s_{im}} \tag{2.61}$$

In the above equation, s_{im} is the immobile saturation of GDL and is chosen as 0.1 in Nam's study [62]. In addition, when s is less than s_{im}, S is equal to zero.

The liquid flow through GDL under the channel induced by capillary pressure [13, 62] is expressed as:

$$N_{ca,w,gdl} = -\frac{\rho_w K K_{rw}}{M_w \mu_w}\left(\frac{dP_c}{dS}\right)\frac{dS}{dz} \tag{2.62}$$

The definition of parameters on the right hand side of Equation (2.62) and their values are listed in Table 2.1. At steady state, $N_{ca,w,gdl}$ is equal to the net water flux from anode to

cathode and is determined by the membrane hydration model. Then reduced saturation S can be obtained by solving Equation (2.62).

Table 2.1: Parameters used for GDL

Parameter	Value
Liquid water density (ρ_w)	1000 kg m^{-3}
Absolute permeability (K)	1×10^{-8} m^2 13
Relative permeability (K_{rw})	S 14
Molecular weight of liquid water (M_w)	18×10^{-3} kg mol^{-1}
Dynamic viscosity of water vapor (μ_w)	4×10^{-4} N s m^{-2}

Instead of using Leverett's function (Equation (2.60)) to calculate the capillary pressure, Natarajan [14] suggested another empirical pressure gradient and did not consider the effect of immobile saturation:

$$\frac{dP_c}{ds} = -3.7\times0.0173\left\{\exp\left[-3.7\left(s-0.494\right)\right]+\exp\left[3.7\left(s-0.494\right)\right]\right\} \tag{2.63}$$

Then Equation (2.62) becomes

$$N_{ca,w,gdl} = -\frac{\rho_w K K_{rw}}{M_w \mu_w}\left(\frac{dP_c}{ds}\right)\frac{ds}{dz} \tag{2.64}$$

Theses two-phase flow models in Pasaogullari's, Nam's and Natarajan's studies describe the liquid saturation in the GDL under channel, as shown in Figure 2-3. The difference between these two results is distinct; Pasaogullari's model is a 2-D model and only describes the distribution of liquid saturation in the GDL under the channel. Their results show average liquid saturation in the GDL under the channel is close to 0.07. Natarajan's model shows 3-dimensional liquid saturation distribution in the GDLs both under the channels and under the ribs. The liquid saturation in the GDL under the ribs is higher than 0.9, whereas that in the GDL under the channel varies between 0 and 0.88. The huge difference arouses our desire to understand the water accumulation in the GDLs under the channels and under the ribs.

In addition, according to Zhang's [18] and Turhan's [17] studies, it is the GDL under rib where water content increases with current density. In addition, ribs account for almost half of the active area, so they cannot be neglected. Therefore, in this study, we

will propose a model that describes the liquid saturation in the GDL under ribs based on neutron experimental results.

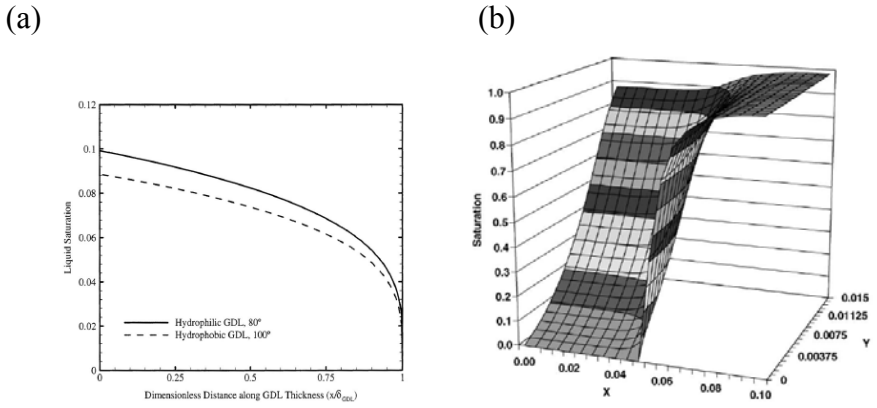

Figure 2-3. Liquid saturation in the GDL. (a) Pasaogullari's study [13] models the liquid saturation in the GDL under the channel. (b) Natarajan's study [14] model the liquid saturation in the GDL under the channel and under the rib.

Figure 2-4 shows the mechanism of water transport through the GDL. In Figure 2-4 (a), water emerges in the cathode catalyst layer due to net water transport from anode to cathode and due to water generation. Because the air flow diffuses through the GDL, most liquid water transport is constrained in the GDL under ribs, as shown in Figure 2-4 (b). The liquid water flux is induced by capillary pressure and transports through the pores of GDL, accumulating adjacent to the ribs, as shown in Figure 2-4 (c). When the GDL under ribs cannot hold more liquid water, the liquid water emerges from the corner of ribs and GDL to the channels. The liquid water then is carried away by air flow, as shown in Figure 2-4(d).

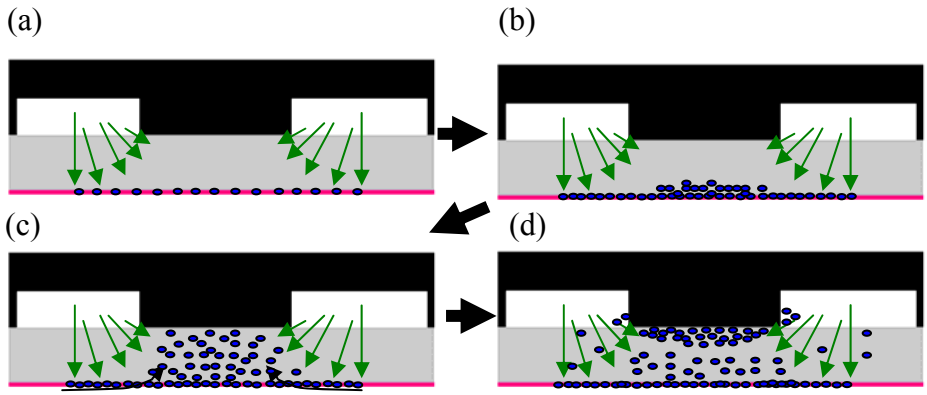

Figure 2-4: Liquid water transport and distribution in the GDL under ribs

In this model, we need to determine the amount of liquid water transport through the GDL under the channel and through the GDL under the rib. In Chapter 3, the water thickness in the cathode GDL under the channel is assumed to be inversely proportional to the gas flow rate. Similarly, we assume the water transport through the GDL under the channel is also inversely proportional to the gas flaw rate in the channel:

$$N_{\text{ca,w,gdl,ch}} = \frac{\beta}{N_{\text{ca, react, ch}}} \tag{2.65}$$

Once we determine the water transport in the GDL under the channel, we can calculate the distribution of liquid saturation in the GDL by using Equation (2.62). To simplify the problem, dP_c / dS in Equation (2.62) is chosen as 22.95 N cm^{-2} [59]. Then the liquid saturation in the catalyst layer can be obtained.

Once the water transport in the GDL $N_{\text{ca,w,gdl,ch}}$ is known, we can calculate the amount of water transport in the GDL under the rib by

$$N_{\text{ca,w,gdl,rib}} = N_{\text{ca,w,gdl}} - N_{\text{ca,w,gdl,ch}} \tag{2.66}$$

According to experimental results in Chapter 3, the maximum water thickness in the cathode GDL under the rib is approximately 50 μm. The result implies even though liquid water flux is very large, the cathode GDL under the rib has a limited capacity to hold liquid water. Thus, the average water thickness of in the GDL under the rib in a segment is approximated by

$$t_{\text{ca,gdl,rib}} = t_{\text{w,max}} \left(1 - \exp\left(\frac{\alpha N_{\text{ca,w,gdl,rib}}}{\left(N_{\text{ca,gas,ch}} \right)^{\gamma}} \right) \right) \tag{2.67}$$

where $t_{ca,gdl,rib}$ is the average water thickness in the GDLs, $N_{\text{ca,w,gdl,rib}}$ is the net water flux in the cathode GDL from catalyst layer toward channels. Then the average liquid saturation in the GDL under the rib can be calculated from

$$s_{ca,gdl,rib} = \frac{t_{ca,gdl,rib} \cdot A}{t_{gdl} \cdot A \cdot \varepsilon} = \frac{t_{ca,gdl,rib}}{t_{gdl} \cdot \varepsilon} \tag{2.68}$$

where t_{gdl} is the GDL thickness, A is the segment area, and ε is the porosity of GDL.

We calculate liquid saturation in the GDL under the channel and liquid saturation in the GDL under the rib separately. Then the average value between these two variables will be used in the segment voltage model.

2.4 Membrane Hydration Model

The water transport within membranes is represented by the membrane hydration model shown in Figure 2-2. The membrane hydration model determines the water transport through the anode/cathode GDLs and water content for determining the membrane conductivity. As shown in Figure 2-2, there are three mechanisms for water flux in the membrane. They are electro-osmotic drag from anode to cathode, back diffusion due to the concentration potential difference between anode and cathode, and water generation at the cathode catalyst layer. These three factors are explained in the following.

The electro-osmotic drag is defined as

$$N_{\text{w,osmotic}} = K_{\text{osmotic}} \frac{I_{\text{seg}}}{\text{F}} \tag{2.69}$$

where K_{osmotic} is the osmotic drag coefficient, and has been studied by many researchers [5, 6, 63-66]. Some results have shown that the value is constant, and others have shown that it depends on the water content in the membrane. In this study, we use Springer's results [5]:

$$K_{\text{osmotic}} = \frac{2.5\lambda_{pem}}{22} \tag{2.70}$$

The water content in the membrane λ_{pem}, is determined from water activity of membrane a_{pem}:

$$\lambda_{pem} = 0.043 + 17.81a_{pem} - 39.85a_{pem}^2 + 36.0a_{pem}^3,\ 0 < a_{pem} \le 1 \tag{2.71}$$

The average water activity of anode and cathode is used to calculate the water content in the membrane:

$$a_{\text{pem}} = \frac{a_{\text{an}} + a_{\text{ca}}}{2} \tag{2.72}$$

In Equation (2.72), a_{an} and a_{ca} are equal to the relative humidity of anode and cathode.

The water transport by back diffusion is expressed as

$$N_{\text{w,diff}} = K_{\text{diff}} \frac{c_{\text{w,ca}} - c_{\text{w,an}}}{t_{\text{pem}}} \tag{2.73}$$

where c_{w} is the water concentration of the membrane as defined by Fuller [6], and t_{pem} is the membrane thickness. Water concentration is calculated as

$$c_{\text{w,an}} = \frac{\rho_{\text{pem}}}{M_{\text{pem}}} \lambda_{\text{an}} \tag{2.74}$$

$$c_{\text{w,ca}} = \frac{\rho_{\text{pem}}}{M_{\text{pem}}} \lambda_{\text{ca}} \tag{2.75}$$

λ_{an} and λ_{ca} in the above equations can be calculated by water activity in anode and cathode:

$$\lambda_{an} = 0.043 + 17.81 a_{an} - 39.85 a_{an}^2 + 36.0 a_{an}^3, \ 0 < a_{an} \le 1 \tag{2.76}$$

$$\lambda_{ca} = 0.043 + 17.81 a_{ca} - 39.85 a_{ca}^2 + 36.0 a_{ca}^3, \ 0 < a_{ca} \le 1 \tag{2.77}$$

In Equation (2.73), K_{diff} is the back diffusion coefficient and is a function of temperature and water content in the membrane 5, [67]:

$$K_{\text{diff}} = K_{\lambda} \exp\left(2416 \left(\frac{1}{303} - \frac{1}{T_{\text{seg}}} \right) \right) \tag{2.78}$$

where

$$K_{\lambda} = \begin{cases} 10^{-10} & , \lambda_{\text{pem}} < 2 \\ 10^{-10} \left(1 + 2 \left(\lambda_{\text{pem}} - 2 \right) \right) & , 2 \le \lambda_{\text{pem}} \le 3 \\ 10^{-10} \left(3 - 1.167 \left(\lambda_{\text{pem}} - 3 \right) \right) & , 3 < \lambda_{\text{pem}} \le 4.5 \\ 1.25 \times 10^{-10} & , \lambda_{\text{pem}} \ge 4.5 \end{cases} \tag{2.79}$$

The net water flux through the anode GDL is

$$N_{\text{an,w,gdl}} = N_{\text{w,diff}} - N_{\text{w,osmotic}} \tag{2.80}$$

whereas that through the cathode GDL is

$$N_{\text{ca,w,gdl}} = N_{\text{w,osmotic}} - N_{\text{w,diff}} + \frac{I_{\text{seg}}}{2\text{F}} \tag{2.81}$$

where the last term on the right hand side is the water generation at the cathode catalyst layer.

The water content is used to calculate the membrane conductivity in the segment voltage model, and the water fluxes in anode and cathode are used in the GDL model and the flow channel model.

2.5 Segment Voltage Model

The segment voltage model calculates voltage of each segment at specific current according to the partial pressures of hydrogen and oxygen, membrane water content, and temperature. The segment voltage can be expressed as

$$V_{\text{seg}} = V_{\text{rev}} - V_{\text{act}} - V_{\text{ohm}} - V_{\text{conc}} \tag{2.82}$$

where V_{rev}, V_{act}, V_{ohm}, V_{conc} are the theoretical reversible voltage, the activation overpotential, the ohmic overpotential, and the concentration overpotential, respectively.

The theoretical reversible voltage is calculated from [68]:

$$\begin{aligned} V_{\text{rev}} &= \frac{-\Delta G}{2\text{F}} \\ &= \frac{-\Delta G^0}{2\text{F}} + \frac{\text{R}T_{\text{seg}}}{2\text{F}} \ln\left(\frac{P_{\text{H}_2} P_{\text{O}_2}^{0.5}}{P_{\text{H}_2\text{O}}}\right) \\ &= 1.229 - 0.85\times10^{-3}\left(T_{\text{seg}} - 298.15\right) + 4.3085\times10^{-5} T_{\text{seg}}\left[\ln\left(P_{\text{an,H}_2,\text{g/m}}\right) + \frac{1}{2}\ln(P_{\text{ca,O}_2,\text{g/m}})\right] \end{aligned} \tag{2.83}$$

The partial pressures of hydrogen $P_{\text{an,H}_2,\text{g/m}}$ and oxygen $P_{\text{ca,O}_2,\text{g/m}}$ come from the anode/cathode GDL models.

The activation overpotential arises from the kinetic reaction at the anode and cathode [69-71]. Due to the slower kinetics of oxygen reduction at the cathode side, the voltage drop due to activation overpotential is dominated by the cathode. The overpotential is modified from Pukrushpan's study [24] as

$$V_{\text{act}} = 0.275 + 0.1\left[1 - \exp(-12 i_{\text{seg}})\right] \tag{2.84}$$

where i_{seg} is the current density of a segment.

The ohmic overpotential is due to the internal resistance of a segment and is expressed as

$$V_{\text{ohm}} = I_{\text{seg}} R_{\text{seg}} \tag{2.85}$$

where I_{seg} is the segment current. The resistance of the segment is the sum of all components through which current flows and contact resistance. These components are membrane, GDLs, and flow field plates:

$$R_{\text{seg}} = R_{\text{pem}} + R_{\text{gdl}} + R_{\text{plate}} + R_{\text{contact}} \tag{2.86}$$

The conductivities of GDL and graphite plates are typically much larger than that of the membrane, so it is not necessary to consider their resistances. Thus only the membrane resistance is considered in this model, which is obtained from

$$R_{\text{pem}} = \frac{t_{\text{pem}}}{\sigma_{\text{pem}}} \tag{2.87}$$

where the membrane conductivity σ_{pem} is a function of temperature and water content in the membrane, and is expressed in the form [5],

$$\sigma_{\text{pem}} = \left(b_{11}\lambda_{\text{pem}} - b_{12}\right)\exp\left[b_{13}\left(\frac{1}{303} - \frac{1}{T_{\text{seg}}}\right)\right] \tag{2.88}$$

where b_{11}, b_{12}, and b_{13} are empirically determined from our experimental results.

Concentration overpotential results from the change in concentration of the reactants as they are consumed in the reaction. The concentration overpotential is significant at high current density and it is frequently expressed by the Nernst equation:

$$V_{conc} = -\frac{RT}{\alpha_c F}\ln\left(1 - \frac{i_{seg}}{i_0}\right) \tag{2.89}$$

However, at high current density, the concentration overpotential from Equation (2.89) is not significant. Squadrito et al. [60] suggest another empirical form:

$$V_{conc} = b{i_{seg}}^{k}\ln\left(1 - \frac{i_{seg}}{i_0}\right) \tag{2.90}$$

where b and k are coefficients to determining the voltage drop. In addition, the flooding effect is also considered, which reduces the activation area of catalyst, so the maximum current density is reduced when liquid water appears at the catalyst layer. The modified concentration overpotential is expressed as

$$V_{\text{conc}} = b_{21}{i_{\text{seg}}}^{b_{22}}\ln\left(1 - \frac{i_{\text{seg}}}{i_{\text{limit}}(1-s)}\right) \tag{2.91}$$

where b_{21} and b_{22} are coefficients to be determined by experimental data.

In the above calculations, the current density in each segment is assumed to be known and the same. However, the cell voltage of all segments should be the same, and the difference in humidity, reactant pressure, etc. resulted in different current density. After each segment voltage model calculates its voltage, actual segment current can be corrected by enforcing all the segment voltages to be the same.

2.6 Cell Voltage Calculation

The models presented in previous sub-sections are implemented in the SIMULINK environment. The block diagrams of six sub-models of a segment are shown in Figure 2-5. Given the inflow properties and (initial guess of) segment current, the segment model calculates the segment voltage. Since the current density is actually not uniform throughout the active area, the cell voltage is determined iteratively by the process shown in Figure 2-6. Xi [72] developed a discretized SOFC model and provided an iterative algorithm to solve the equations in his model. We will use the similar algorithm to determine the cell voltage in our model. This algorithm will be explained briefly in the following.

At the beginning of an iteration, we guess an inlet gas pressure P_{in} and a current load I_{cell}. Under the desired stoichiometry values and relative humidity levels, the inflow anode and cathode flow properties for the cell can be determined. The initial guess for each segment current $I_{\text{seg, i}}$, is set to be one fifteenth of the cell current, I_{cell}. The segment voltage $V_{\text{seg, i}}$ is determined by the segment model described in previous sections. Because of the different locations, each segment may not have the same inflow gas properties such as reactant pressure, resulting in different segment voltages.

If the difference between the maximum and minimum segment voltages is not within an acceptable range, the segment currents need to be corrected. Based on the typical polarization curve of a fuel cell, the segment with higher voltage should increase its current, and that with lower voltage should decrease its current. To increase iteration speed, the change in segment current is set to be proportional to the voltage difference while keeping the cell current constant.

$$\Delta I_{\text{increased}} = k\left[\max(V_{\text{seg, i}}) - \min(V_{\text{seg, i}})\right] \tag{2.92}$$

$$I_{\text{seg, i}}\Big|^{n+1} = I_{\text{seg, i}}\Big|^{n} + \frac{\Delta I_{\text{increased}}}{\text{number of segments whose } V_{\text{seg, i}} > V_{\text{avg}}} \quad \text{when } V_{\text{seg, i}} > V_{\text{avg}} \tag{2.93}$$

$$I_{\text{seg, j}}\Big|^{n+1} = I_{\text{seg, j}}\Big|^{n} - \frac{\Delta I_{\text{increased}}}{\text{number of segments whose } V_{\text{seg, j}} < V_{\text{avg}}} \quad \text{when } V_{\text{seg, j}} < V_{\text{avg}} \tag{2.94}$$

The superscript n in these equations indicates the n-th step in time. In addition, the inlet pressures of the anode and cathode are also adjusted to keep the outlet pressure the same as the ambient pressure.

In this model, water accumulation in the GDL is an important factor to affect cell performance. To understand how liquid water accumulates in the GDL makes this model more accurate. The detail of observing and quantifying liquid water within a working fuel cell is illustrated in next chapter.

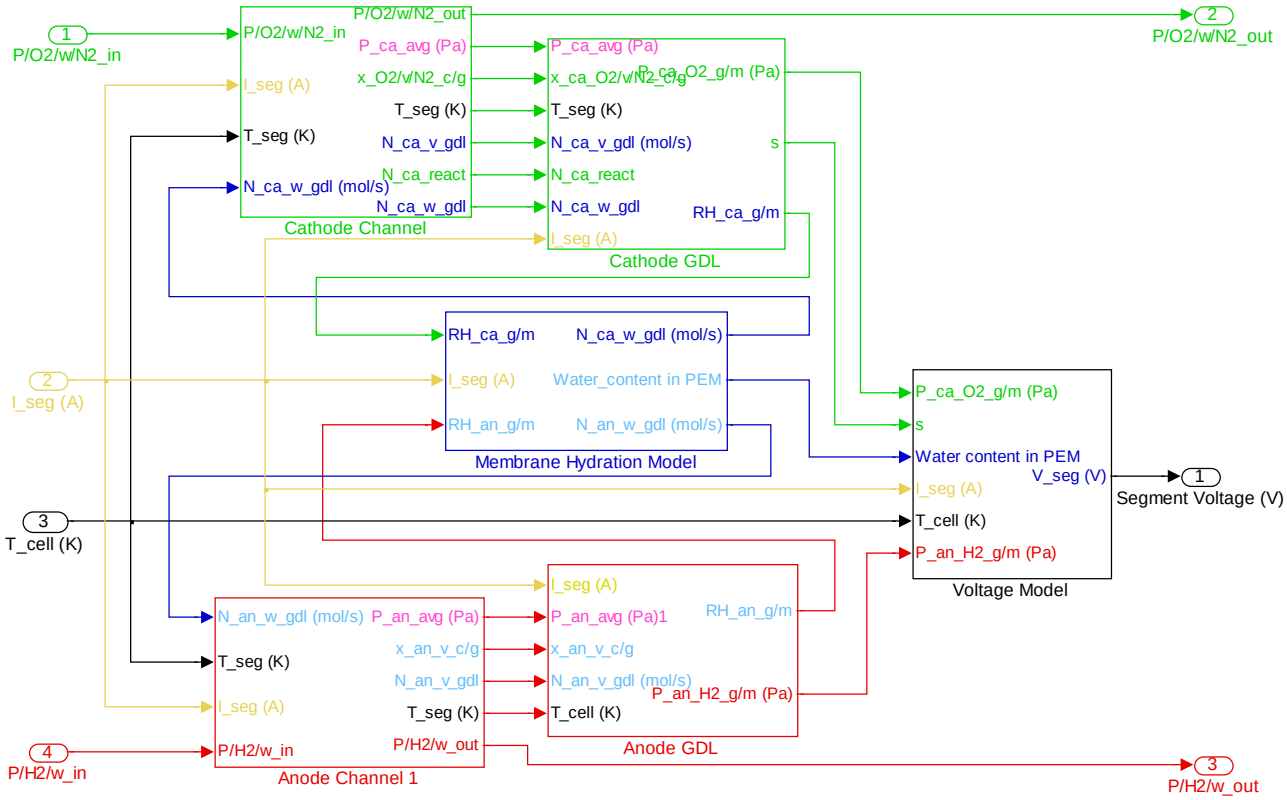

Figure 2-5: The connection of six sub-models in a segment

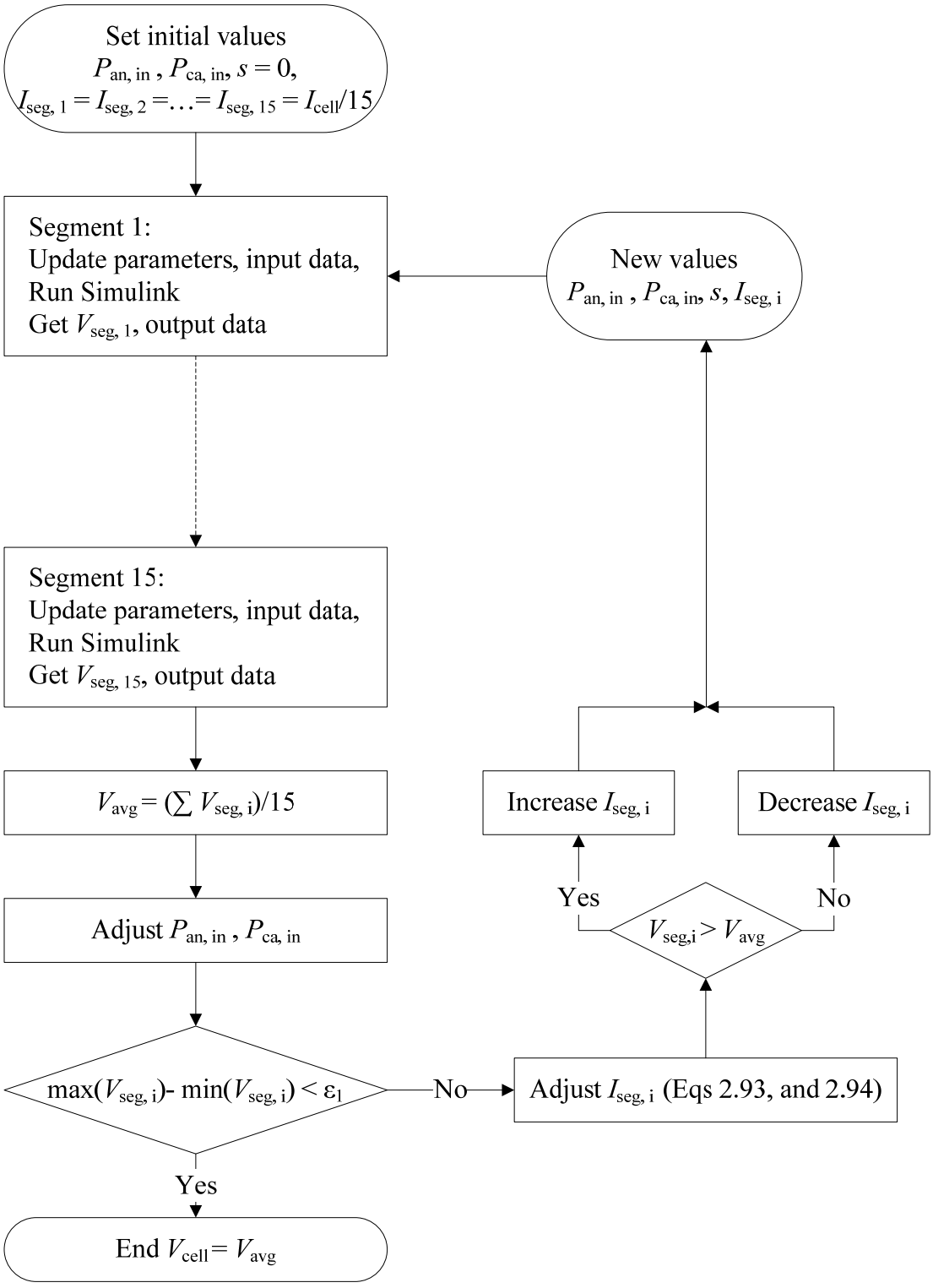

Figure 2-6: The process to solve cell voltage

CHAPTER 3
EXPERIMENTAL METHOD

As discussed in Chapter 2, the major water transport mechanisms in a PEMFC are electro-osmotic drag, back diffusion, and water transport in the GDL. Electro-osmotic drag and back diffusion have been studied experimentally. Water transport in the GDL, which affects the liquid saturation in the GDL, has been studied by many researches [13, 14, 62]. The liquid saturation in the above studies was derived based on empirical equations and the results were not validated by experiments. Thus, experimental results that can measure liquid water distribution in a PEMFC, and more importantly, results that provide cathode/anode and under channel/under rib differentiation can be very helpful in the advancement of fuel cell models.

The water transport within a cell contains two types of forms, liquid and vapor. It is not easy to directly quantify the liquid water within an operating fuel cell. However, we can detect water vapor by using a relative humidity sensor. Tüber et al. [28] made a transparent fuel cell to observe the liquid water within it, but the cell material was changed and water quantification was not easy to conduct.

Neutron is very sensitive to hydrogen, so neutron radiography provides a non-intrusive method to detect the liquid water inside a fuel cell. In this chapter, we will design fuel cells that enable us to locate and quantify liquid water within operating fuel cells. In addition, we will also use miniature RH sensors to capture the distribution of relative humidity.

3.1 Single Cell Design

Three single cells with different flow fields were designed in this study. The active area of each cell is 100 cm^2. The membrane electrode assembly (MEA) was

provided by Umicore. It has a membrane thickness of 25 μm, a carbon-supported catalyst loading of 0.4 mg Pt cm^{-2} on both anode and cathode, and gas diffusion layers (GDLs). The GDLs are made of carbon papers with an uncompressed thickness of 230 μm. The flow field plates are made of graphite. Because commercial graphite plates have porosity that could trap water—which will interfere with the neutron imaging, the graphite plates were densified with resin before machining.

Most published neutron radiography experiments used identical anode and cathode flow fields for which the water content in the anode flow field and cathode flow field can not be distinguished for the neutron image. In order to differentiate anode flow field from cathode flow field in neutron radiography experiment, a special flow field was designed. One side of flow field is shifted by a channel width, as shown in Figure 3-1. All the anode flow fields were 6-channel serpentine, combined with different straight cathode flow fields. Figure 3-2(a) shows the cathode flow channel is perpendicular to anode flow field. Figure 3-2(b) shows the cathode flow channel is parallel to anode flow field. Figure 3-2(c) shows the cathode channel number reduces from 12 channels to 6 channels. This design was investigated to see whether the reduction in flow area will help to alleviate flooding problem. All channel depth, channel width and rib width were 1, 1.6, and 1.7 mm, respectively. The rectangular holes in those flow fields indicate the sensor locations.

The current collectors are made of gold-plated copper plates. End plates are made of aluminum alloy, used to compress MEAs, flow field plates and current collectors precisely. The cell assembly is compressed by using twelve bolts with nuts. The compression is chosen to compress the thickness of GDL to 184 μm, which is suggested by Umicore. A flow field plate embedded with RH sensors is shown in Figure 3-3. One of the assembled single cells is shown in Figure 3-4.

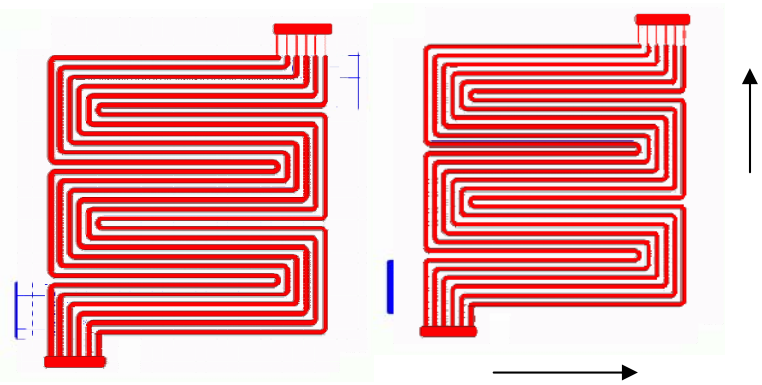

Figure 3-1: Shifted design of flow field to differentiate anode flow field

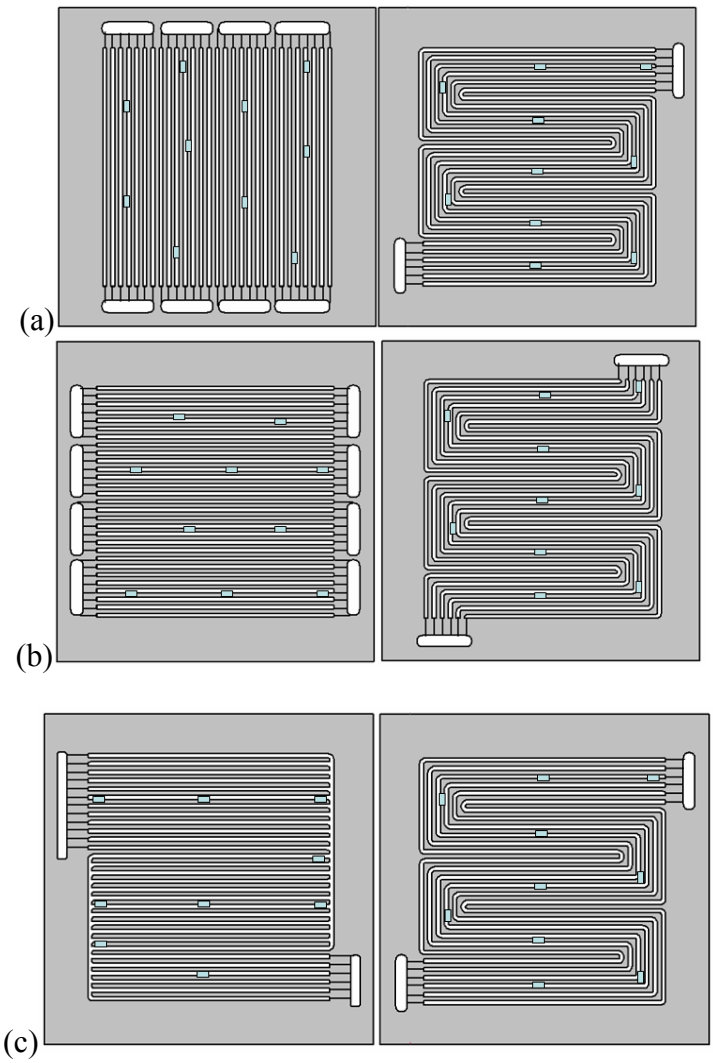

Figure 3-2: Flow field designs in this study (Left: cathode; Right: anode.). (a) Cell no. 1; (b) Cell no. 2; (c) Cell no. 3.

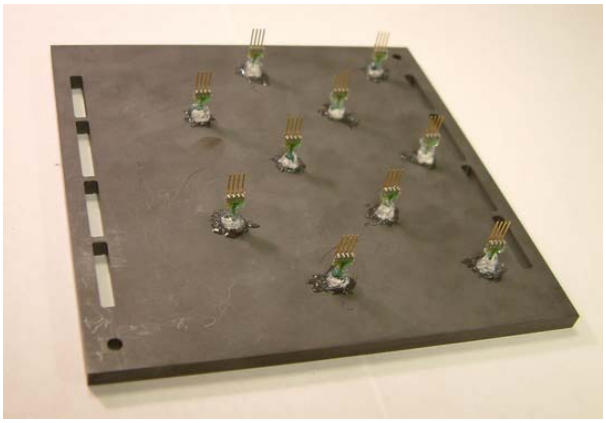

Figure 3-3: A flow field plate embedded with RH sensors

Figure 3-4: An assembled fuel cell

3.2 Relative Humidity Sensors and Calibration

Ten commercial relative humidity sensors (SHT75, Sensirion, Switzerland) were placed at selected positions along the anode channels and cathode channels, respectively. These positions were shown schematically in Figure 3-2. SHT75 is the smallest available sensor we can find on the market. Its cross section area is 3.7 x 2.2 mm. Each sensor was penetrated through a plate such that the sensor head was inside the fuel cell and leading pins were outside the fuel cell, as shown in Figure 3-5. Removable signal cables were connected with the leading pins which transfer digital data to the Evaluation Kit (EK-

H3), shown as Figure 3-6, which is connected to a computer. With evaluation kit and software, temperature, RH and dew point could be measured and recorded for each individual sensor. Therefore, there is no need to install thermocouples.

Figure 3-5: A SHT75 humidity sensor and the cross section view of a sensor embedded

Figure 3-6: Evaluation Kit of Sensirion for humidity sensors.

According to the specification provided by the sensor vendor, the accuracy of the relative humidity (RH) measurement is ±2 %RH when RH is between 10% and 90%. But it was found that not all RH sensors reported the same value under same environment. Therefore, it is necessary to calibrate these RH sensors before they were embedded in fuel cells.

The calibration experiment was conducted at a facility at the Chrysler Technical Center of the DaimlerChrysler Corporation. Figure 3-7(a) shows the humidity generator made by Thunder Scientific Corporation (model number 2500). The specifications of this humidity generator are as follows.

- Relative Humidity Range: 10 to 98%
- Relative Humidity Resolution: 0.02%
- Relative Humidity Accuracy : ±0.5%

Figure 3-7(b) shows the chamber of the humidity generator, which accommodates the RH sensors to be calibrated. The RH sensors were placed inside this chamber and the connected cables went through the hole on the right of the chamber. The RH inside the chamber was set at 60, 70, 80, 90, 95%, respectively. These relatively high levels of RH were selected because they represent the typical operating conditions inside PEMFCs. The Evaluation Kit for the RH sensors was used to process the signal and record the readings from these sensors.

Figure 3-8 shows the calibration results of the 20 RH sensors. The sensors seem to produce readings that can be grouped into two or three batches. The measurement error seems to increase with RH and is as large as 7 %. This large level of error is of course undesirable. Fortunately, the error appears to be very linear for all sensors. Therefore, through a simple post-processing routine the measurement error can be compensated.

Figure 3-7: (a) Model 2500 humidity generator--left; (b) chamber--right.

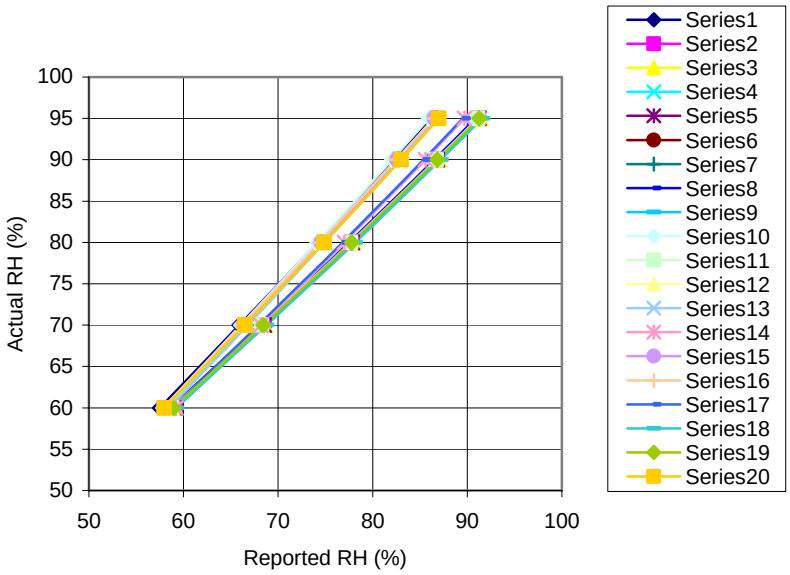

Figure 3-8: The relationship between actual RH value and sensor reading value

3.3 Neutron Radiography

Neutron transmissibility is sensitive to hydrogen, which is an element of water molecule; therefore, neutron radiography provides a non-destructive method to detect liquid water inside an operating fuel cell, since Figure 3-9 shows the comparison of the relative cross-sections of various elements for X-rays and for neutrons. It shows that the hydrogen atom has a high neutron scattering cross section, so that the presence of liquid water causes large changes in the attenuation of the neutron beam.

The transmitted neutron intensity attenuated by any material is given by

$$J = J_0 \exp\left(-\rho d t_w\right) \tag{3.1}$$

where J is the transmitted intensity, J_0 is the incident intensity, ρ is the atom density, and d is the neutron cross-section. In Equation (3.1), if J, J_0, and d are measured, then one can determine the thickness of liquid water t_w. The determination of water content within the cell is attainable by referencing a conversion factor which correlates water thickness to pixel luminance.

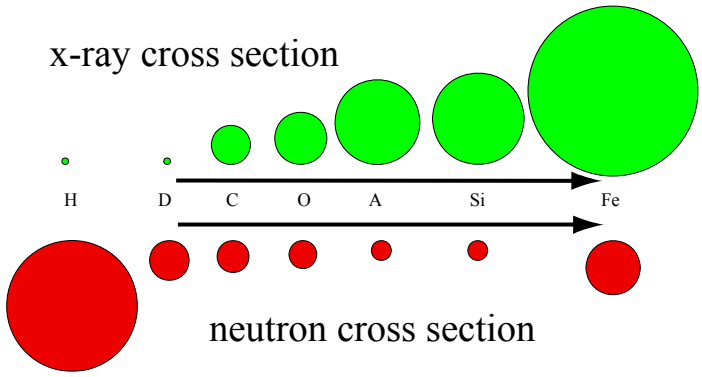

Figure 3-9: Compared with X-ray, neutron is more sensitive to hydrogen [29].

All the experiments were performed at Beam Tube 2 (BT-2) of the Center for Neutron Research (NCNR), a research center of the National Institute of Standards and Technology (NIST). The experimental setup is depicted in Figure 3-10 and a photo of experimental setup is shown in Figure 3-11. The NCNR facility was discussed in the literature [73]. High energy neutrons (MeV) were created by fission in the reactor core and were moderated to thermal energies (meV) by D_2O. The remaining gamma and high energy neutron contribution of the beam was filtered out by a 15 cm thick single crystal bismuth filter that is very transmissive to thermal neutrons when cooled to 77 K by liquid nitrogen. The filtered beam was then collimated with a simple thermal neutron pinhole (made from boron and cadmium) located directly downstream from the filter. In this study, a 2 cm aperture produced an effective L/d ratio of 300 and a neutron fluence rate of 1.7×10^7 cm^{-2} s^{-1}. The images were acquired with a Li^6-doped ZnS scintillator placed directly in contact with an amorphous silicon flat panel detector which has a pixel pitch of 0.127 mm and a spatial resolution of about 0.250 mm at a frame rate of 1 Hz and about 0.125 mm at a frame rate of 15 Hz. The following sections will illustrate the experimental procedure for steady-state and transient images.

3.3.1 Experimental Procedure for Steady-State Images

The fuel cell was controlled by a fuel-cell test station that was custom-built for NIST. This test stand provides accurate flows of humidified hydrogen and air as well as dry nitrogen and pure/nitrogen mixed oxygen. A heat tape wrapped around the perimeter of the cell heated the cell to a temperature of 70 °C. The cell was purged with dry nitrogen and dry air for at least 15 mins prior to taking dry reference images. To reduce

image noise, a series of 1000 images of the dry cell was taken and averaged to obtain the reference image. The water content in the fuel cell is then calculated based on the difference between the test image and the reference image.

The effect of cathode reactant humidity and stoichiometry were investigated in this study. The cell was operated at different current densities, 0, 0.1, 0.2, 0.3, 0.4, 0.5, 0.6, 0.7 A-cm^{-2}. For each current density, the test was conducted at 2 relative humidity values, 50% and 100%, and 3 stoichiometry values, 2, 3, and 4 for the cathode inlet. The anode gas was not humidified and the stoichiometry was 1.2 for all experiments, except that a minimum flow rate for both cathode and anode was set at levels corresponding to 0.2 A cm^{-2}. Neutron imaging was initiated at least 5 mins after a new condition was established.

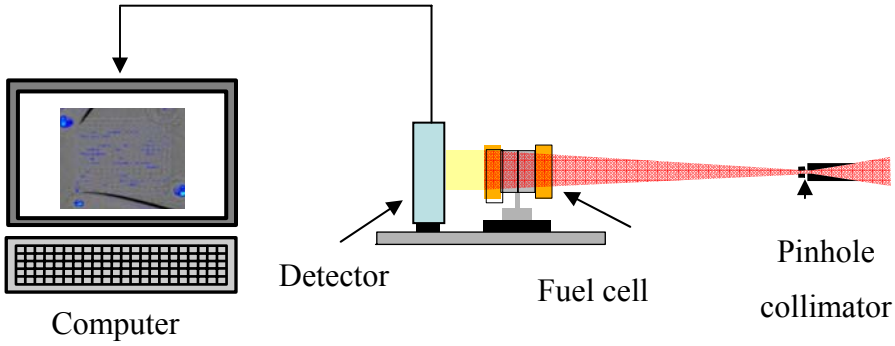

Figure 3-10: Schematic experimental seetup of Neutron Radiography at NCNR

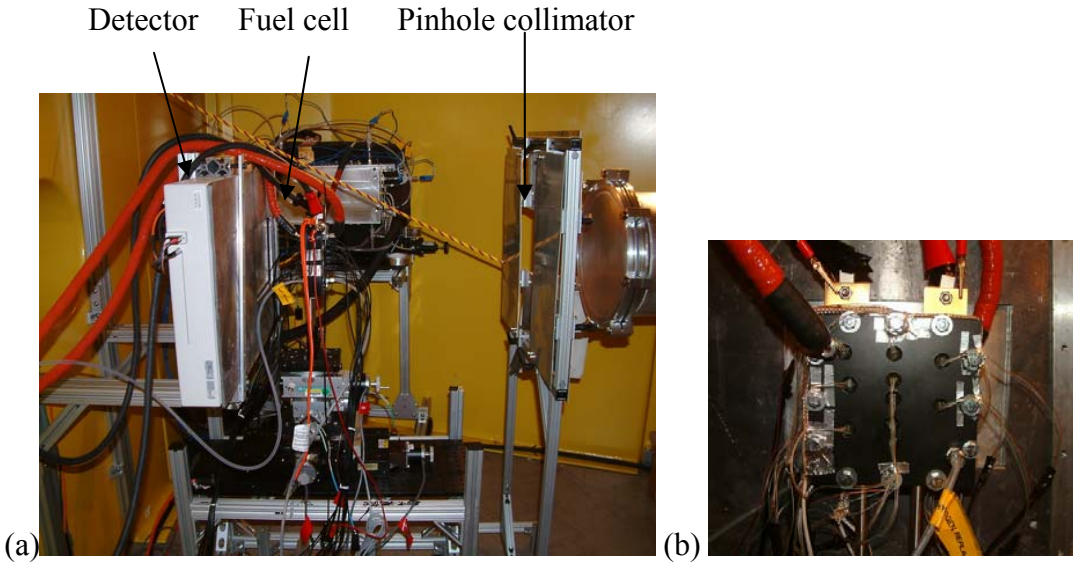

Figure 3-11: (a) Experimental setup at NCNR. (b) Close view of the fuel cell

3.3.2 Experimental Procedure for Transient Images

The purpose of transient images is to study the variation of water content in the fuel cell during step load changes. Seven different changes of current density were selected in this experiment: from 0 to 0.1, from 0.1 to 0.4, from 0.4 to 0.6 (0.7), and from 0.6 (0.7) to 0 A/cm^2.

The experimental setup for transient images was the same with that for steady-state images except the frame rate was set as 15 fps. The anode gas was not humidified and the relative humidity of cathode inlet gas selected at 50% and 100%. The stoichiometry values of anode and cathode were 1.2 and 3, respectively for all experiment except that a minimum flow rate for both cathode and anode was set at levels corresponding to 0.2 A cm^{-2}. At each set of experiments, the current density was changed when the transient images were being recorded. The images were recorded for 3 minutes at a frame rate of 15 fps.

3.4 Data Analysis

Steady-state images and transient images were analyzed by different procedures. The steady-sate images focused on how water content varies with current density, whereas transient images highlight how water content varies during the setup current change.

3.4.1 Data Analysis for Steady-State Images

After the raw images were captured, the water content in the cell was extracted by analyzing the image data using codes developed at NIST. Ten images were used to obtain averaged test data to reduce noise. The image intensity of each pixel of the image reflects the recorded neutron intensity, which quantifies the amount of liquid water at that spatial location. Once the quantity and location of liquid water along the flow-channel direction is determined, the focus shifts to further understanding where liquid water forms along the through-MEA direction. The PEM is quite thin and hydrophilic; therefore the water content in it typically remains relatively constant and does not influence the observed water quantity in a neutron image. In an earlier study [18], where an un-shifted flow field

design was used, the water content "under channel" was found to be much less than that "under ribs," and the amount of water under channel does not change significantly with current density. The under-saturated test conditions reported in another study [17] showed similar results. These earlier results imply that the liquid water has a tendency to accumulate in the GDLs under the ribs, and the quantity can vary significantly. Water that is present in the channels, on the other hand, is carried through the flow channel and its quantity is relatively fixed. The above two papers both used fuel cells with a small active area and straight flow channels. Therefore, the water distribution within the active area is quite uniform. Since the anode flow field was identical to the cathode flow field in their designs, the area that was identified by the neutron image to have liquid water under channel is at locations where anode channels and cathode channels overlap (referred to as "Ch-Ch"), whereas the area under ribs is at locations where anode ribs and cathode ribs overlap ("Rib-Rib").

In this research, since the flow fields of anode and cathode are not identical and are shifted spatially, there are two additional combinations. The two additional types of areas, which in fact accounts for the majority of the active area, were the overlap of cathode channels and anode ribs (which we will call An_rib), and that of anode channels and cathode ribs (Ca_rib), as shown in Figure 3-12. To quantify liquid water in the four different areas, image masking techniques were used to determine the location of water inside the cell. Image masking refers to the process in which all neutron intensity in an image is blocked except for pixels that lie within a specified region. Four masks were created to quantify liquid water in the four different areas, as shown in Figure 3-13. Another important consideration is that active area was not small enough to be regarded as uniform, so the active area was divided into fifteen segments along the anode flow field, as shown in Figure 3-14, which is numbered successively along the anode flow direction. The average liquid water thickness was then calculated for each mask in each of the fifteen segments. The quantification result is the average thickness for each segment, for the four different types of area. The water thickness in the plots cannot be interpreted as the thickness of liquid water accumulated in any specific layer because the equivalent water thickness of each layer in MEA is unknown.

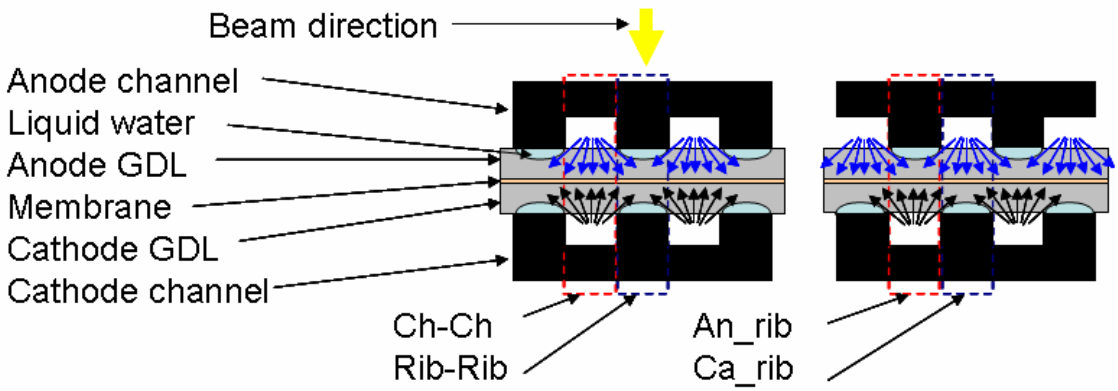

Figure 3-12: Schematic of four kinds of channel/rib combinations and water accumulation.

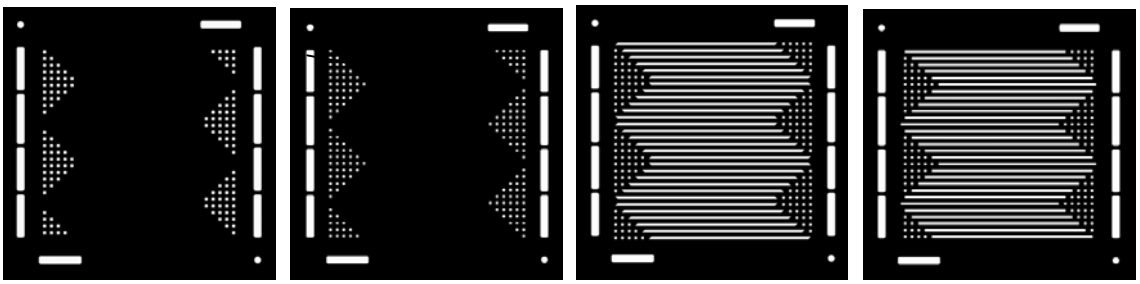

Figure 3-13: Four masks used to quantify liquid water in (a) Rib_Rib; (b) Ch_Ch; (c)Ca_rib; (d) An_rib.

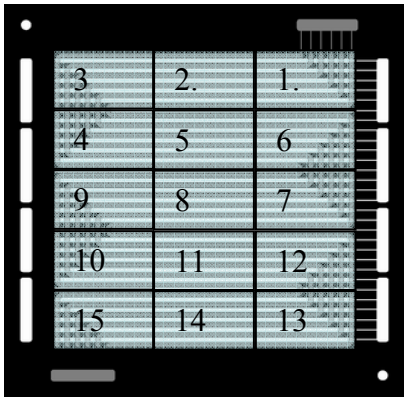

Figure 3-14: Schematic of 15 segments along anode flow field.

3.4.2 Data Analysis for Transient Images

In processing transient results, ten images were used to obtain moving average images. The procedure was illustrated in Figure 3-15. The same four masks shown in

Figure 3-13 were also applied to differentiate the water content in four areas. The average liquid water thickness was then calculated for each mask in the fifteen segments shown in Figure 3-14.

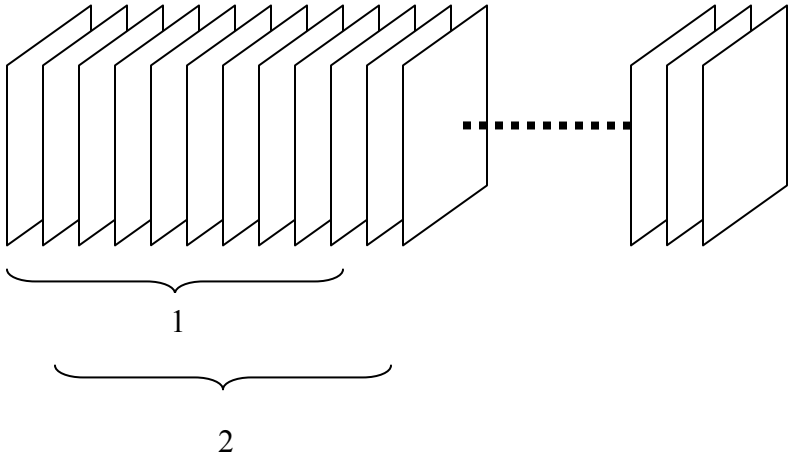

Figure 3-15: Schematic of obtaining moving average images.

3.5 Neutron Radiography Experimental Results

The calculated average liquid water quantity can be used for qualitative and quantitative assessment. The water quantity can be used for the calibration and validation of a mathematical model. In addition, we can also use it as a visualization tool, through colorizing the neutron density images. Figure 3-16 shows a colorized neutron image of cell No. 2, whose flow field pattern is shown in Figure 3-2 (b). The bottom half of the image, which corresponds to the downstream anode flow, contains more water than the top half. However, it is not possible to distinguish from this image whether the water accumulation is located in the membrane, anode/cathode channels, or anode/cathode GDLs. By applying the masking technique described earlier, however, we will be able to identify the location of liquid water more accurately.

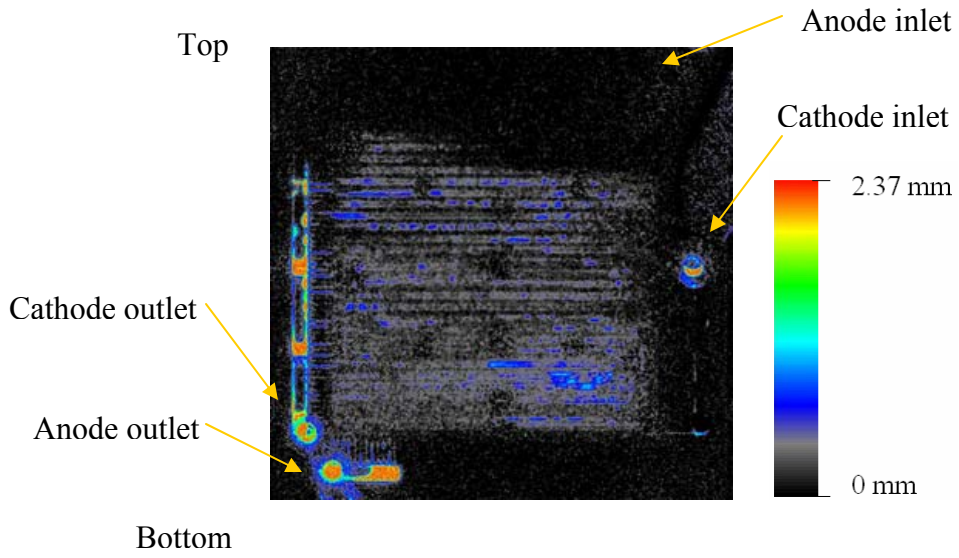

Figure 3-16: Colorized neutron image of cell No. 2. Current density: 0.2 A/cm^2; Anode/Cathode inlet RH: 0% / 100%.

3.5.1 Anode and Cathode Differentiation

First, we will show that the flow field design and image processing technique developed in this study help in differentiating liquid water in the anode and in the cathode. Figure 3-17 shows the average water thickness in the 15 segments as a function of current density by using Rib-Rib (a), Ch-Ch (b), Ca_rib (c), and An_rib (d) masks, when the cathode inlet RH is fixed at 50%. Figure 3-18 shows the results when the cathode inlet air is fully humidified. The layout of the subplot matrix corresponds to the segment distribution in Figure 3-14. In the middle columns of Figure 3-17 (a)-(b) and Figure 3-18 (a)-(b), the plots show nothing, because there are no Ch-Ch and Rib-Rib areas in those segments. In Figure 3-17 (a) and Figure 3-18 (a), which show results for application of the Rib-Rib mask, a maximum water thickness of approximately 100 μm was observed in segment 15. Since segment 15 is the last one along the anode flow field, it is reasonable for it to contain the most liquid water. The results imply that the maximum amount of liquid water that can accumulate in the Rib-Rib area is equivalent to the water thickness of around 100 μm. So when we observe water thickness in excess of 100 μm, it is very likely the amount over 100 μm is due to liquid water in the flow channels.

The water thickness in Figure 3-17 (d) was observed to decrease slightly with increasing current density. This phenomenon becomes more pronounced when the cathode inlet gas was fully humidified, as is displayed in Figure 3-18 (d). The water thickness in Figure 3-18 (d) decreases to 20-80 μm, depending on the segment position. Figure 3-18 (a) and (b) show that the water thickness in the Rib-Rib and Ch-Ch areas of segments 1, 6, 7, 12, and 13 does not significantly change with current density. However, the water thickness in the Ca_rib and An_rib areas of these segments decreases with current density, as shown in Figure 3-18 (c) and (d). This result suggests the decrease in Ca_rib and An_rib areas is due to the water content in the GDLs under the ribs. This trend was also observed in the operating conditions with fully humidified or over-humidified inlet gas reported by Turhan et al. [17]. This phenomenon is perhaps related to water transport by electro-osmotic drag from anode to cathode, which is highly related to current density [66]. Another possible explanation of this phenomenon is the changing flow rate. At fixed stoichiometric value, the gas flow rate varies proportionally with current density. Since in this study only the cathode gas is humidified and the anode gas is dry, water in the anode GDL has the tendency to move into the channels through convective mass transfer. Therefore, high flow rate, resulting from high current density, reduces the total amount of water measured in the neutron image. Both explanations seem to be plausible and in fact could co-exist.

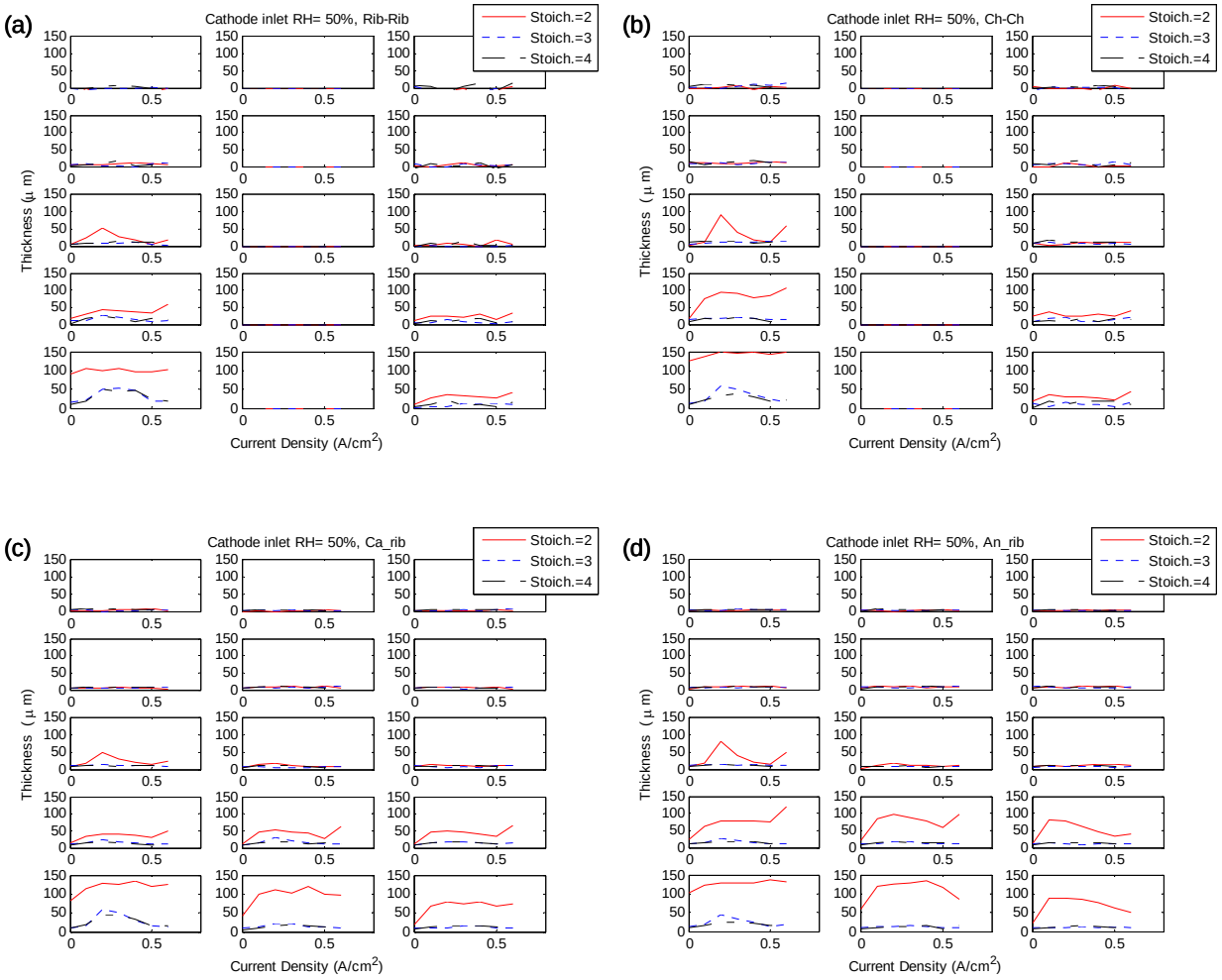

Figure 3-17: Water distribution within the cell in the area of (a) Rib-Rib; (b) Ch-Ch; (c)Ca_rib; (d) An_rib when the cathode inlet relative humidity is 50%. (cell No. 2)

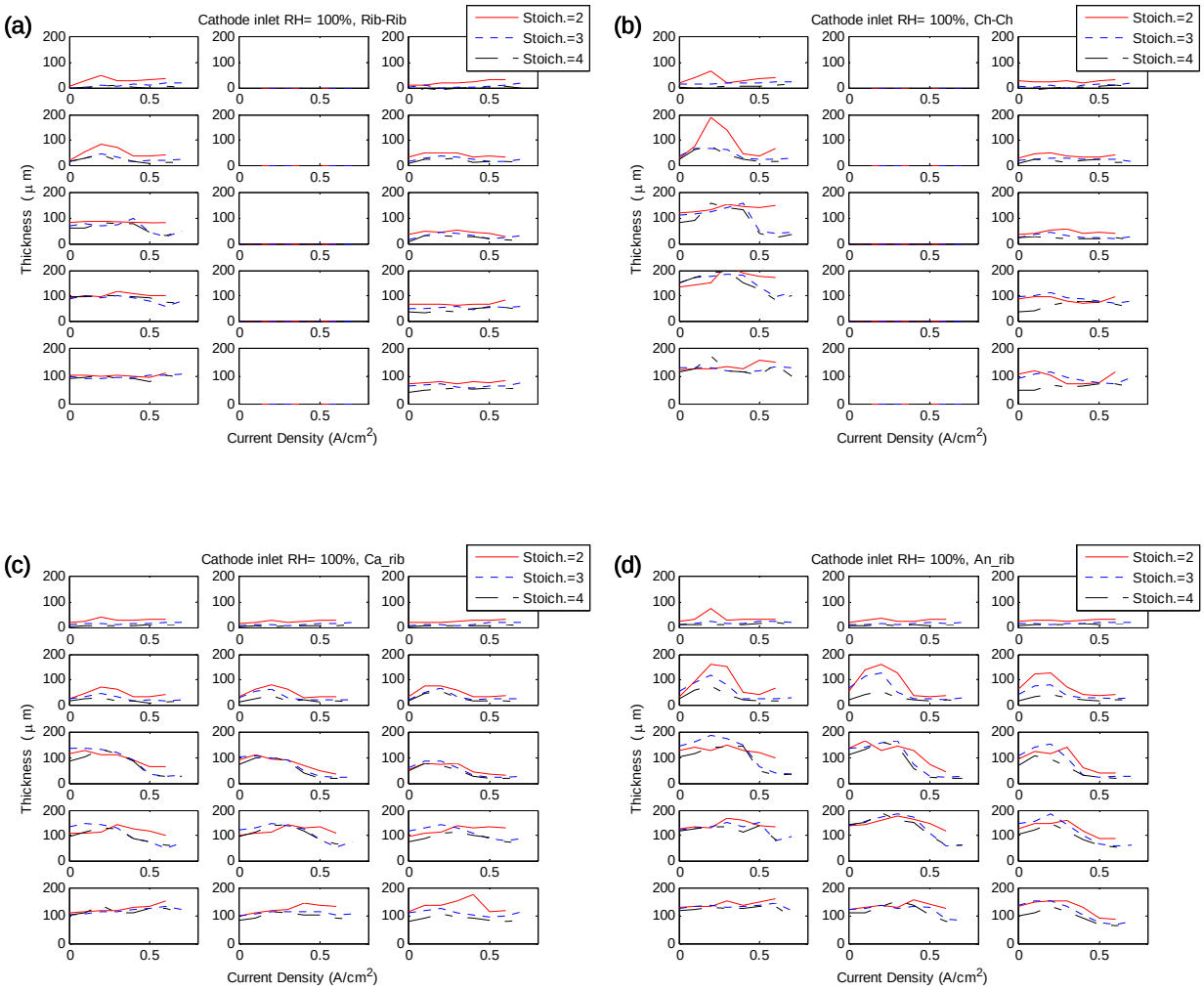

Figure 3-18: Water distribution within the cell in the area of (a) Rib-Rib; (b) Ch-Ch; (c)Ca_rib; (d) An_rib when the cathode inlet relative humidity is 100%. (cell No. 2)

3.5.2 Effect of Cathode Inlet Stoichiometry

Three different cathode inlet stoichiometry values were tested to study the impact of flow rate on water quantity and distribution. In Figure 3-17 and Figure 3-18, it is observed that at high current densities, experiments at a low stoichiometry value of 2 result in noticeably higher water content in the GDLs. This is because when the gas flow rate is low, less water is taken away, resulting in more water accumulation in the GDLs. This phenomenon is more significant when the cathode inlet RH is low. Figure 3-19 shows the water content in the An_rib area and Ca_rib area along the anode flow channel when the cathode inlet RH is 50%. The numbers in the abscissa denote segment number.

At the low stoichiometry value of 2, a significant amount of water in those areas was observed. However, the segments near the inlet do not contain much liquid water. Starting from segment number 8 or 9, the water thickness increases toward a maximum of about 120 μm. When the stoichiometry value is higher at 3 or 4, the water thicknesses in the Ca_rib or An_rib area vary from 0 to approximately 15 μm along the anode flow field. These values do not change significantly with current density. Liu's work [74] showed that when inlet RH is low, the upstream segments have lower current densities. Lower current density is accompanied by weaker electro-osmotic drag from anode to cathode and less water generation in the cathode. Therefore, the cathode side could be under-saturated, which contributes to higher resistivity and lower current density. Figure 3-20 shows a similar trend when cathode inlet RH was 100%. In addition, the water profile along the anode flow channel seems to be similar for all stoichiometric values. In Figure 3-20 (a), it can be seen that at low current densities of 0.1 to 0.3 A cm^{-2}, the amount of liquid water starts to increase from segment 3, whereas at high current densities, it starts to increase from segment 7. In Schneider's study [75], both distributed current densities and water content were measured and the results support similar trends to this work. Schneider found similar profile for current density distribution and water content distribution, followed a similar profile. Our study shows similar trend with theirs [74, 75]. The trend indicates that current density distribution is more even under low load than under high load.

At each current density, the cell voltage was recorded as the main indicator of cell performance. Figure 3-21 compares polarization curves obtained while different stoichiometry values of cathode inlet gas were fed to the cell under two different RH conditions. Regardless of the value of RH, lower cathode stoichiometry appears to result in lower performance. When the stoichiometry is 2, the polarization curve does not seem to be sensitive to cathode inlet RH despite the fact that the water content in the GDL is quite different. This implies that at low stoichiometry, water accumulation in the GDL is not correlated to low performance. For current densities between 0.1 and 0.5 A cm^{-2}, which are in the ohmic polarization region, it is very likely the low performance is due to low membrane water content instead of flooding. At lower cathode flow rate, little water is carried to the membrane, which causes low membrane hydration and low membrane

conductivity. Therefore, cell performance is low even when the cathode inlet gas is fully humidified.

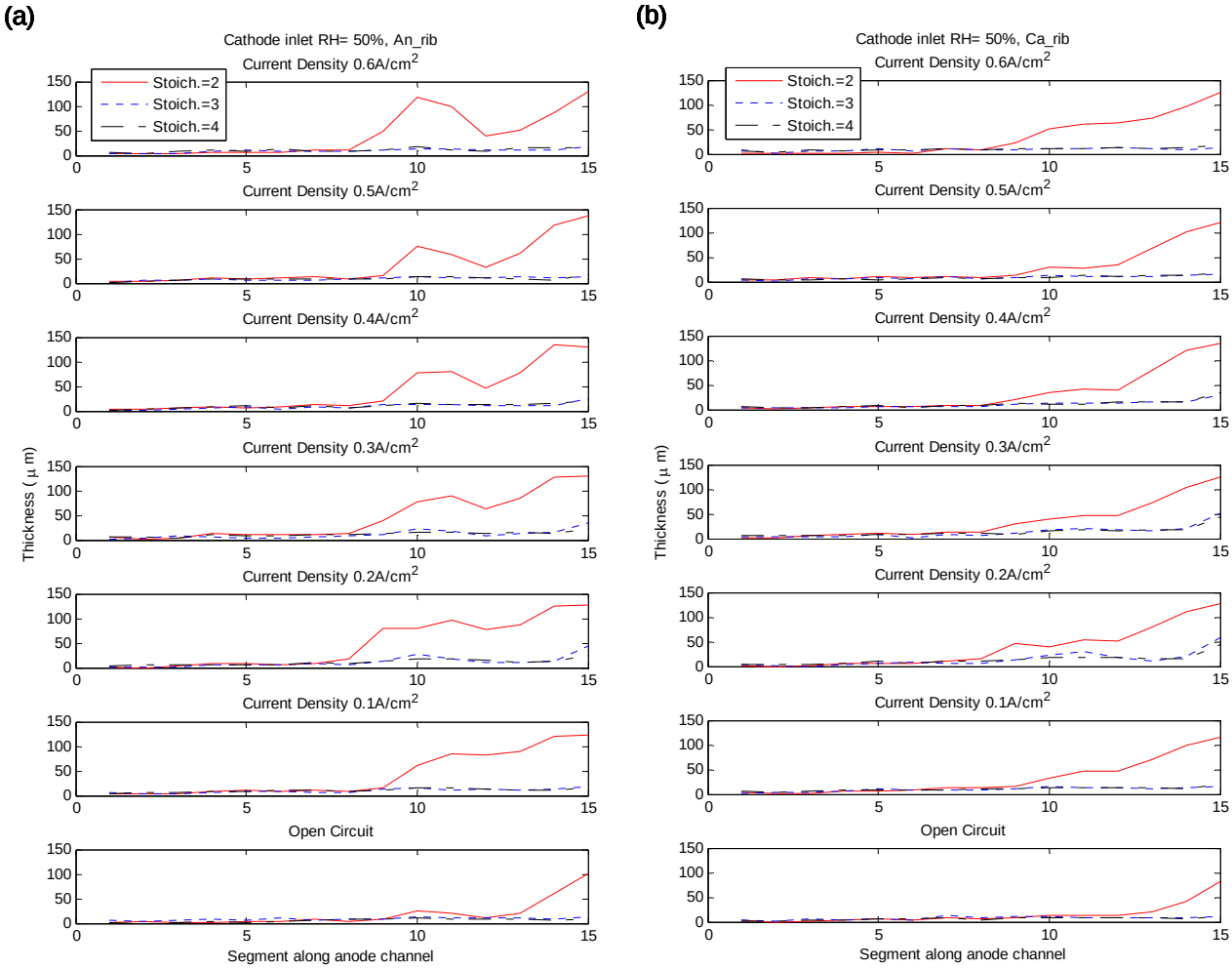

Figure 3-19: Water distribution along anode flow field by using (a) Ca_rib mask; (b) An_rib mask, when cathode inlet relative humidity is 50%. (cell No. 2)

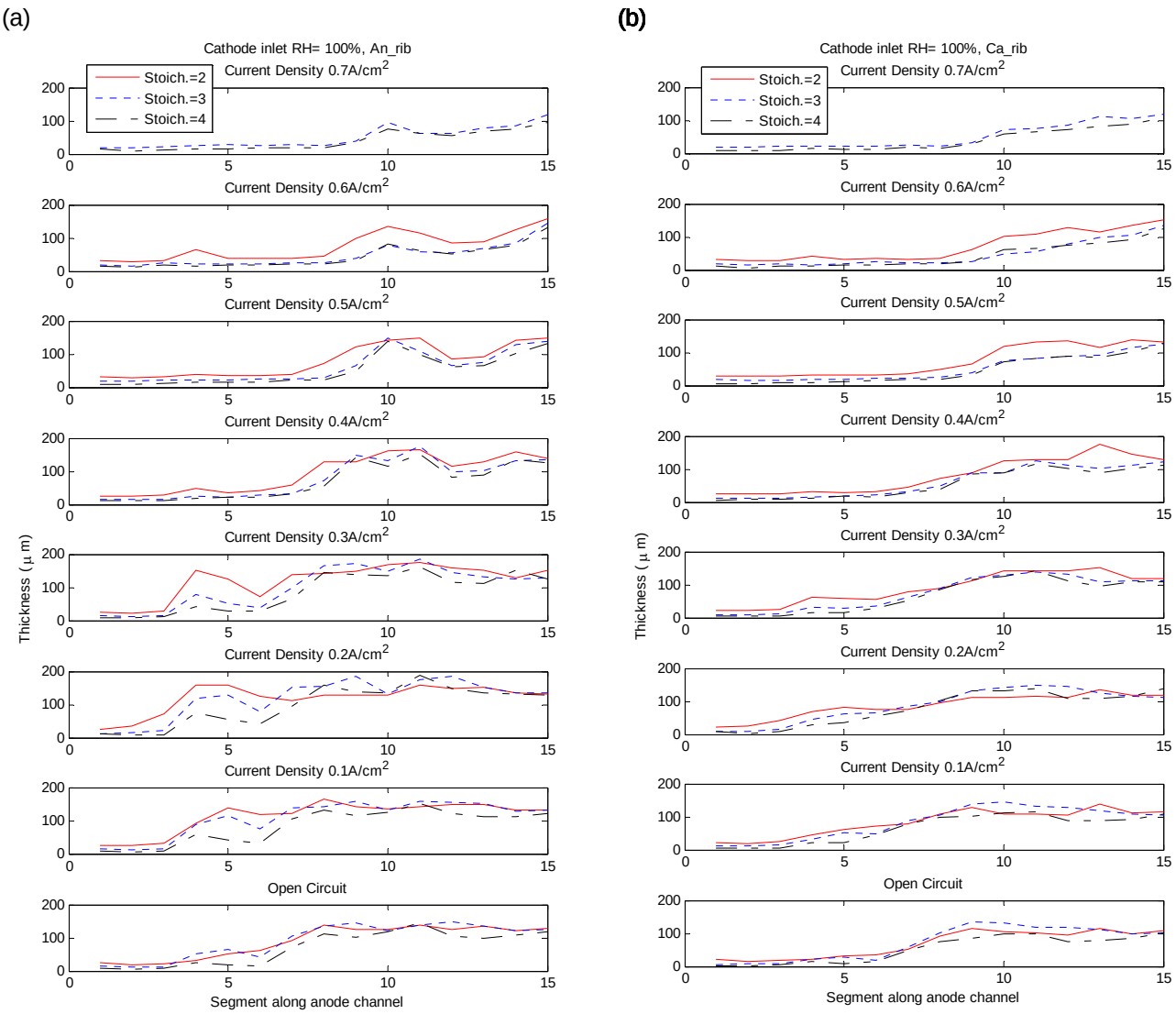

Figure 3-20: Water distribution along anode flow field by using (a) Ca_rib mask; (b) An_rib mask, when cathode inlet relative humidity is 100%. (cell No. 2)

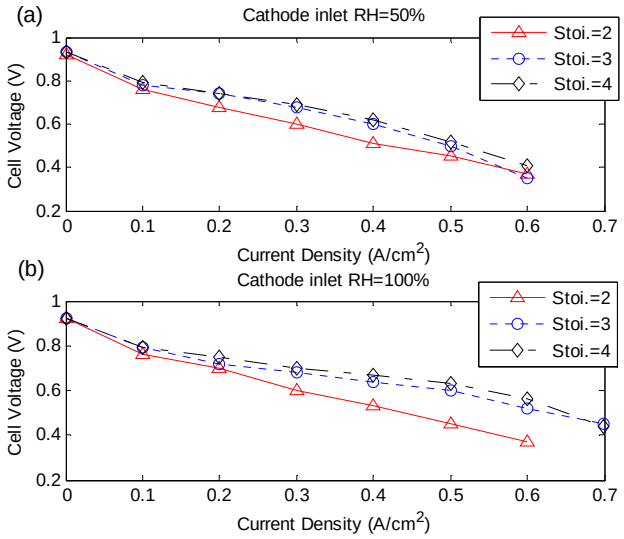

Figure 3-21: Polarization curves of cell No. 2 when cathode inlet relative humidity is (a) 50%; (b) 100%.

3.5.3 Effect of Cathode Inlet Relative Humidity

The effect of reactant relative humidity (RH) on the water accumulation in the GDLs is investigated in this study at two different RH levels: 50% and 100%. The effect of cathode inlet RH can be studied by comparing Figure 3-19 and Figure 3-20. When the cathode inlet gas is 50% (thus under-saturated), it takes water from the GDL through convective mass transfer [12]. When under-saturated cathode gas with stoichiometry of 3 or 4 is fed to the cell, the water thickness in the Ca_rib area is approximately 20 μm; however, the water thickness is apparently larger at low stoichiometry of 2. If a fully saturated cathode gas is fed to the fuel cell, the water content in the area increases and stoichiometry value has little effect on the water content. From Figure 3-20 (b), the water content profiles in the last several segments seem to be fully developed. The maximum water thickness in the Ca_rib area is approximately 120 μm, which could be the maximum amount of water that can accumulate in the GDL under those operating conditions. Since the GDL cannot hold any more water, once the water is generated in the cathode catalyst layer, the water is expelled from the hydrophobic GDL into the channels. If the flow field design can not remove liquid water effectively, flooding will occur.

Since the anode gas is not humidified in this study, the only way for the anode side to acquire water is through the back diffusion mechanism, which carries water from

the cathode to the anode. Water transport by back diffusion not only counter-balances the electro-osmotic drag from anode to cathode, but also compensates for the water loss in the GDL caused by dry flowing anode gas. Through the back-diffusion mechanism, the water content in the anode GDL is not necessarily lower, and sometimes could actually be higher than that in the cathode GDL, as can be seen by comparing Figure 3-20 (a) and (b). At high current densities, however, the anode GDL generally contains less water than the cathode GDL because the electro-osmotic drag becomes more significant and more liquid water transports from anode to cathode.

The polarization curves in Figure 3-21 show that under the same stoichiometry, the cell has lower performance when the cathode inlet RH is low. This is likely due to insufficient water in the inlet air to humidify the membrane from the cathode side. In Figure 3-21 (b), the cell voltages were unstable at the operating condition of 0.7 A cm^{-2} for all three stoichiometry values. It is possible that; because the cathode is fully saturated, the unstable voltages are caused by flooding in the cathode GDL, especially for those segments near the outlet.

As a final note, the cell voltage measured in our experiment seems to be lower than values reported in typical fuel cell papers. Although we were not able to pinpoint the root cause, there are at least two possible explanations. First, since the flow channel is shifted to improve visualization, it might have unintentional adverse effects on the gas diffusion in the GDL, for example, due to the "cross bite" of the ribs of the graphite plates. It is also possible that even though we used the compression ratio suggested by Umicore, the suggested value is optimized for "regular" cell designs instead of our cross-bite design. Since the focus of this experiment is on water distribution rather than cell performance, the low cell voltage could be a concern because we could not run higher current densities, but not a flaw.

These experiments, in combination with our specially designed flow fields and image processing technique, provide a new way to investigate liquid water distribution in anode and cathode. The results show the effects of relative humidity and stoichiometry of cathode inlet on water accumulation as well as cell performance. These new results still provide some interesting insight to the field of fuel cell water management, prediction, and control.

3.5.4 Channel and GDL Differentiation

By using the specially designed cells, we can differentiate the liquid water in four areas by neutron radiography experiments; however, we still cannot differentiate the liquid water in the GDL under the channel and water in the flow channel. Liquid water within a PEMFC could accumulate in six types of locations, as shown in Figure 3-22: anode channel (A_c), anode GDL under the channel (A_{gc}), anode GDL under the rib (A_{gr}), cathode channel (C_c), cathode GDL under the channel (C_{gc}), and cathode GDL under the rib (C_{gr}).

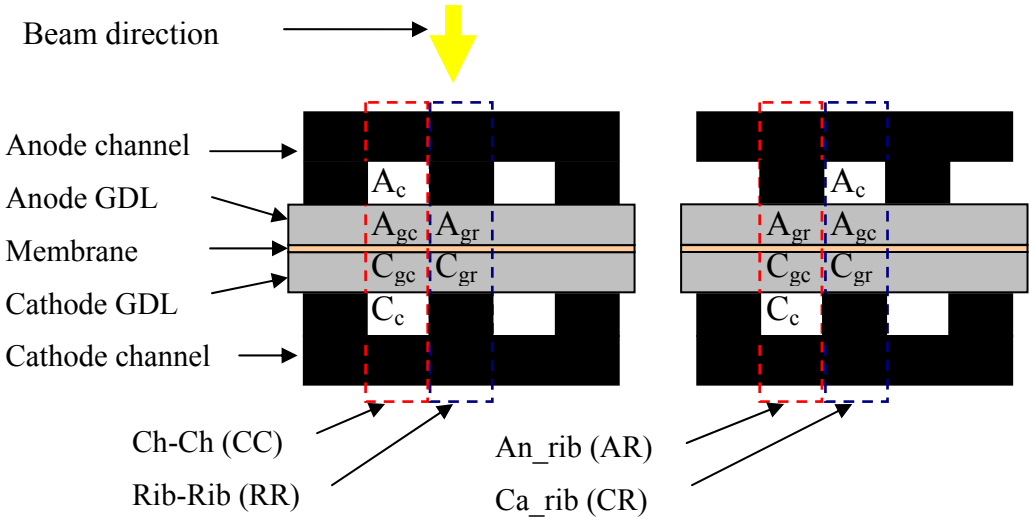

Figure 3-22: Schematic of water accumulation in six areas.

We can express the relationship between water thicknesses in those six locations and measured data Rib-rib (*RR*), Channel-Channel (*CC*), Cathode_rib (*CR*) and Anode_Rib (*AR*) as

$$\begin{aligned} A_{gr} + C_{gr} &= RR \\ A_c + A_{gc} + C_{gc} + C_c &= CC \\ A_c + A_{gc} + C_{gr} &= CR \\ A_{gr} + C_c + C_{gc} &= AR \end{aligned} \tag{3.2}$$

or in a matrix form

$$\mathbf{Ax} = \mathbf{b} \tag{3.3}$$

where

$$\mathbf{A}=\begin{bmatrix}0&0&1&0&0&1\\1&1&0&1&1&0\\0&0&1&1&1&0\\1&1&0&0&0&1\end{bmatrix},\ \mathbf{x}=\begin{bmatrix}C_c\\C_{gc}\\C_{gr}\\A_c\\A_{gc}\\A_{gr}\end{bmatrix},\ \mathbf{b}=\begin{bmatrix}RR\\CC\\CR\\AR\end{bmatrix} \tag{3.4}$$

There are six unknowns and four equations for each of the 15 segments. Overall, there are ninety unknowns and sixty equations. We can solve the water content in fifteen segments at the same time. The relationship between water content in ninety locations and sixty measured data is expressed in an augmented matrix form:

$$\begin{bmatrix}\mathbf{A}&\mathbf{O}&\mathbf{O}&\mathbf{O}&\cdots&\mathbf{O}\\\mathbf{O}&\mathbf{A}&\mathbf{O}&\mathbf{O}&\cdots&\mathbf{O}\\\mathbf{O}&\mathbf{O}&\mathbf{A}&\mathbf{O}&\cdots&\mathbf{O}\\\mathbf{O}&\mathbf{O}&\mathbf{O}&\mathbf{A}&\cdots&\mathbf{O}\\\vdots&\vdots&\vdots&\vdots&\ddots&\vdots\\\mathbf{O}&\mathbf{O}&\mathbf{O}&\mathbf{O}&\cdots&\mathbf{A}\end{bmatrix}\begin{bmatrix}\mathbf{x_1}\\\mathbf{x_2}\\\mathbf{x_3}\\\mathbf{x_4}\\\vdots\\\mathbf{x_{15}}\end{bmatrix}=\begin{bmatrix}\mathbf{b_1}\\\mathbf{b_2}\\\mathbf{b_3}\\\mathbf{b_4}\\\vdots\\\mathbf{b_{15}}\end{bmatrix} \tag{3.5}$$

where $\mathbf{A}$, $\mathbf{x}_i$ and $\mathbf{b}_i$ are defined in Equation (3.4) for i-th segment. $\mathbf{O}$ is a zero matrix with the same size as $\mathbf{A}$.

Equation (3.5) is an under-determinant problem and a unique solution does not exist. In addition, matrix $\mathbf{A}$ is not full rank because A_{gc} and A_c always co-exist, and C_{gc} and C_c always co-exist. Since A_{gc} and A_c are not differentiable, they are considered as a single unknown, and so are C_{gc} and C_c. Then there are four unknowns and four measurements in each segment; A_{gr} and C_{gr} can be solved exactly.

After the above procedure, thirty unknowns are solved, and sixty unknowns remain; however, there are only forty-five equations left. The problem is still "too under-determinant" to yield accurate data. To reduce the number of unknowns, we need to make an assumption. According to Turhan [17], liquid water inside a fuel cell significantly decreases with increasing gas flow rate. This is because GDL is made of hydrophobic and porous materials, large gas flow rate helps push liquid water out from the GDL, resulting less liquid water accumulation in the GDL. To simplify the problem, the water

thicknesses in the GDL under the channel are assumed to be inversely proportional to the gas flow rate:

$$C_{gc} = \frac{\alpha}{N_{ca}}$$
$$A_{gc} = \frac{\beta}{N_{an}} \tag{3.6}$$

Under these assumptions, the remaining unknowns and equations are expressed as

$$\begin{bmatrix} \mathbf{S} & \mathbf{O} & \mathbf{O} & \mathbf{O} & \cdots & \mathbf{O} & \mathbf{a}_1 & \mathbf{b}_1 \\ \mathbf{O} & \mathbf{S} & \mathbf{O} & \mathbf{O} & & \mathbf{O} & \mathbf{a}_2 & \mathbf{b}_2 \\ \mathbf{O} & \mathbf{O} & \mathbf{S} & \mathbf{O} & & \mathbf{O} & \mathbf{a}_3 & \mathbf{b}_3 \\ \mathbf{O} & \mathbf{O} & \mathbf{O} & \mathbf{S} & & \mathbf{O} & \mathbf{a}_4 & \mathbf{b}_4 \\ \vdots & \vdots & \vdots & \vdots & \ddots & \vdots & \vdots & \vdots \\ \mathbf{O} & \mathbf{O} & \mathbf{O} & \mathbf{O} & \cdots & \mathbf{S} & \mathbf{a}_{15} & \mathbf{b}_{15} \end{bmatrix} \begin{bmatrix} \mathbf{y_1} \\ \mathbf{y_2} \\ \mathbf{y_3} \\ \mathbf{y_4} \\ \vdots \\ \mathbf{y_{15}} \\ \alpha \\ \beta \end{bmatrix} = \begin{bmatrix} \mathbf{T_1} \\ \mathbf{T_2} \\ \mathbf{T_3} \\ \mathbf{T_4} \\ \vdots \\ \mathbf{T_{15}} \end{bmatrix} \tag{3.7}$$

where

$$\mathbf{S} = \begin{bmatrix} 1 & 1 \\ 0 & 1 \\ 1 & 0 \end{bmatrix},\ \mathbf{O} = \begin{bmatrix} 0 & 0 \\ 0 & 0 \\ 0 & 0 \end{bmatrix},\ \mathbf{a}_i = \begin{bmatrix} \frac{1}{N_{ca,i}} \\ 0 \\ \frac{1}{N_{ca,i}} \end{bmatrix},\ \mathbf{b}_i = \begin{bmatrix} \frac{1}{N_{an,i}} \\ \frac{1}{N_{an,i}} \\ 0 \end{bmatrix},\ \mathbf{y}_i = \begin{bmatrix} C_{c,i} \\ A_{c,i} \end{bmatrix},\ \mathbf{T}_i = \begin{bmatrix} NewCC_i \\ NewCR_i \\ NewAR_i \end{bmatrix} \tag{3.8}$$

In the vector $\mathbf{T}_{i,}$

$$NewCC_i = CC_i - C_{gr,i} - A_{gr,i}$$
$$NewCR_i = CR_i - C_{gr,i} \tag{3.9}$$
$$NewAR_i = AR_i - A_{gr,i}$$

By using least-squares method (LSM), we can solve Equation (3.7) to find out $C_{c,i}$, $A_{c,i}$, α, and β. From Equation (3.6), C_{gc} and A_{gc} can then be solved.

3.5.5 Steady-State Conditions

Figure 3-23 to Figure 3-27 show the results of using LSM to differentiate water accumulation in the six locations for three single cells at different operating conditions. The flow field patterns of these three cells are shown in Figure 3-2. Figures (d) and (f) in above figures suggest that water thickness in the anode GDLs decreases when current density is high. This phenomenon becomes more pronounced when the cathode inlet RH is 100%. The decrease of water content at high current density is likely due to the water transport by electro-osmotic drag from anode to cathode. Another possible reason is the high gas flow rate at high current density. Higher flow rate gas takes more liquid water out from the GDLs.

Figures (c) (from Figure 3-23 to Figure 3-27) show little liquid water in the cathode GDL under the channel. This trend was also observed in Zhang's study [18] when the reactants were fully humidified. A possible reason is that due to the high stoichiometric value in the cathode side, the flow rate in the cathode is higher than that in the anode. Figure 3-23 to Figure 3-27 also show that water content at a low stoichiometry value is slightly more than that at a high stoichiometry value. This is because when the gas flow rate is low, less water in the GDLs is carried away by the gas flow, resulting in more water accumulation in the GDLs.

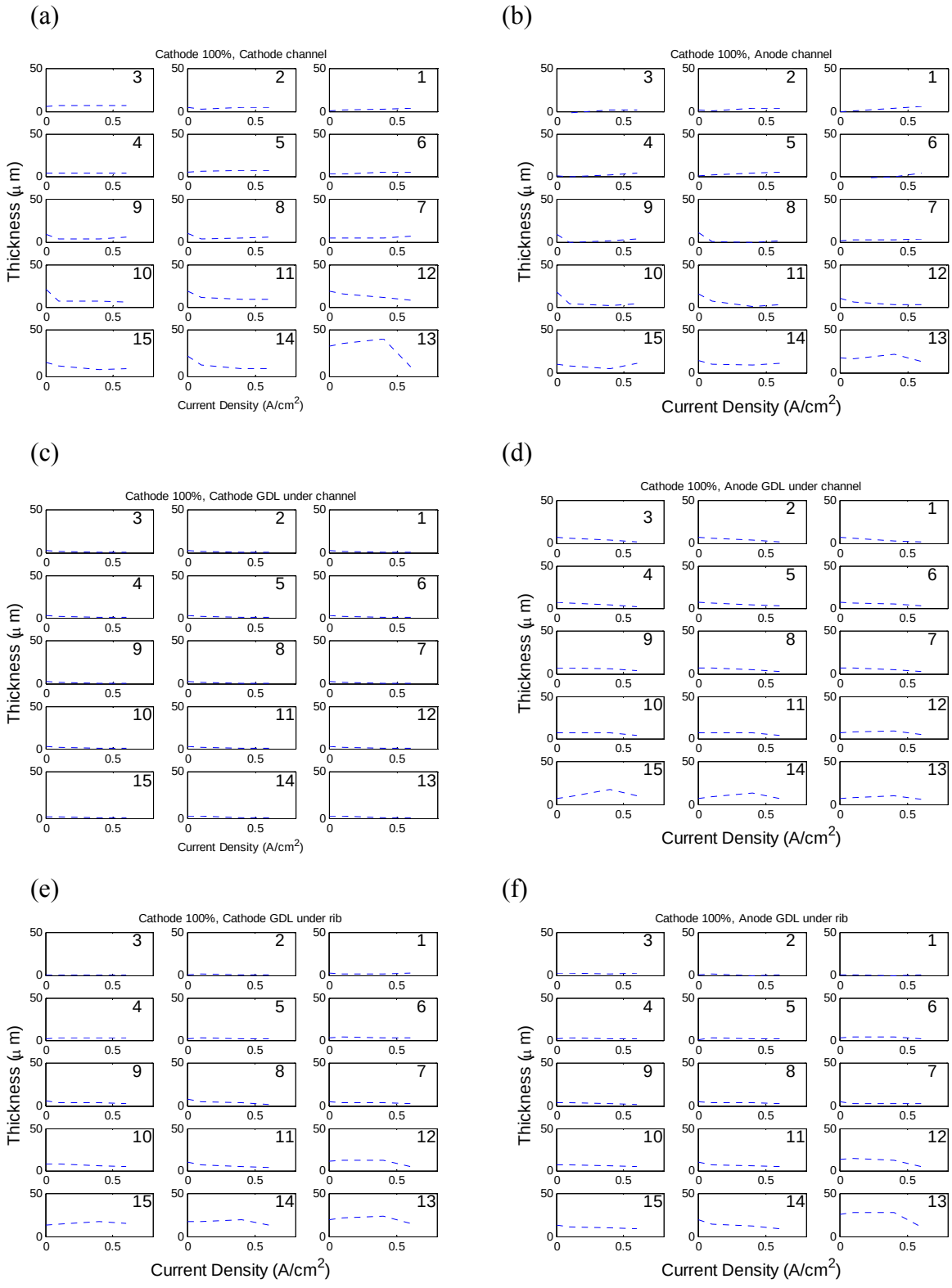

Figure 3-23: Liquid water accumulation at six locations of cell No. 1 at steady state condition (cathode inlet RH=100%).

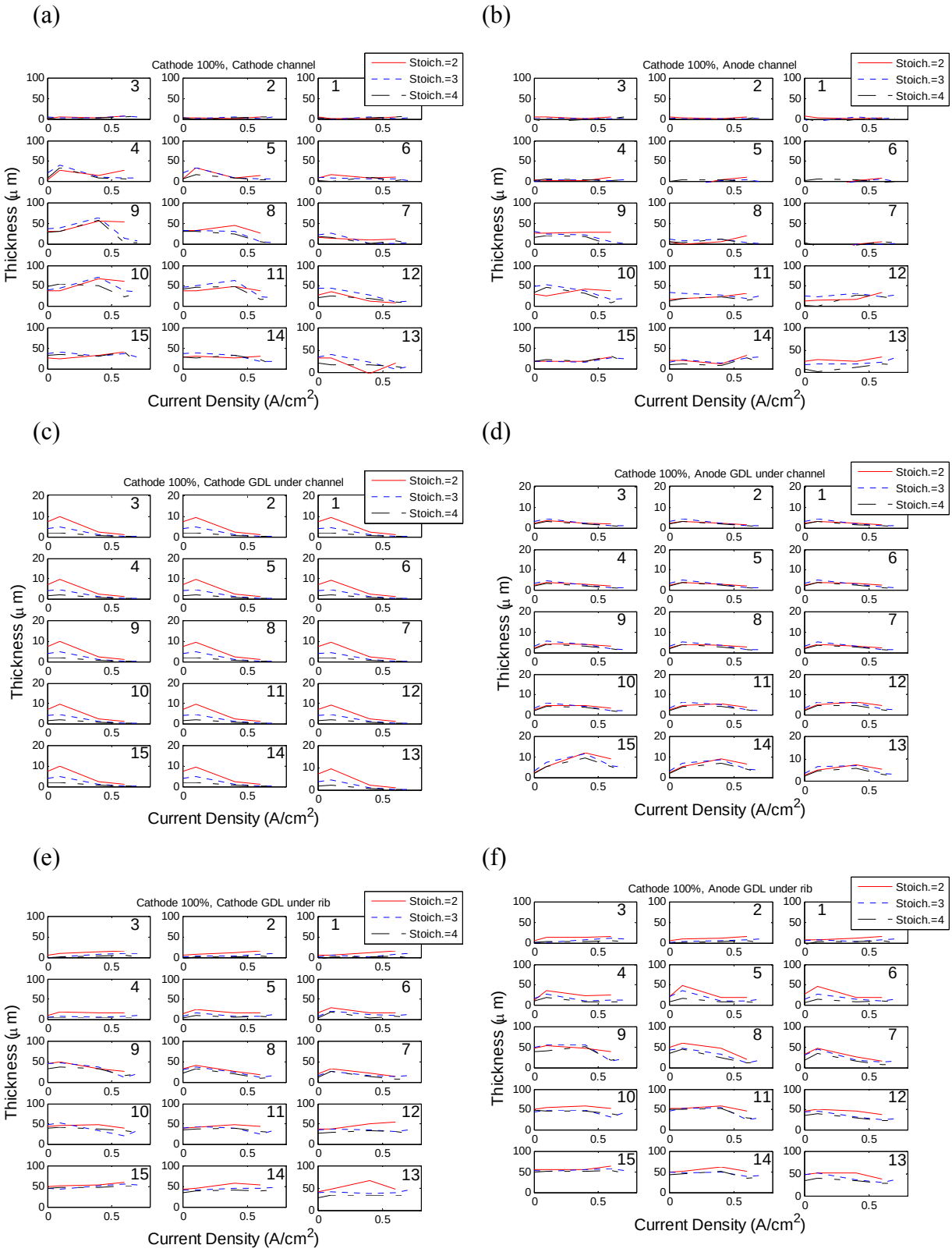

Figure 3-24: Liquid water accumulation at six locations of cell No. 2 at steady state condition (cathode inlet RH=100%).

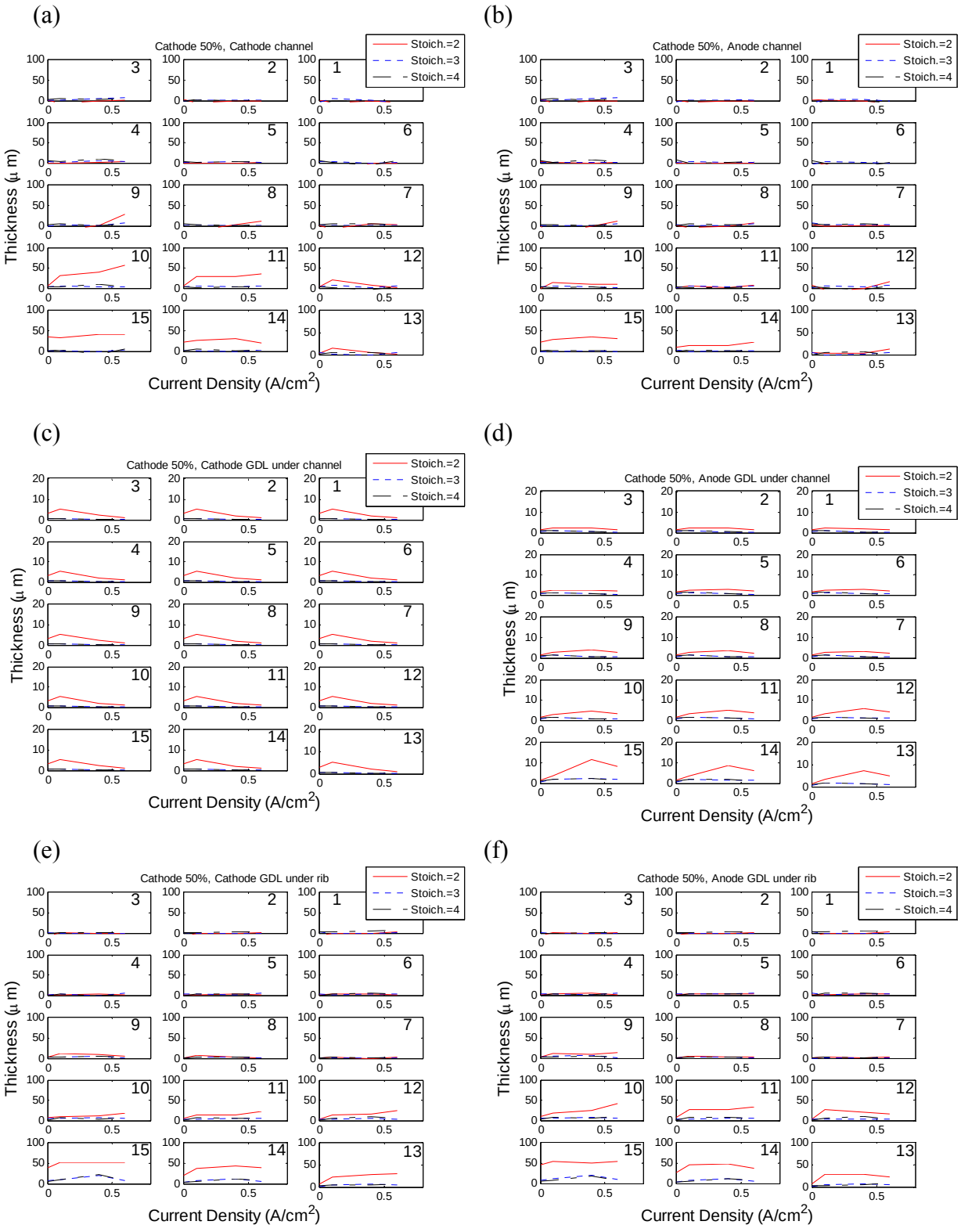

Figure 3-25: Liquid water accumulation at six locations of cell No. 2 at steady state condition (cathode inlet RH=50%).

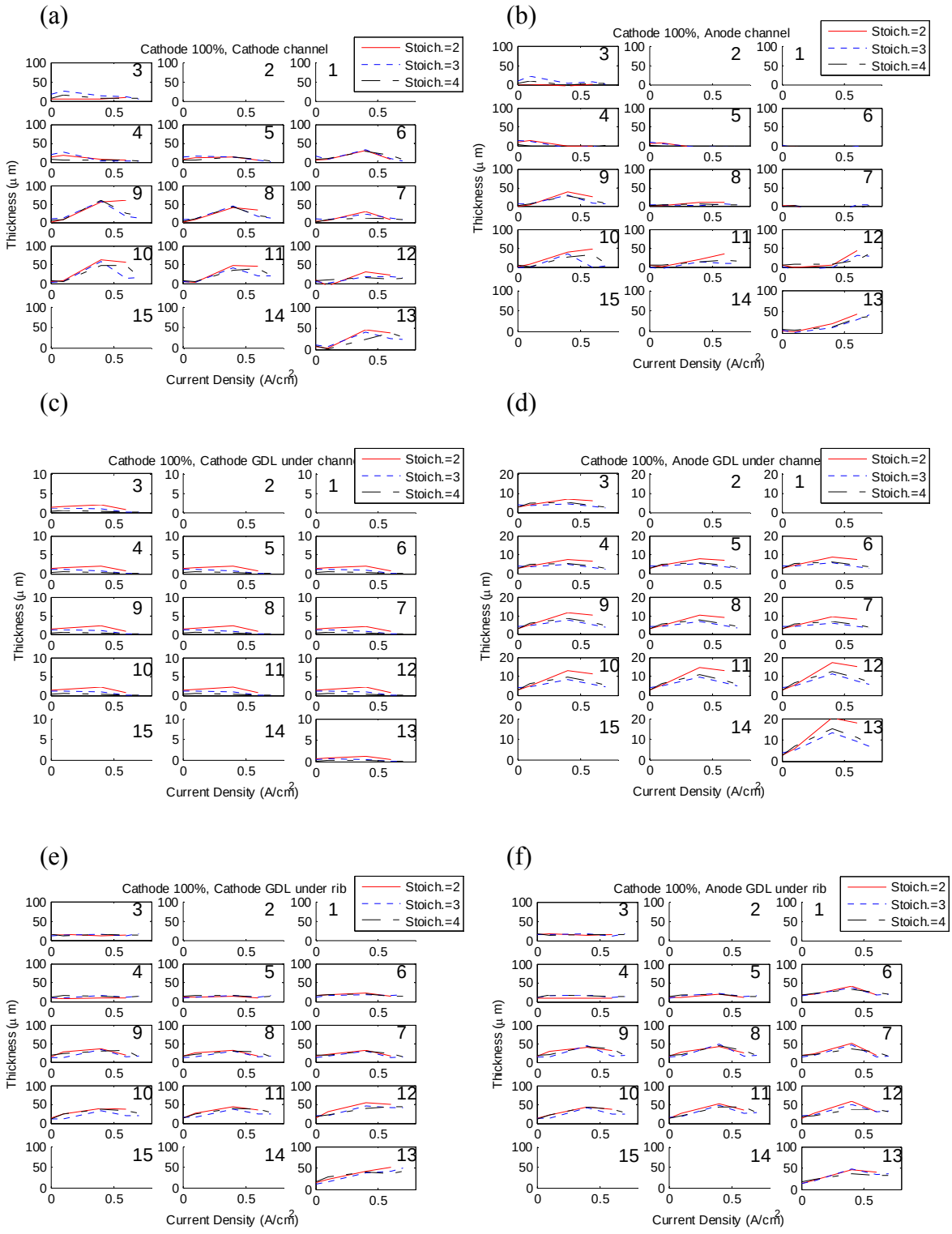

Figure 3-26: Liquid water accumulation at six locations of cell No. 3 at steady state condition (cathode inlet RH=100%).

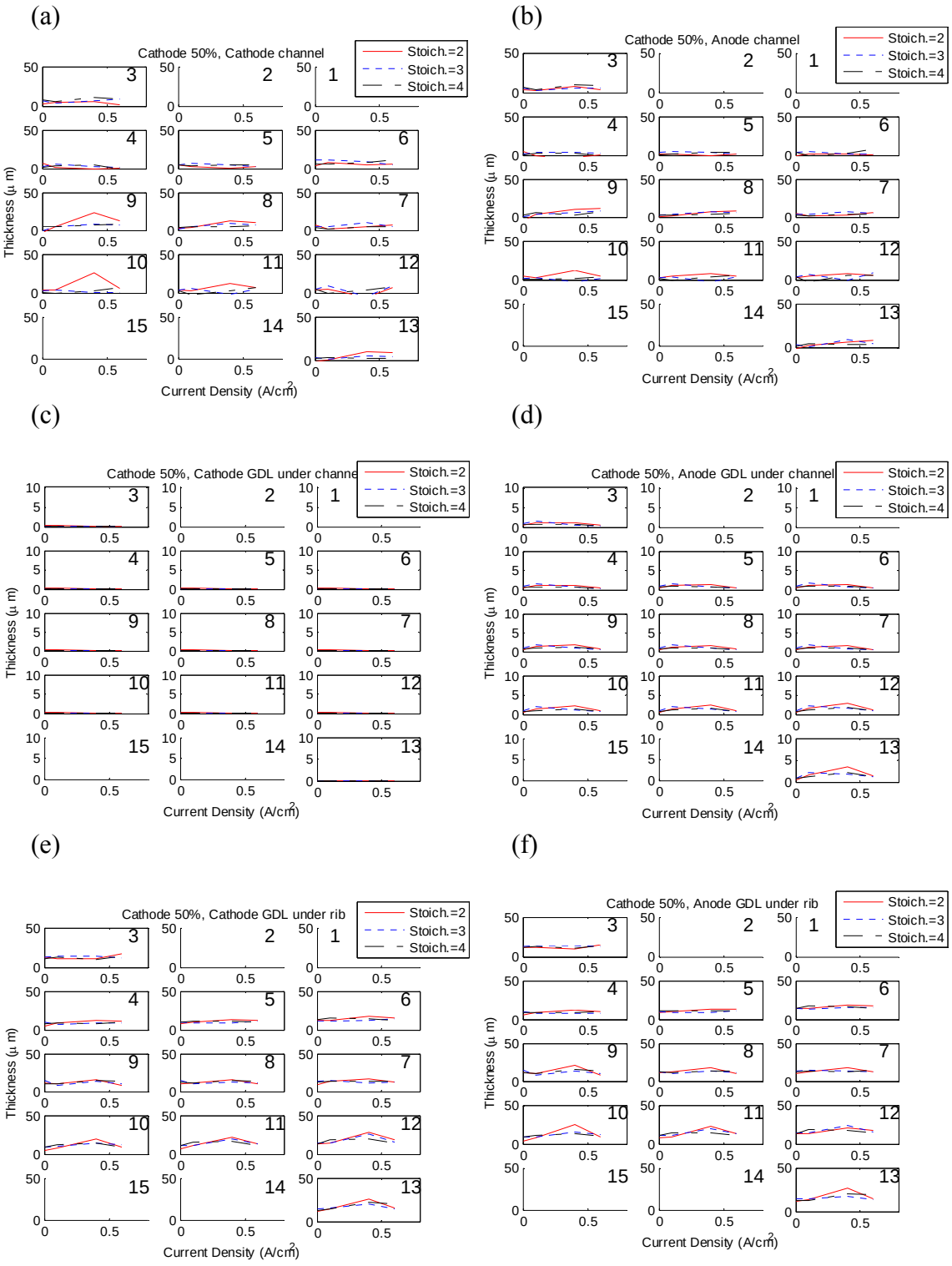

Figure 3-27: Liquid water accumulation at six locations of cell No. 3 at steady state condition (cathode inlet RH=50%).

From Figure 3-25 and Figure 3-27, it can be seen that when the cathode inlet RH is 50%, water content in the GDLs does not change with current densities. Because of the low RH of inlet cathode gas, the generated liquid water is quickly taken from GDLs by unsaturated gas flow. When the cathode inlet is fully humidified, more liquid water accumulates in the cathode GDL under the rib. Figures (e) and (f) in Figure 3-24 and Figure 3-26 show that maximum water thickness in the GDLs under the cathode rib and under the anode rib is around 50 μm, which could be the maximum amount of water that can accumulate in the GDLs under those operating conditions. Once water is generated in the cathode catalyst layer, it has the tendency to move from the hydrophobic GDL into the channels. If the GDL cannot expel liquid water effectively, liquid saturation in the GDL and catalyst layer will be large, which is commonly referred to as flooding.

Liquid saturation can be precisely quantified by the ratio of liquid volume to the pore volume in the GDL. This ratio directly relates to how much of the available volume for reactant flow has been occupied by liquid water, and thus reflects the extent of GDL "flow blockage". Pasaogullari et al. [13] and Natarajan et al. [14] developed different empirical models to study the distribution of liquid saturation along the thickness of GDLs. The liquid saturation in GDL is not easy to measure by using a mono-neutron beam—it will be possible, in theory, to obtain that information by using accurate stereo imaging. Unfortunately, such capability was not available when we conducted the experiment. Therefore, from the test data we can only calculate the average liquid saturation, which can be calculated by Equation (2.68).

The cathode of the PEMFC is the performance-constraint component due to the slower kinetics of oxygen reduction and the mass-transfer limitations caused by liquid water generation and the existence of large quantity of nitrogen. Thus, in the following only cathode liquid saturation is calculated and compared with other groups' studies. Figure 3-28 shows the result of using Equation (2.68) to calculate average liquid saturation in the cathode GDLs in cell No. 3. Figure 3-28 (a) shows that average liquid saturation in the GDL under the ribs varies from 0.05 to 0.5, whereas that in the GDL under the channels is below 0.02, as shown in Figure 3-28 (b). As shown in Figure 2-3 in Chapter 2, Pasaogullari's model describes the distribution of liquid saturation in the GDL under the channels only and the average value is close to 0.07. Natarajan's model shows

3-dimensional liquid saturation distribution in the GDLs both under the channels and under the ribs. The liquid saturation in the GDL under the ribs is higher than 0.9, whereas that in the GDL under the channel varies between 0 and 0.88. Pasaogullari's modeling result show better accuracy according to our experimental data.

(a) (b)

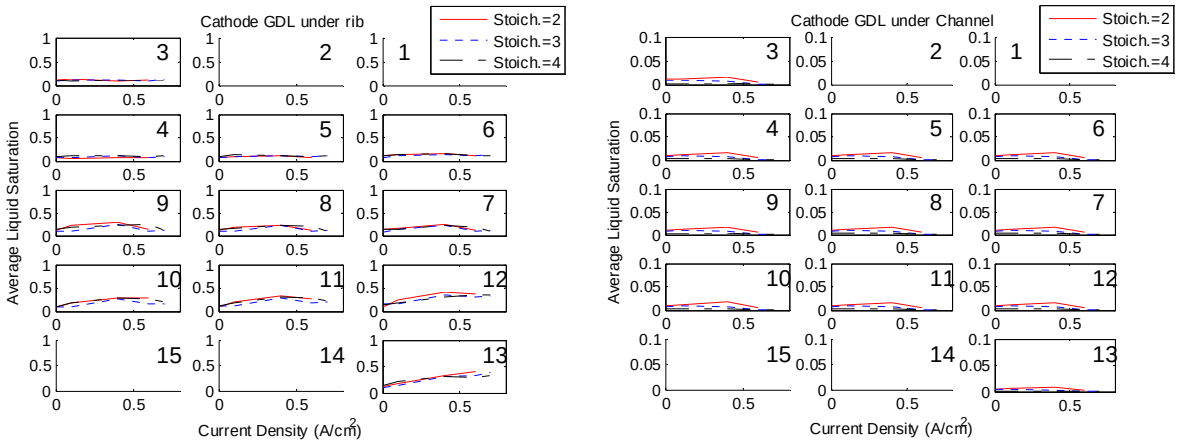

Figure 3-28: Average liquid saturation in (a) the GDL under rib; (b) the GDL under channel of cell No. 3.

Figure 3-29 (a) and Figure 3-29 (b) show relative humidity distribution in the cathode and anode when the cathode inlet RH is 50%. The RH in each segment increases with increasing current density. This is because water generation increases with increasing current density. However, at high current density (0.6 A cm^{-2}), RH values decrease slightly. It could be due to the high flow rate of unsaturated gas at high current density. Moreover, Figure 3-29 (a) shows that RH in the cathode channel at stoichiometry of 2 is slightly higher than those at stoichiometry of 3 and 4. These phenomena suggest small flow rate results in higher RH values in the channels. On the other hand, when cathode inlet RH is 100%, stoichiometry values do not influence RH in the channels, as shown in Figure 3-30 (a). Figure 3-29 (c), Figure 3-29 (d), Figure 3-30 (c), and Figure 3-30 (d) show segment temperatures increase slightly with current density but the temperature difference between segments can be neglected regardless of the stoichiometric values and cathode inlet RH.

The experimental results in this study suggest liquid water in the GDL under the ribs varies with current load and operating conditions, where as that in the GDL under the channels is not significantly influenced by operating conditions. In addition, this distributed data also provides us useful information to develop a fuel cell model.

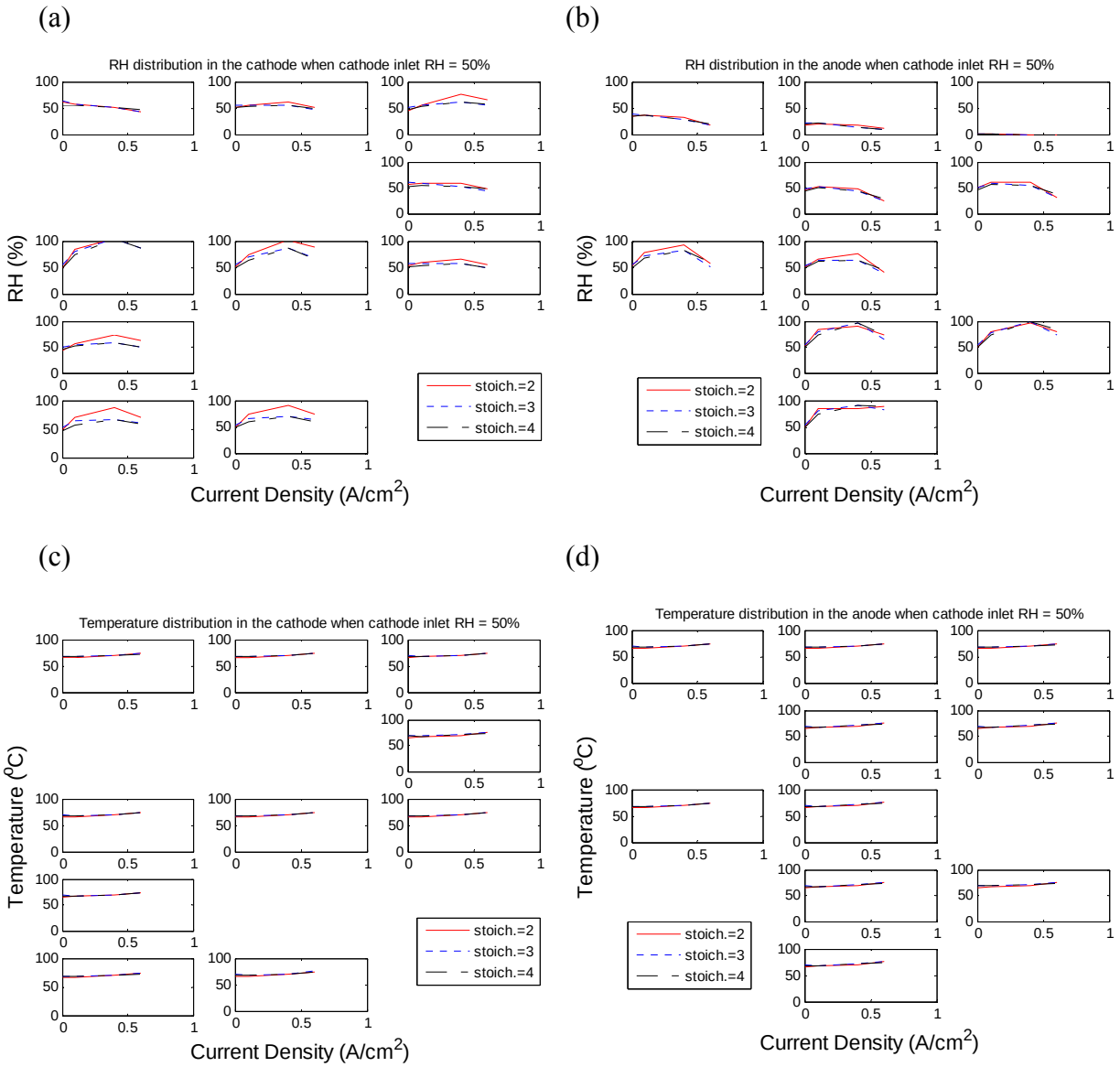

Figure 3-29: Relative humidity distribution in (a) cathode channel; (b) anode channel. Temperature distribution in (a) cathode channel; (b) anode channel when cathode inlet of cell No. 3 (cathode inlet RH= 50%).

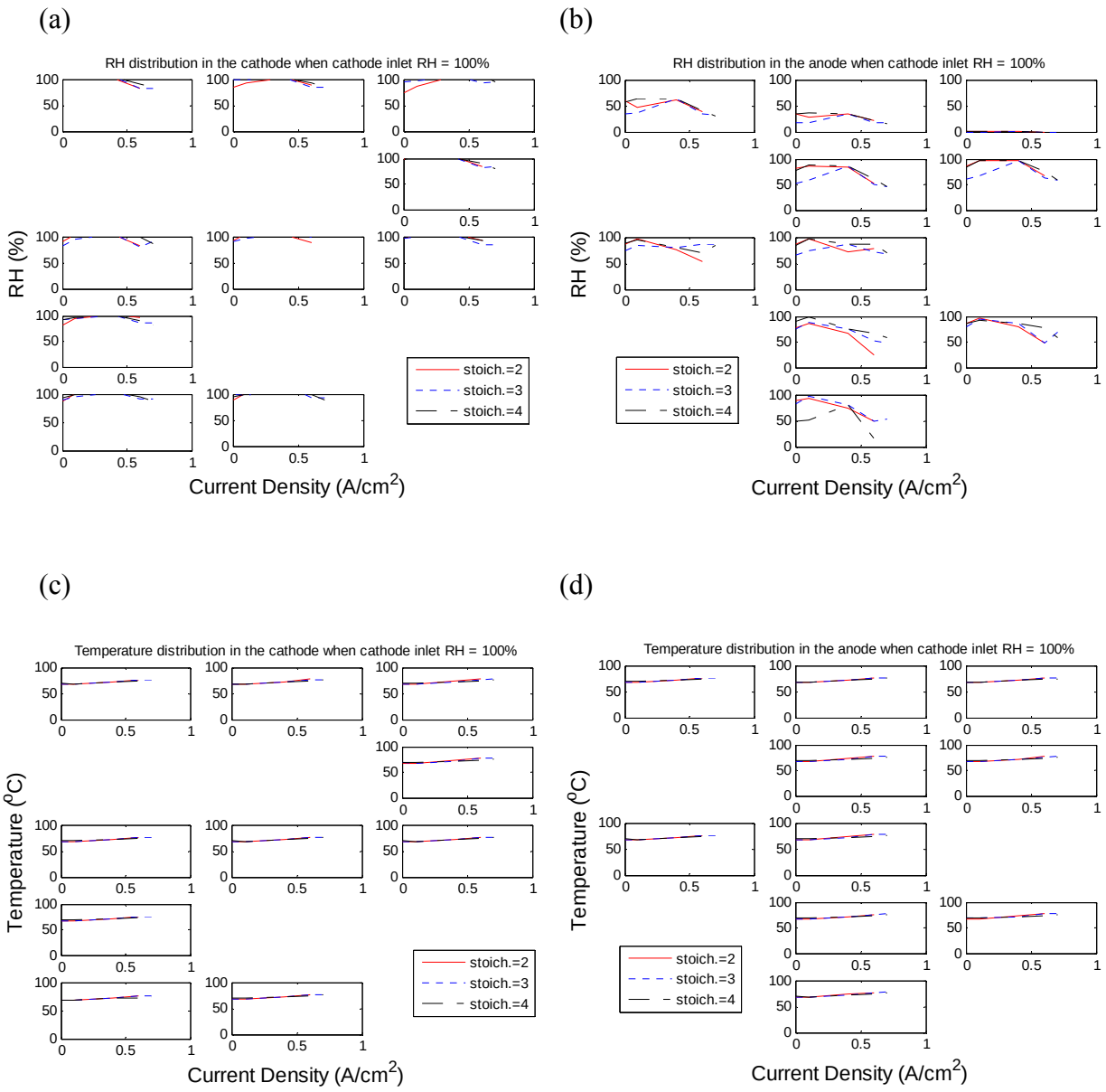

Figure 3-30: Relative humidity distribution in (a) cathode channel; (b) anode channel. Temperature distribution in (a) cathode channel; (b) anode channel when cathode inlet of cell No. 3 (cathode inlet RH= 100%).

3.5.6 Transient Behavior of Water Transport

The transient behavior of water transport was studied by plotting water thickness and measured RH values in the anode and cathode channels versus time. Due to limited time at the NIST, only cell No. 3 had simultaneously measured neutron imaging and RH sensor data. Cells No. 1 and No. 2 did not have data from RH sensor. In this section, only

transient behavior of water transport of cell No. 3 is discussed. The neutron images were recorded when the cell was operated at four different step current changes; from 0 A cm^{-2} to 0.1 A cm^{-2}, from 0.1 A cm^{-2} to 0.4 A cm^{-2}, from 0.4 A cm^{-2} to 0.7 A cm^{-2}, and from 0.7 A cm^{-2} to 0 A cm^{-2} as shown in Figure 3-31. The moment when a load change was applied was marked by vertical dashed lines in the figures, and the test data shown in Figure 3-32 includes 1 minute before the step change and 2 minutes after. Figure 3-32 shows that the water thickness changes with respect to time when the cathode inlet gas is 100%. These plots suggest that water contents in those six locations do not change immediately with load change. In other words, after current density is changed, it takes time for the water content in the fuel cell to reach steady-state.

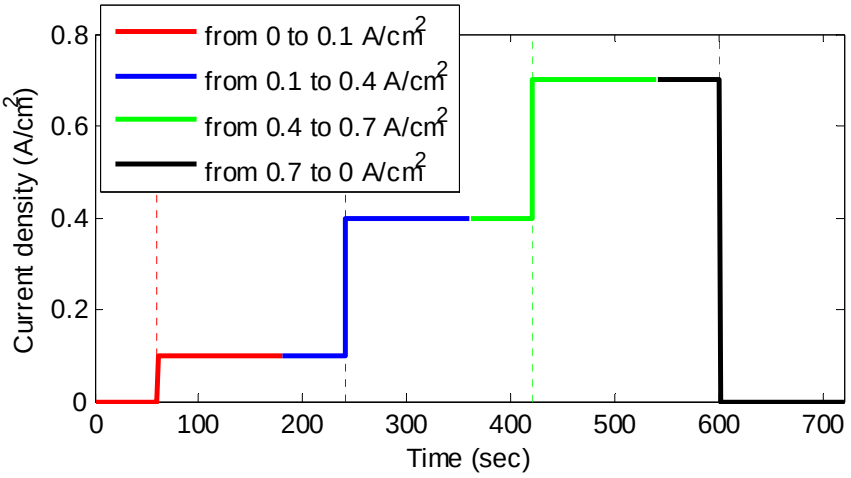

Figure 3-31: Step changes of current densities

Figure 3-32 (a) shows that liquid water in segment 13 gradually increases when current density changes from 0.4 to 0.7 A cm^{-2}, whereas liquid water in other segments decreases or keeps constant. It is possible that due to the channel-reduction design (from 12 channels to 6 channels) in the cathode, more liquid water is carried to the outlet, which encountered a bottleneck at segment 13. The liquid water in the GDL under the rib does not increase with time, as shown in segment 13 in Figure 3-32 (e). This result suggests that the channel-reduction design reduces flooding in the GDLs.

Figure 3-33 (a) and Figure 3-33 (b) show the RH values and temperature in the cathode and anode channels. When the cell is operated at low current densities, the RH in

the anode channel increases with the flow distance quickly and typically reaches saturation after one-third of the flow distance. However, when the current density changes from 0.4 to 0.7 A cm^{-2}, RH in the anode channel decreases to approximately 50% due to the electro-osmotic drag. Figure 3-32 (b) shows that there is some liquid water in the anode channel but RH sensors in Figure 3-33 (b) do not report 100%. The possible reason is that mass transfer rate due to liquid water evaporation is lower than that due to anode gas flow at high current density.

Figure 3-34 (a) and Figure 3-33 (b) show RH difference between cathode channel and anode channel when cathode inlet RH is 50%. When the current density is zero, i.e. no liquid water generated inside the fuel cell, RH in the anode channel increases along the channel to about 50%. When the current density increases to 0.1 A cm^{-2}, the RH values in the anode channel increase approximately to 75%, which is higher than that in the cathode channel. When the current density is 0.4 cm^{-2}, the RH values in the last segment of the anode channel reports 100%. Since the anode inlet gas is not humidified, the only way for anode gas to acquire water is through back diffusion from cathode to anode. Moreover, the cathode stoichiometry is higher than anode stoichiometry, i.e., cathode gas flow rate is higher than anode gas flow rate. Therefore, water in the anode channel is slowly removed, resulting in the increase of RH in the anode channels.

Figure 3-33 and Figure 3-34 also show the temperature distribution measured by RH sensors within the fuel cell. Since we only have 10 RH sensors for each of the anode/cathode side, some of the segments have no temperature data reported. Subplots are arranged corresponding to RH sensor positions. Regardless of the cathode inlet RH values, temperatures change slowly after sudden current changes. In addition, there is no significant temperature variation throughout the active area. There is little spatial variation of temperature at all current density levels. High thermal conductivity of graphite (140 W m^{-1} K^{-1}) and reactant flow both contribute to the uniform temperature. This result implies that temperature distribution can be considered to be uniform in a single cell, which helps to reduce the complexity of segmented single cell model in our future study.

The specially designed single cells together with image processing techniques and LSM provide a new way to investigate liquid water accumulation in an operating fuel

cell. These results show the influence of stoichiometry values and RH of cathode inlet on water distribution within a fuel cell. The experimental data is used to calibrate the mathematical model shown in Chapter 2. In developing a dynamic fuel cell model, the slow transient response of water transport in the GDL should not be neglected.

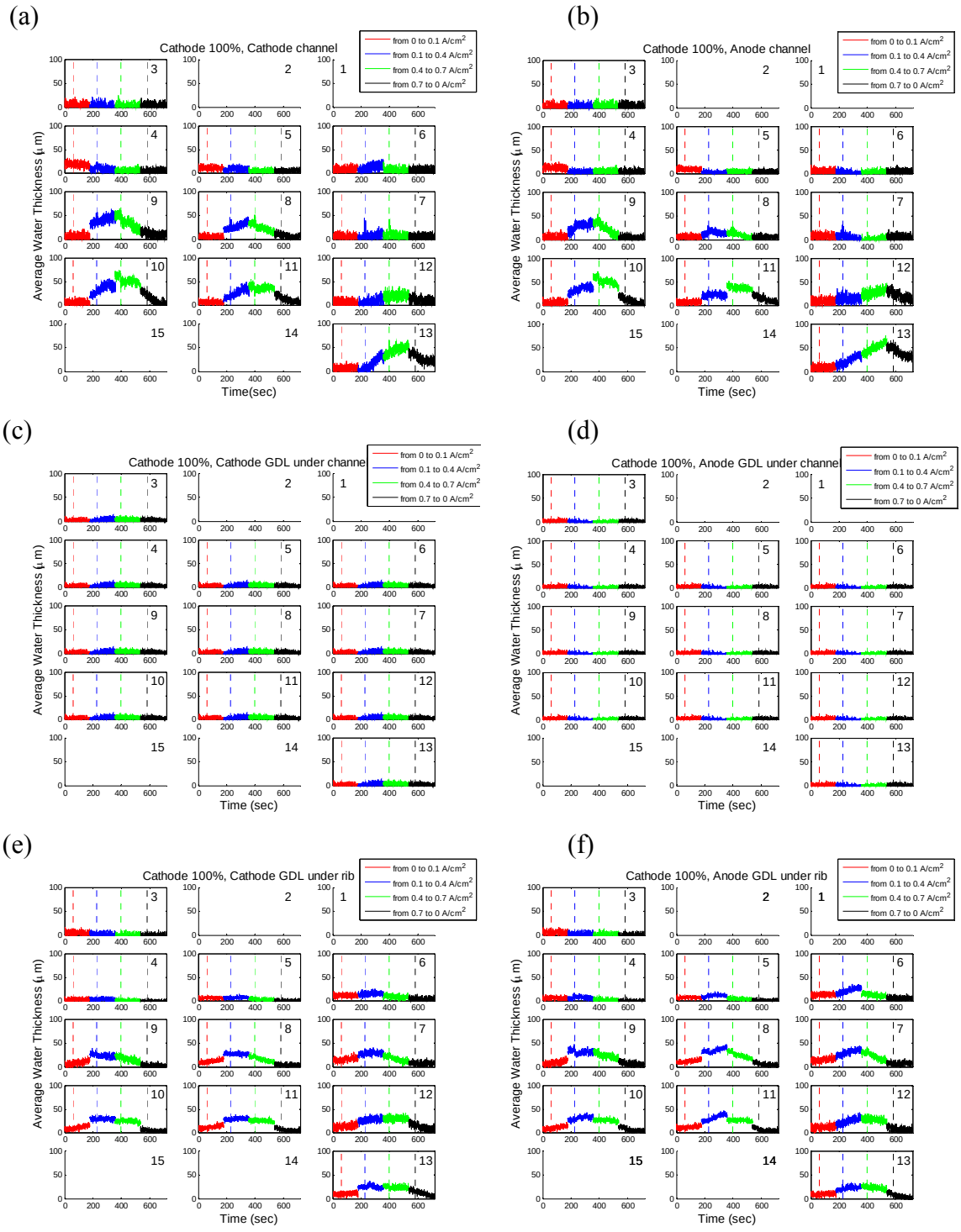

Figure 3-32: Step response of average liquid water thickness in (a) cathode channel; (b) anode channel; (c) cathode GDL under channel; (d) anode GDL under channel; (e) cathode GDL under rib; (f) anode GDL under rib when the cathode inlet RH is 100%.

(a) (b)

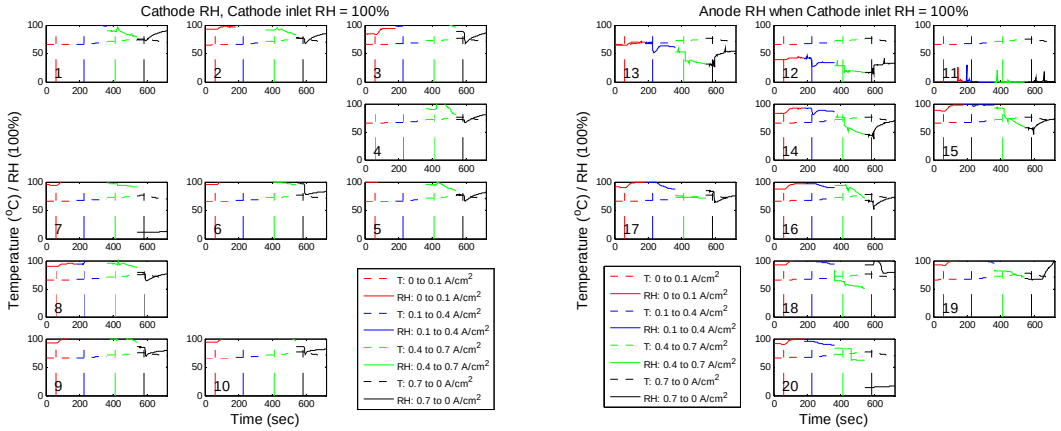

Figure 3-33: Step response of relative humidity in the (a) cathode channel; (b) anode channel when cathode inlet RH is 100%

(a) (b)

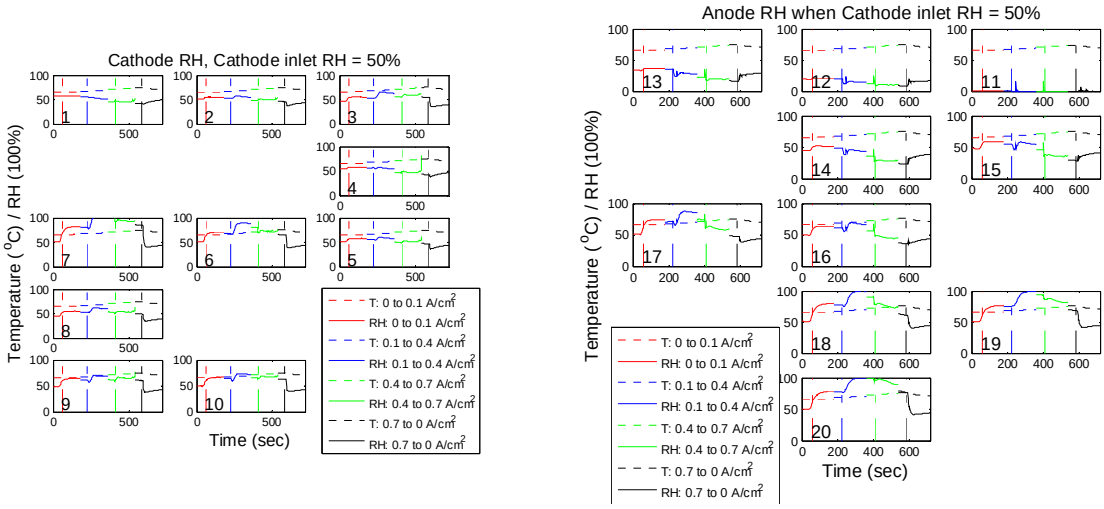

Figure 3-34: Step response of relative humidity in the (a) cathode channel; (b) anode channel when cathode inlet RH is 50%

CHAPTER 4
MODELING RESULTS AND DISSCUSSIONS

In this chapter we will discuss the steady-state modeling results. A two-dimensional steady-state fuel cell model was developed in Chapter 2. The model captures the distributions of current density, water content in the membrane, and RH in the flow channels. The segments of this model will be reconnected according to different flow field designs and modeling results will also be compared in this chapter.

4.1 Model Calibration

In Chapter 3, three single cells were designed for neutron radiography experiments. The experimental results were used to calibrate water related parameters in this model. There are many water related parameters in our fuel cell model. Due to the limitation in time and access to facility, we were only able to calibrate part of these parameters and obtained the other parameter values from the literature. The specification of fuel cell No. 1 and corresponding parameters are listed in Table 4.1. Those parameter values obtained from the literature are listed in Table 4.2. The parameters that are adjusted in this study are listed in Table 4.3.

The mathematical model discussed in Chapter 2 is calibrated based on the cell performance and water accumulation in the GDLs from experimental data. In the ohmic overpotential region of cell performance curve, membrane conductivity is mainly dependent on water content in the membrane, as shown in Eq. (2.88). Thus, b_{11}, b_{12}, and b_{13} in Eq. (2.88) and the contact resistance R_{contact} in Eq. (2.86) were tuned to match the calculated I-V curve with experimental data in the ohmic overpotential region. α and γ in Eq. (2.67) and β in Eq. (2.65) were adjusted to make modeling results of liqud

saturation in the GDLs match data from neutron radiography experiments. Once α, β, and γ were determined, liquid saturation can be determined. Subsequently, b_{21}, b_{22}, and i_{limit} in Eq. (2.91) are adjusted according to the concentration overpotential region of I-V curve.

Table 4.1: Parameters of the single cell No. 1.

Parameter	Value
Cell active area (A_{cell})	100 cm^2
Channel depth (H_{ch})	1 mm
Channel width (W_{ch})	1.6 mm
Rib width (W_{rib})	1.7 mm
Anode channel number in a segment (Z_{an})	6
Cathode channel number in a segment (Z_{ca})	10
Anode channel length in a segment (L_{an})	3.33 cm
Cathode channel length in a segment (L_{ca})	2 cm
GDL thickness (t_{gdl})	184 μm
GDL porosity (ε)	0.725
Dry membrane thickness (t_{pem})	25 μm
Dry membrane density (ρ_{pem})	2000 kg m^{-3}
Dry membrane equivalent weight (M_{pem})	1.1 kg mol^{-1}

Table 4.2: Parameter values that were obtained from literature

Parameter	Value
Absolute Permeability of GDL (K)	1×10^{-8} m^{-2} [13]
Relative permeability of GDL (K_{rw})	S [14]
Dynamic viscosity of hydrogen (μ_{H_2})	9.5493×10^{-6} N s m^{-2} [53]
Dynamic viscosity of oxygen (μ_{O_2})	2.2379×10^{-5} N s m^{-2} [53]
Dynamic viscosity of nitrogen (μ_{N_2})	1.9260×10^{-5} N s m^{-2} [53]
Dynamic viscosity of water vapor (μ_v)	4.6657×10^{-4} N s m^{-2} [53]
Pressure-diffusivity product of water vapor and hydrogen pair ($PD_{H_2\text{-}v}$)	16.6801 Pa m^2 s^{-1} [54]
Pressure-diffusivity product of water vapor and oxygen pair ($PD_{O_2\text{-}v}$)	3.2890 Pa m^2 s^{-1} [54]
Pressure-diffusivity product of water vapor and nitrogen pair ($PD_{v\text{-}N_2}$)	3.4400 Pa m^2 s^{-1} [54]
Pressure-diffusivity product of oxygen and nitrogen pair ($PD_{O_2\text{-}N_2}$)	2.5504 Pa m^2 s^{-1} [54]
Diffusivity of water vapor in hydrogen ($D_{v\text{-}H_2}$)	9.3940×10^{-3} m^2 s^{-1} [54]
Diffusivity of water vapor in air ($D_{v\text{-air}}$)	2.6560×10^{-3} m^2 s^{-1} [54]

Table 4.3: Parameters that were tuned based on experimental data

Parameter	Equation number	Tuned value
$R_{contact}$	(2.86)	0.047 (Ohm)
α	(2.67)	-0.012
β	(2.65)	1×10^{-9}
γ	(2.67)	2
b_{11}	(2.88)	0.195
b_{12}	(2.88)	0.326
b_{13}	(2.88)	350
b_{21}	(2.91)	-0.75
b_{22}	(2.91)	7
i_{limit}	(2.91)	1.2 (A cm^{-2})

4.2 Modeling Results of Cell No. 1

In practical applications, due to space and cost considerations, it is common to humidify only the cathode reactant. Thus, we will focus on the influence of relative humidity of cathode inlet on cell performance and water transport. Figure 4-1 compares the cell performance of cell No. 1 obtained by this model and by experiments. The cell operating at low cathode inlet RH of 50% shows lower cell performance. This is because the under-saturated air takes water from the membrane, resulting in low membrane hydration and conductivity.

In this study, each segment is regarded as a lumped model. Thus, at the end of the iteration procedure, only lumped values were obtained. For visual aids, color pictures are created through interpolation and extrapolation of these values, which are marked at the center of each segment.

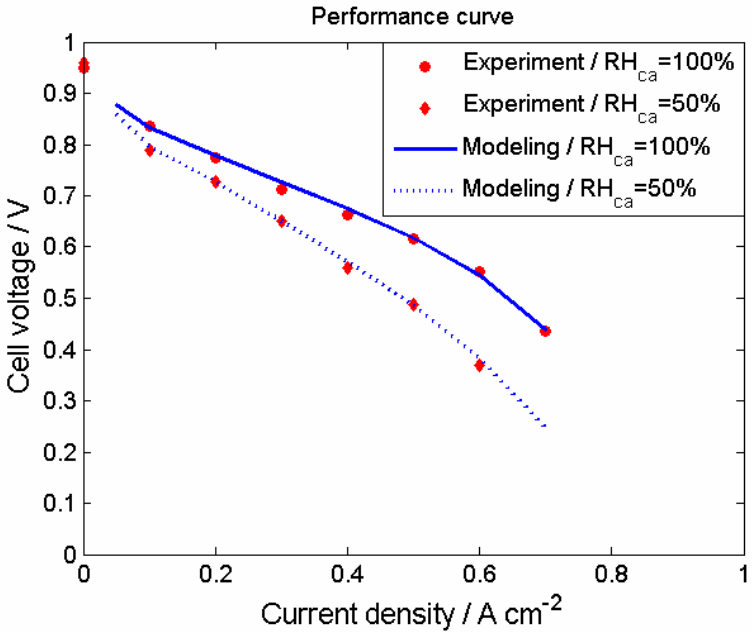

Figure 4-1: Comparison of experimental results and modeling results for different cathode inlet RH (cell No. 1).

4.2.1 Distribution of Current Density and Water Content in the Membrane

Membrane dehydration increases ohmic overpotential, and could even cause irreversible damage to the membrane. Since the membrane conductivity dominates (Conductivity of membrane: ~2.75 Ω^{-1} m^{-1}; GDL: ~1250 Ω^{-1} m^{-1}; graphite plate: ~1×10^{5}

Ω^{-1} m^{-1}), current density distribution is highly dependent on the water content in the membrane, which in turns significantly influences the cell performance and reliability.

Figure 4-2 (a), Figure 4-2 (b), Figure 4-3 (a), and Figure 4-3 (b) show current density distribution of four selected operating conditions listed in Table 4.4. All figures suggest that the maximum current density is located near the anode outlet, the region with maximum water content. By comparing Figure 4-2 (a) and Figure 4-2 (b) (high current density cases), we observe that at fully humidified cathode condition, the maximum local current is approximately 1.4 times the minimum local current. This ratio increases to 2 at low cathode humidity condition. In Figure 4-3 (a) and Figure 4-3 (b), for low current density cases, the maximum local current is 1.5 and 1.6 times the minimum, respectively. The result suggests that at low current density, cathode inlet relative humidity has less influence on current density distribution. Low cathode humidity causes low water content, as shown in Figure 4-3(d).

Table 4.4: List of selected operating conditions

	Case1	Case 2	Case 3	Case 4
Anode/Cathode inlet RH (%)	0/100	0/50	0/100	0/50
Anode/Cathode stoichiometry value	1.2/3.0	1.2/3.0	1.2/3.0	1.2/3.0
Anode/Cathode outlet pressure (atm)	1/1	1/1	1/1	1/1
Cell current density (A cm^{-2})	0.7	0.6	0.1	0.1
Cell temperature (˚C)	70	70	70	70

Measurement of current density distribution of a working fuel cell can be achieved by using divided current collectors [74, 77-81]. Yoshioka et al. [77] compared the distribution of current densities at different inlet gas RH levels. Their results show that the region close to air inlet has lower current density. The trend is more significant with dry inlet air. Liu et al. [74] measured current density distribution of a fuel cell with one serpentine flow channel. Their findings are the same as [77] qualitatively, except that with fully humidified air, current density of the area near outlet is lower due to flooding. In the study of Mench et al. [81], both anode and cathode gases were fully humidified before fed into the fuel cell and thus the influence of relative humidity was not discussed

in their study. Their study mainly focused on the influence of cathode stoichiometry value on current density distribution. Experimental results showed that high stoichiometry values results in uniformly distributed current density. At Low stoichiometry conditions, current density at the downstream area is obviously lower than that at the upstream area.

In our study, the effect of flooding on reducing current density near the outlet is not obvious. A possible reason is that anode reactant is not humidified so the excess water transports to the anode. Another reason is that we use straight parallel cathode channels so liquid water is quickly removed from channels.

	Case 1	Case 2
Current density distribution (%)	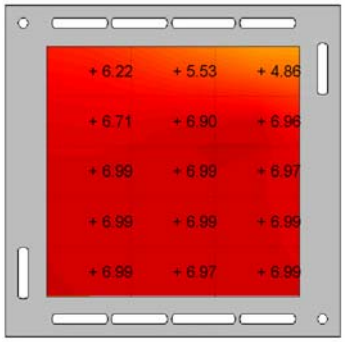 (a)	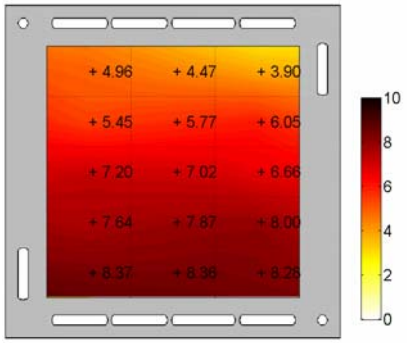 (b)
Water content	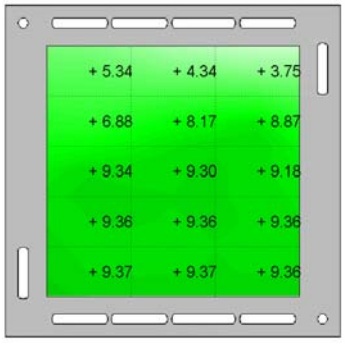 (c)	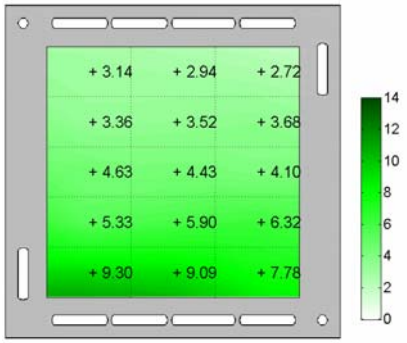 (d)
Anode RH (%)	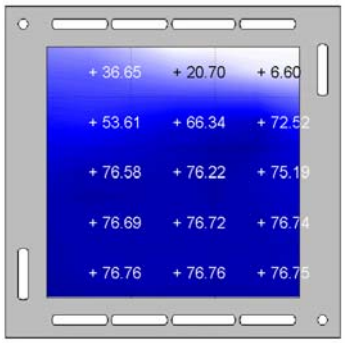 (e)	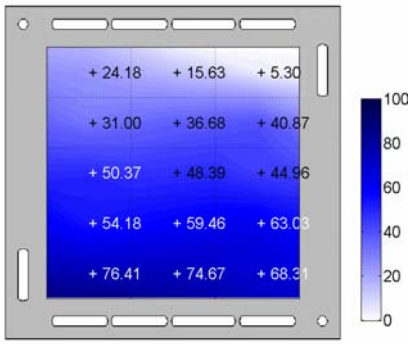 (f)
Cathode RH (%)	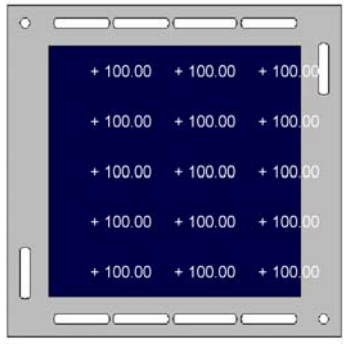 (g)	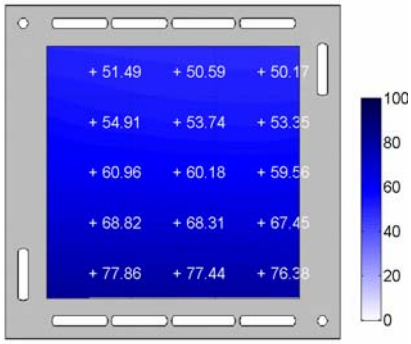 (h)

Figure 4-2: Distribution of current density, water content in the membrane, relative humidity in the anode channel, and relative humidity in the cathode channel. Left figures: case 1. Right figures: case 2. (Cell No. 1)

	Case 3	Case 4
Current density distribution (%)	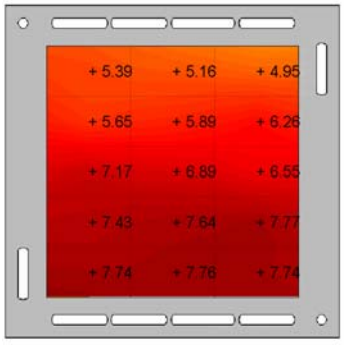 (a)	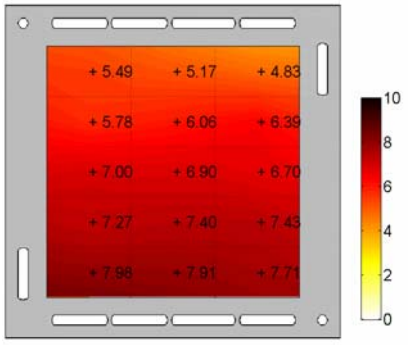 (b)
Water content	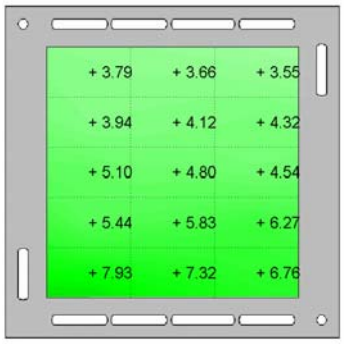 (c)	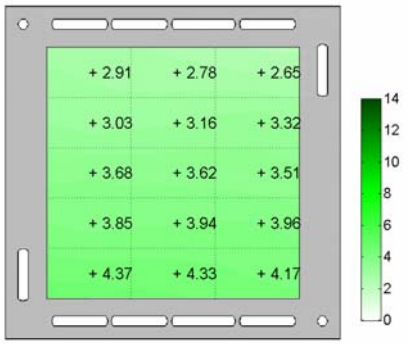 (d)
Anode RH (%)	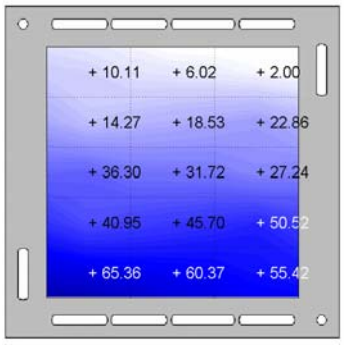 (e)	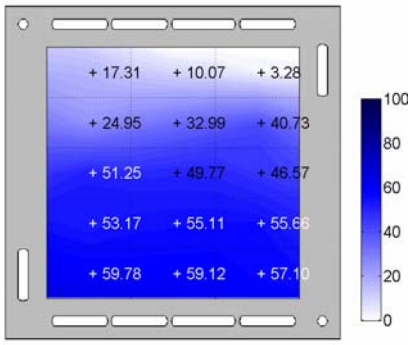 (f)
Cathode RH (%)	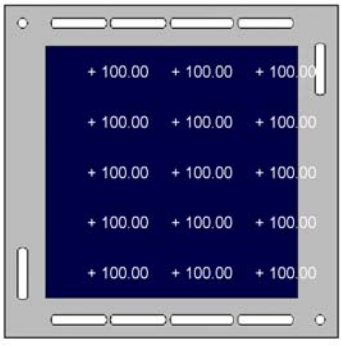 (g)	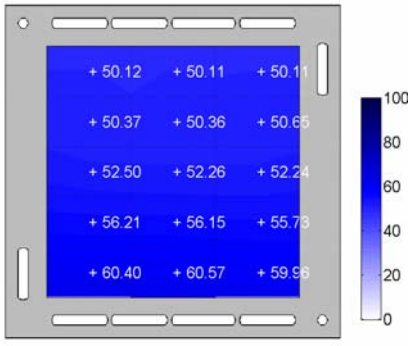 (h)

Figure 4-3: Distribution of current density, water content in the membrane, relative humidity in the anode channel, and relative humidity in the cathode channel. Left figures: case 3. Right figures: case 4. (Cell No. 1)

4.2.2 Distribution of RH in the Flow Channel and Water Transport in the MEA

Figure 4-2 (e), Figure 4-2 (f), Figure 4-3 (e), and Figure 4-3 (f) show RH distribution in the anode flow channel. For all cases, RH increases along the flow direction because dry hydrogen gradually uptakes water vapor that comes from the cathode by back diffusion. Figure 4-4 compares water transport through the membrane and through both anode and cathode GDLs. The magnitude indicates the quantity of water transport and positive direction represents from the anode to the cathode. At high current density, water transport from the anode channel to the membrane through the anode GDL was observed in the downstream segments, as shown in Figure 4-4 (a) and Figure 4-4 (b). The high current density in those segments results in high electro-osmotic drag from the anode to the cathode, which is stronger than the back diffusion from the cathode to the anode; hence, water in the anode reactant supplies for the difference. However, as shown in Figure 4-2 (a), the anode RH does not decrease along flow channel. Because of hydrogen consumption along flow channel, the molar fraction of water vapor increases along flow channel. That also explains why RH in the anode downstream segments barely increased.

Figure 4-4 (c) and Figure 4-4 (d) show that the electro-osmotic drag of the segments near outlet in case 3 is significantly higher than that in case 4, although current densities of both cases are very similar, as shown in Figure 4-3 (a) and Figure 4-3 (b). According to Eq. (2.70), the electro-osmotic drag coefficient is a function of water content. Thus, high water content in the membrane is attributed to humidified cathode reactant.

Figure 4-2 (g) and Figure 4-3 (g) show fully saturated reactant in the cathode channel throughout the active area. Since cathode inlet reactant is fully humidified, the generated water transports to the channel in liquid form. In the cases of under-saturated cathode inlet reactant, the cathode RH gradually increases along the gas flow direction, as shown in Figure 4-2 (h) and Figure 4-3 (h). The increase is due to water generation and also oxygen consumption along the flow channel, resulting in increased molar fraction of water vapor. Water transport through GDLs influences diffusivities of reactant and could also form liquid water in the GDLs.

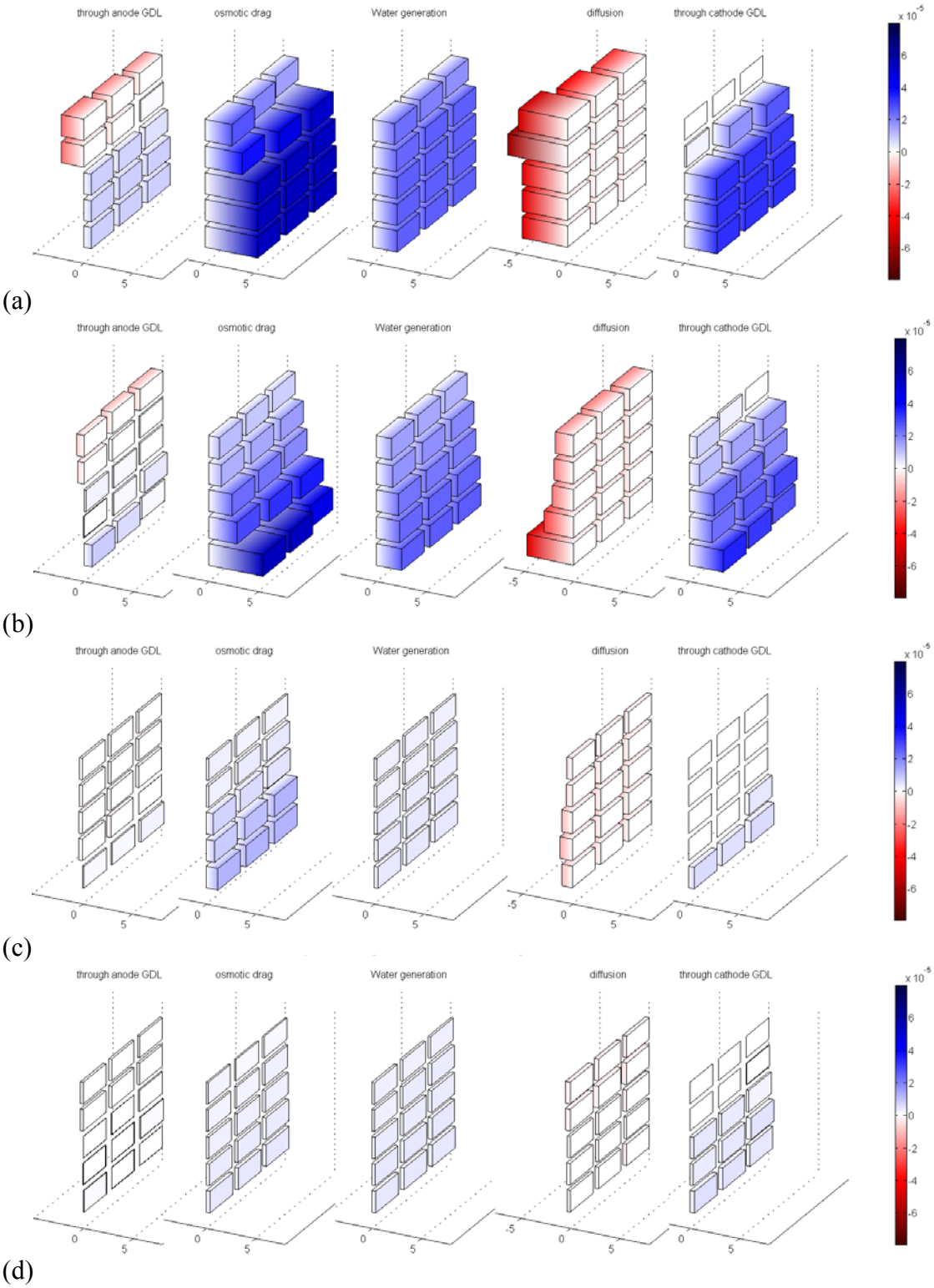

Figure 4-4: Quantity of water transport (mol s^{-1}) across the MEA (Cell No. 1). (a) case 1; (b) case 2; (c) case 3; (d) case 4.

4.2.3 Distribution of Water Accumulation

Cathode liquid saturation in the GDL affects cell performance because liquid water may cover the reaction sites in the catalyst layer or block the pathway of gas flow through the GDL. The liquid saturation in the cathode GDL is affected by many factors: cell temperature, permeability and hydrophobicity of the GDL, net water flux through the GDL, and cathode flow RH. In this model, temperature, permeability and hydrophobicity of the GDL are assumed to be constant. Under saturated condition, net water flux through the GDL is determined by working current density. Higher current density results in higher electro-osmotic drag and water generation, which causes higher net water flux through the GDL, as shown in Figure 4-4 (a) and Figure 4-4 (b).

Figure 4-5 compares average liquid saturation in the cathode GDL of modeling results and experimental data. The fifteen subplots correspond to fifteen segments of the active area. Figure 4-5 (a) and Figure 4-5 (c) suggest that liquid water accumulate in the GDL under the rib. Results from other neutron radiography experiments also show this phenomenon [82, 83]. Slight liquid saturation in the GDL under the rib is observed at the segment near cathode inlet and increases toward the outlet. Maximum liquid saturation is approximately 0.4. The low water accumulation in the cathode GDL at high current density is likely due to the high gas flow rate at high current density. Figure 4-5 (c) shows some liquid saturation in the GDL under the rib when cathode inlet RH is 50%. However, there is almost no liquid water in the GDL under the channel, as shown in Figure 4-5 (d). This is because the gas flow in the flow channel is under-saturated.

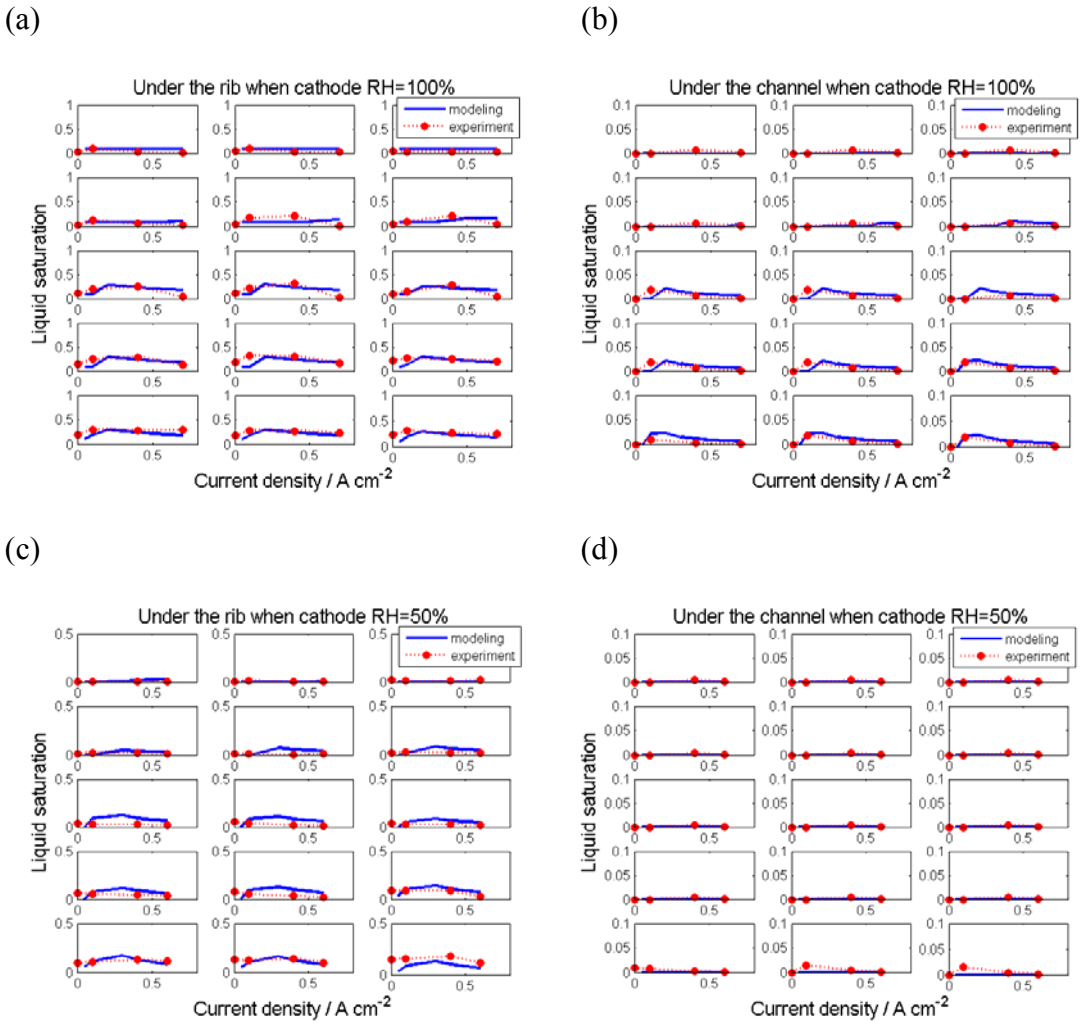

Figure 4-5: Comparison of modeling results and experimental data. (Cell No. 1) (a) Distribution of liquid saturation in the GDL under the rib when cathode inlet RH=100%; (b) Distribution of liquid saturation in the GDL under the channel when cathode inlet RH=100%; (c) Distribution of liquid saturation in the GDL under the rib when cathode inlet RH=50%; (d) Distribution of liquid saturation in the GDL under the channel when cathode inlet RH=50%.

4.3 Modeling Counter-Flow and Co-Flow Designs

In this study, three single cells were designed and used for experiments to study the influence of flow field pattern on cell performance and water accumulation within these cells. The model calibration was based on the experimental data of cell No. 1. We will keep the calibrated parameters and connect the segments according to the flow field

patterns of cells No. 2 and No. 3, respectively. The experimental results of cells No. 2 and No. 3 will be used to validate the modeling results.

In the flow pattern designs for cells No. 2 and No. 3, counter-flow exists in part of the active area, as shown in Figure 4-6. Figure 4-7 shows segments numbered successively according to the anode flow pattern. If we follow the solving procedure shown in Figure 2-6, it will be a challenge in solving the counter-flow segments. In this study, segment current and all the properties of the anode and cathode reactants are required for individual segment to solve the segment voltage. If we solve each segment successively according to anode flow direction, then there is no problem to get $N_{an,H_2,in}$ and $N_{an,w,in}$ for each segment. However, when we start to solve segment 4, we don't have $N_{ca,O_2,in}$, $N_{ca,N_2,in}$, and $N_{ca,w,in}$ since they are outputs of segment 5, which has not been solved yet.

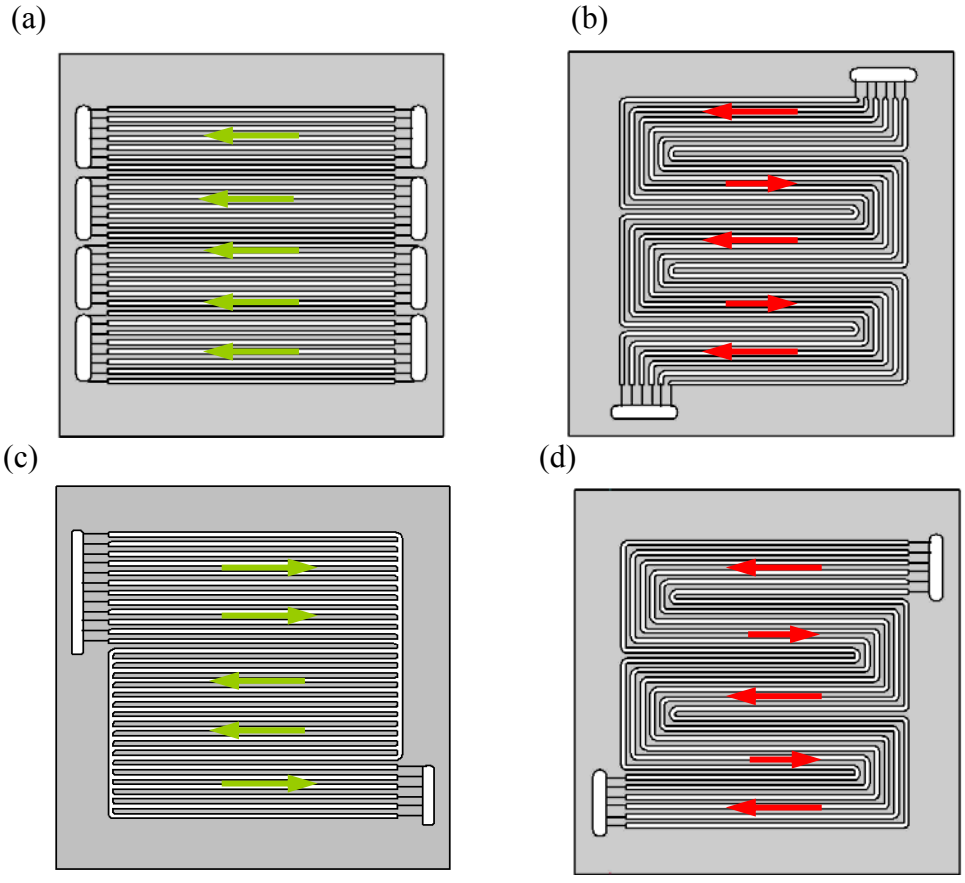

Figure 4-6: Schematic of counter-flow in cell No. 2. (a) cathode of cell No. 2; (b) anode of cell No. 2; (c) cathode of cell No. 3; (b) anode of cell No. 3.

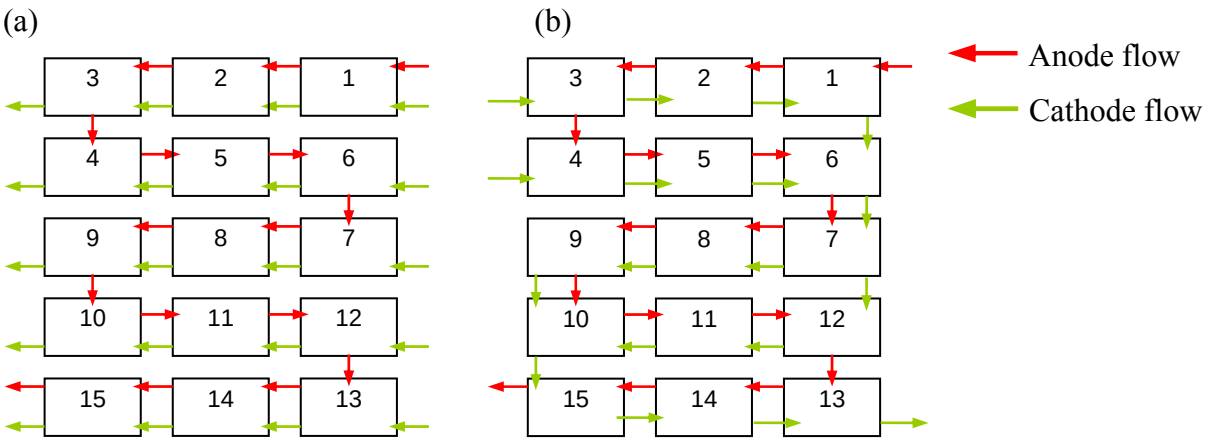

Figure 4-7: Segment connection of cell No. 2 (a) and cell No. 3 (b).

In the literature, a few researchers have modeled the count-flow configuration of PEMFCs [84-87]. Ge et al. [84] developed a two dimensional fuel cell model to investigate the co-flow and counter-flow modes of fuel cell at different operating conditions. When they dealt with the counter-flow mode, they guessed a water flow rate at the cathode inlet and the calculated water flow rate at the cathode outlet was compared with actual value. If these two values do not match, they will guess a new values and solve the model again. Birgersson et al. [85] developed an isothermal three-dimensional model to compare the performance of four different flow field patterns: co-flow, counter-flow, interdigitated, and foam. The details of solving counter-flow mode were not given in their study. However, their model took one to twelve hours to solve the counter-flow model problem. Their results suggested that under the same operating conditions, interdigitated and foam flow fields showed higher performance than co-flow and counter-flow did, but there was no significant performance difference between the co-flow and counter-flow. Hwang et al. [86] developed a non-isothermal model to investigate a interdigitated flow field pattern. They studied the conditions where the cathode reactants flowed into the GDL with the same (co-flow) and opposite (counter-flow) directions to the anode reactants. They used commercial software to solve their model and the details were not provided in their paper. Their model also takes hours to solve for each operating condition.

Berger et al. [87] developed a simplified model to study the distributions of current density and relative humidity along a straight channel. They discussed the

influence of co-flow and counter-flow modes on the distributions of current density and relative humidity. In their model, they discretized the flow channel into 1048 points. When they solved the counter-flow mode, all the initial values of the anode and cathode fluxes at these points were set as the inlet values. The cathode fluxes were then updated by using the anode fluxes from the previous iteration. The anode fluxes were then updated by using local current and water transfer calculated from previously computed cathode channel values. The updating process is continued until the anode and the cathode flux values converge. The details can be found in Berger's study [87]. Berger et al. provided a useful method for solving the counter-flow problem in a straight channel design. In our study, the flow field patterns are more complicated than straight channels. There are not only counter-flow modes but also co-flow modes in our designs of cells No. 2 and No. 3. We employed and modified Berger's updating procedure to solve our flow field patterns.

As mentioned at the beginning of this section, $N_{\mathrm{ca,O_2,in}}$, $N_{\mathrm{ca,N_2,in}}$, and $N_{\mathrm{ca,w,in}}$ for segment 4 are unknown when we start to solve segment 4 during each iteration. However, we can calculate $N_{\mathrm{ca,O_2,in}}$ and $N_{\mathrm{ca,N_2,in}}$ before segment 5 and segment 6 are solved. Flow rates of reacted oxygen in segments 5 and 6 can be determined by the assigned segment currents in the beginning of each iteration.

$$N_{\mathrm{ca,O_2,in}}\Big|_{seg,4} = N_{\mathrm{ca,O_2,in}}\Big|_{seg,6} - \frac{I_{seg,5}}{4F} - \frac{I_{seg,6}}{4F} \tag{4.1}$$

Besides, nitrogen does not react in each segment, so nitrogen flow rate in segment 4 is equal to that at the inlet of segment 6.

$$N_{\mathrm{ca,N_2,in}}\Big|_{seg,4} = N_{\mathrm{ca,N_2,in}}\Big|_{seg,6} \tag{4.2}$$

From the above, the only unknown is $N_{\mathrm{ca,w,in}}$ when will start to solve segment 4. In the flow field design of cell No. 2, same situation happens to segments 5, 10, and 11.

Similar to Berger's procedure, in the beginning of our solution process, the $N_{\mathrm{ca,w,in}}$ values of segments 4, 5, 10, and 11 are initially set as the inlet values of segments 6 or 12 according to the flow field pattern. Then $N_{\mathrm{ca,w,in}}$ values of the above four segments are updated by using the output values of their preceding segments, i.e., segments 5, 6, 11, 12, respectively.

$$N_{\text{ca,w,in}}\Big|_{\text{seg,4}}^{n+1} = N_{\text{ca,w,out}}\Big|_{\text{seg,5}}^{n} \tag{4.3}$$

$$N_{\text{ca,w,in}}\Big|_{\text{seg,5}}^{n+1} = N_{\text{ca,w,out}}\Big|_{\text{seg,6}}^{n} \tag{4.4}$$

$$N_{\text{ca,w,in}}\Big|_{\text{seg,10}}^{n+1} = N_{\text{ca,w,out}}\Big|_{\text{seg,11}}^{n} \tag{4.5}$$

$$N_{\text{ca,w,in}}\Big|_{\text{seg,11}}^{n+1} = N_{\text{ca,w,out}}\Big|_{\text{seg,12}}^{n} \tag{4.6}$$

The superscript n in these equations indicates the *n*-th step in time.

The updating procedure continues until solutions converge. The same solution procedure is applied to cell No. 3 for the segments with counter-flow mode.

4.4 Comparison of Cell Performance

Figure 4-8 shows the cell performance curves of cells No. 2 and No.3. Compared with cell No. 1, the cell voltages of cells No. 2 and No. 3 operated at the cathode inlet RH of 50% are only a little lower that those at 100%, as shown in Figure 4-8 (a) and Figure 4-8 (b). The experimental results suggest that cathode inlet RH has more significant influence on cell performance in cell No. 1.

Figure 4-1 shows that simulation results agree well with the experimental results for cell No. 1. In Figure 4-8 the slight deviation between modeling results and experimental results for cells No. 2 and No. 3 could be due to the different cathode flow field designs. The other possible reason is that the MEAs used for the 3 single cells are not exactly the same. For example, the difference of Pt catalyst loading between MEAs could result in different cell performance. In addition, different flow field designs could also cause different contact resistances. These problems can be solved by tuning some parameters in the cell voltage model.

All three cells operated at low cathode inlet RH of 50% show lower cell performance. This is because of the low water content in the cathode gas flow, gas flow takes water from membrane, resulting in low membrane hydration and conductivity.

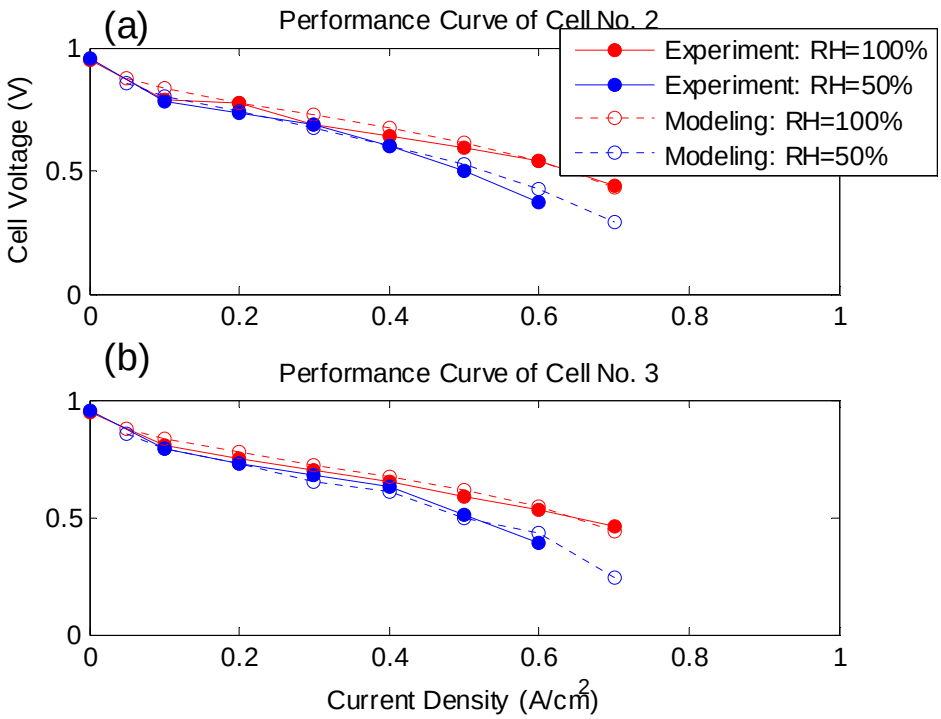

Figure 4-8: Comparison of experimental results and modeling results for different cathode inlet RH.

Figure 4-9 shows current density distribution, water content in the membrane, RH in the anode channels and in the cathode channels of cell No. 2 when the cathode inlet RH is 100% and 50%, respectively. When cathode inlet RH is 100%, current density distribution is more even than that when the cathode inlet RH is 50%. When cathode inlet RH is 50%, the current density near cathode inlet is lower and increases with cathode gas flow distance, as shown in Figure 4-9 (b). The result also suggests that cathode inlet RH significantly influences current density distribution. From the above results, high RH of cathode inlet gas helps current density distribute more evenly. Liu et al. [74] measured the current density distribution of a working fuel cell; their study also showed similar results.

The current density distribution of cell No. 3 suggests similar trend as that of cell No. 2, i.e., the current density near the anode inlet is the lowest and gradually increases toward the outlet, as shown in Figure 4-10 (a) and Figure 4-10 (b). According to Equations (2.71) and (2.72) in the membrane hydration model, water content in the membrane is determined by the relative humidity values in the anode and cathode. At the

operating conditions where the cathode inlet RH is 50%, the RH in the anode channels and in the cathode channels increase with flow direction, mainly from the top to the bottom of the active area. If the cathode flow direction is placed opposite to the anode flow direction, the overall water content in the membrane will be more even due to the humid reactants in the downstream. When a humidifier is not available, counter-flow field design is a better solution.

	Case 1	Case 2
Current density distribution (%)	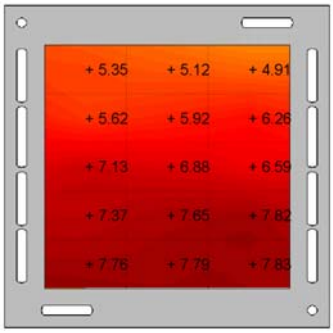 (a)	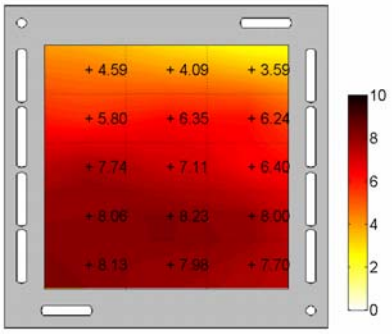 (b)
Water content	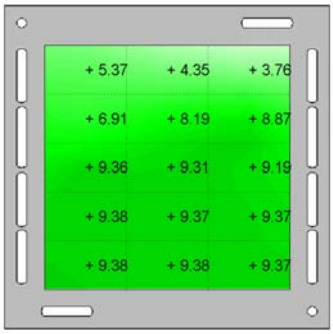 (c)	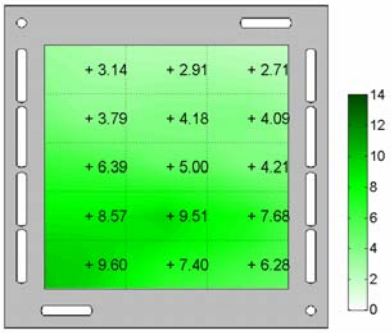 (d)
Anode RH (%)	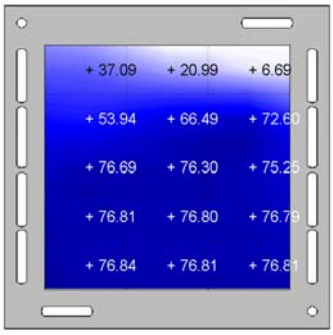 (e)	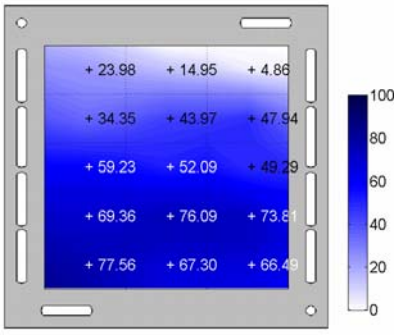 (f)
Cathode RH (%)	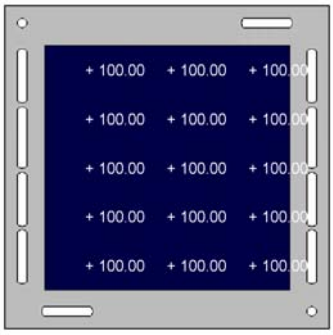 (g)	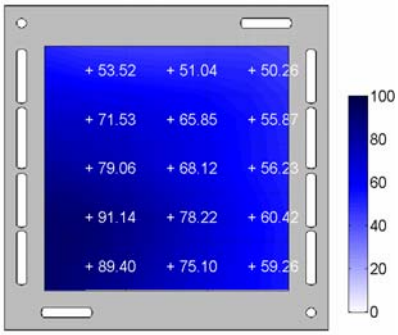 (h)

Figure 4-9: Distribution of current density, water content in the membrane, relative humidity in the anode channel, and relative humidity in the cathode channel. Left figures: case 1. Right figures: case 2. (Cell No. 2)

	Case 1	Case 2
Current density distribution (%)	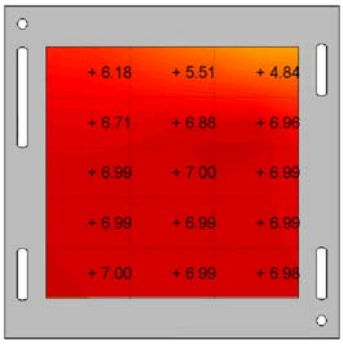 (a)	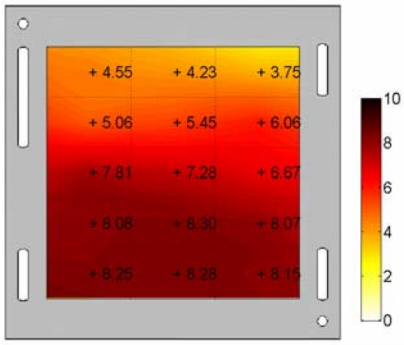 (b)
Water content	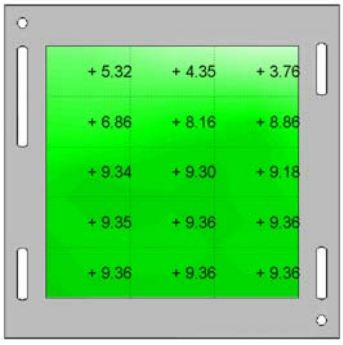 (c)	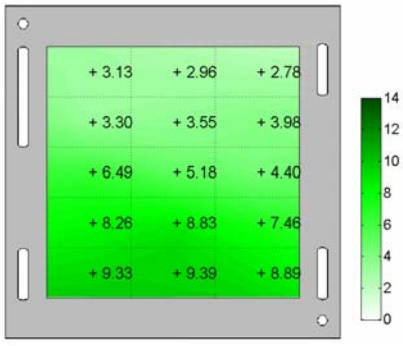 (d)
Anode RH (%)	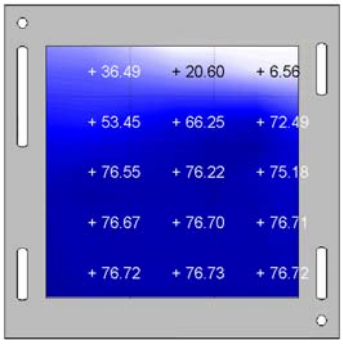 (e)	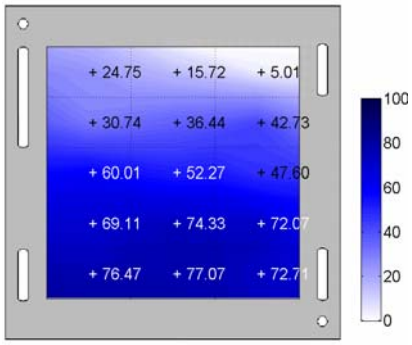 (f)
Cathode RH (%)	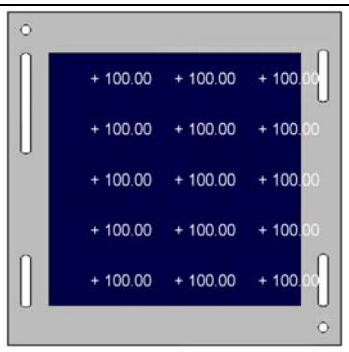 (g)	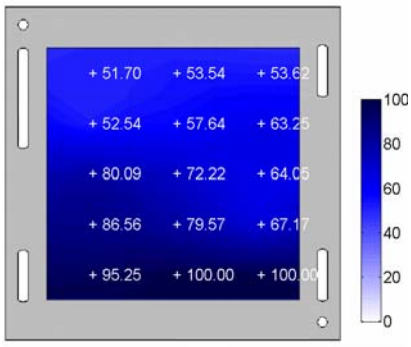 (h)

Figure 4-10: Distribution of current density, water content in the membrane, relative humidity in the anode channel, and relative humidity in the cathode channel. Left figures: case 1. Right figures: case 2. (Cell No. 3)

In portable fuel cell systems or transportation applications, where there is no space for humidifiers, an appropriate flow field design is the only mechanism to increase the system efficiency. Under the circumstances where the humidifier cannot work efficiently or humidifier is not available in the system, generated water within the fuel cell should be used effectively to humidify the membrane internally. In the flow pattern design of cells No. 1, No. 2, and No. 3, both the anode and cathode reactants move from the top to the bottom. We designed a virtual cell No. 4 in which the cathode inlet is placed at the bottom of the active area and the anode flow direction is kept the same with other cells, as shown in Figure 4-11. The performance and water accumulation in this design will be predicted by our segmented model and compared with other designs.

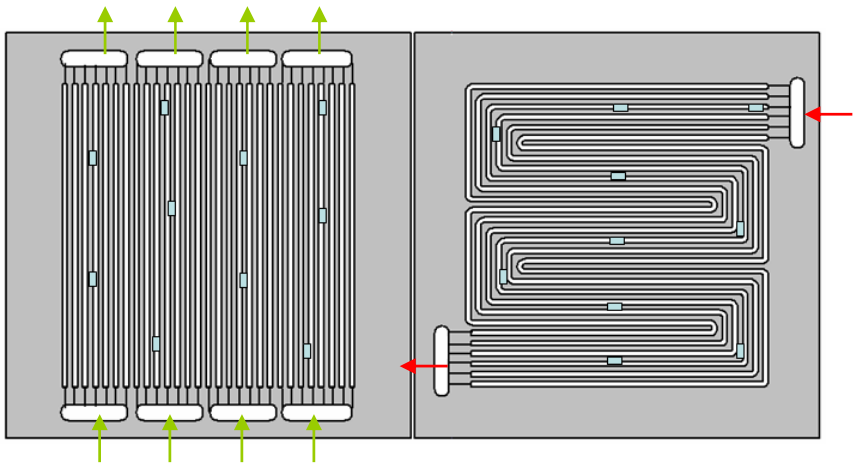

Figure 4-11 : Flow field pattern of cell No. 4. Left: the cathode inlet is placed at the bottom of the active area. Right: the anode inlet is on the up right corner.

	Case 1	Case 2
Current density distribution (%)	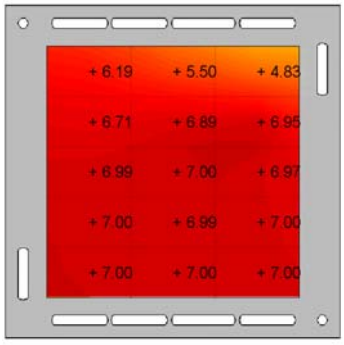 (a)	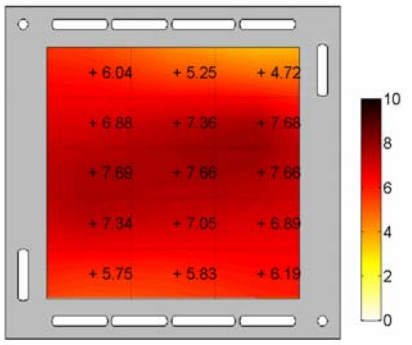 (b)
Water content	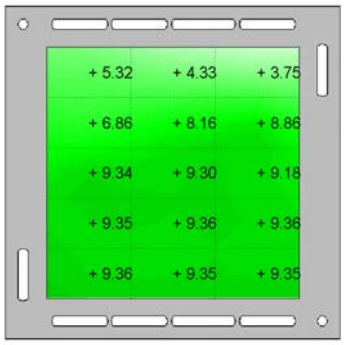 (c)	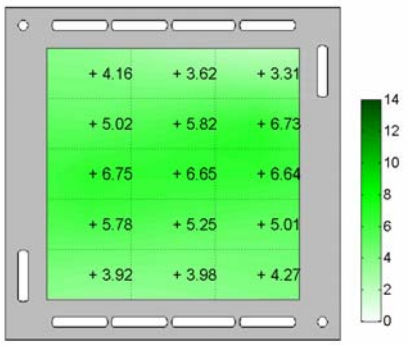 (d)
Anode RH (%)	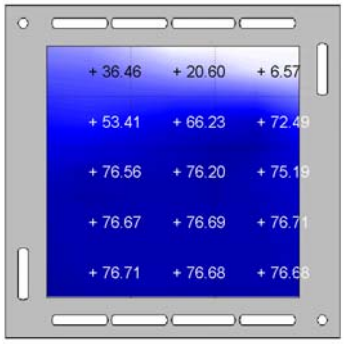 (e)	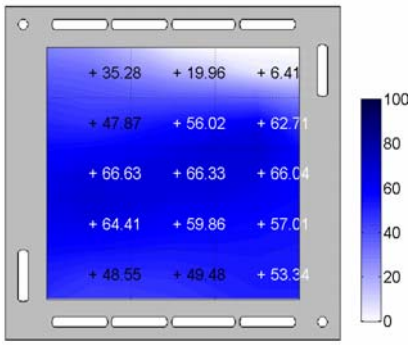 (f)
Cathode RH (%)	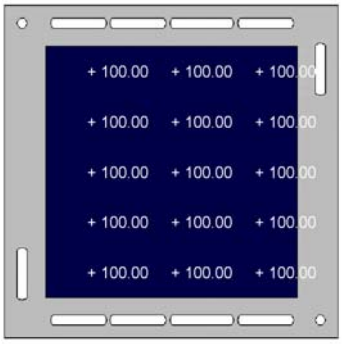 (g)	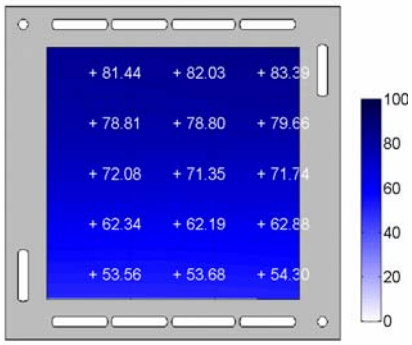 (h)

Figure 4-12: Distribution of current density, water content in the membrane, relative humidity in the anode channel, and relative humidity in the cathode channel. Left figures: case 1. Right figures: case 2. (Cell No. 4)

Figure 4-12 shows the modeling results of cell No. 4. In Case 1, where the cathode inlet RH is 100%, the distributions of current density and water content in the membrane are similar to those of cell No. 1 to cell No. 3 at the same operating condition. However, when the cathode inlet RH is 50%, the current density (4.72%) near the anode inlet is higher compared to that in cells No. 1 (3.90%), No. 2 (3.59%), and No. 3 (3.75%). The current densities at the bottom segments are lower because the under-saturated cathode reactant is fed from the bottom of the cell. The maximum current density appears in the middle part of the active area, as shown in Figure 4-12(b), and the distribution is more even. Water content in the membrane shows similar trend as current density distribution, as shown in Figure 4-12(d). The performance of these four flow pattern designs were compared in Figure 4-13. There is no significant difference when cathode inlet RH is 100%. When RH of cathode inlet is 50%, cell No. 4 shows higher performance than the other cells at high current density. This is due to the humid cathode reactant near the outlet, resulting in increasing the water content of the membrane.

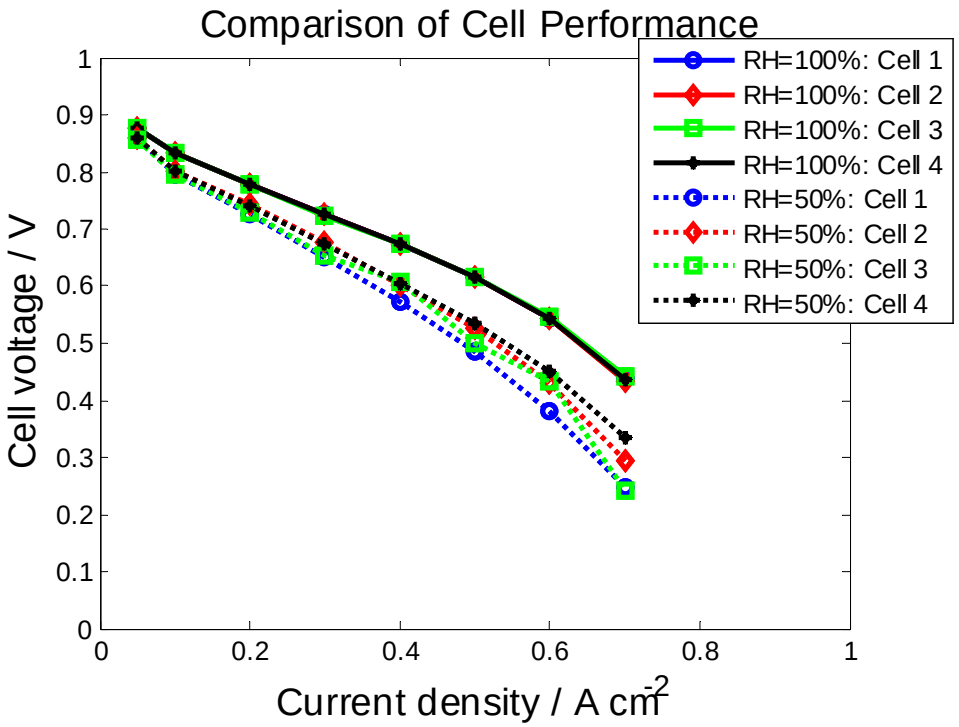

Figure 4-13: Comparison of cell performance of four single cells.

4.5 Comparison between Modeling and Experimental Results

Figure 4-14, Figure 4-15, and Figure 4-16 compare the experimental data from RH sensors and modeling results of RH distribution in the flow channel for cell No. 3. Figure 4-14(c) shows that at high current density anode RH near the downstream area is lower than at low current density, as shown in Figure 4-14(b). The reason is possibly due to the higher dry hydrogen flow rate at high current density, resulting in decreased RH in the down stream. The experimental data supports the modeling results, as shown in Figure 4-14(c). In Figure 4-15, when the cathode inlet RH is 50%, the modeling results also show good agreement with experimental results.

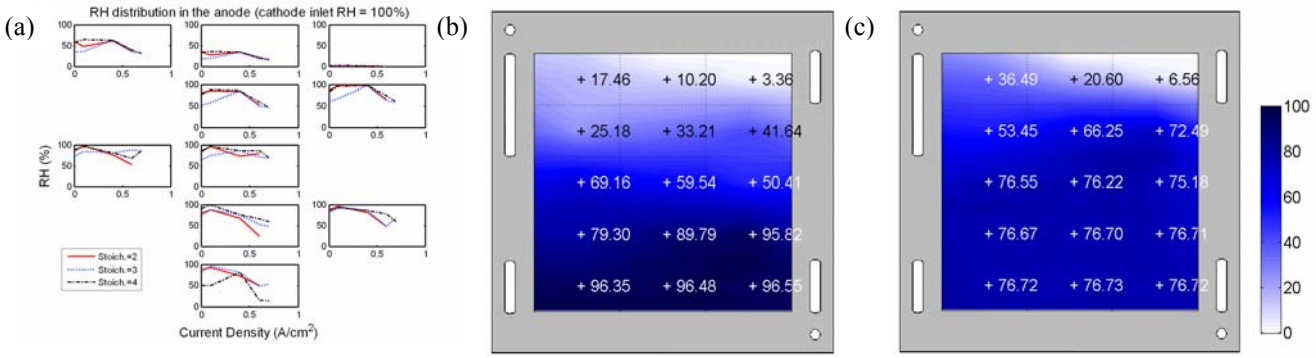

Figure 4-14: RH in the anode flow channels when cathode inlet RH is 100% (cell No. 3) (a) experimental results; (b) modeling results when current density is 0.1 A/cm^2 ; (c) modeling results when current density is 0.7 A/cm^2

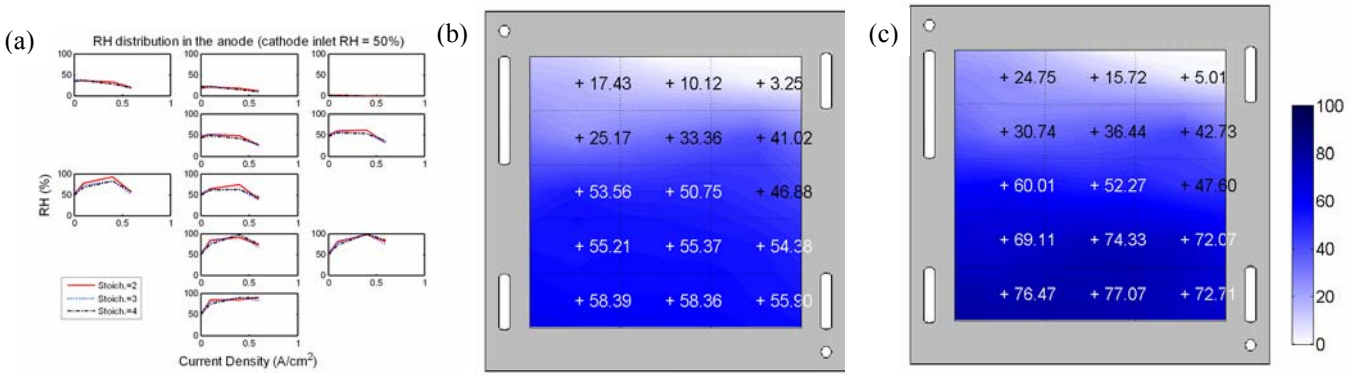

Figure 4-15: RH in the anode flow channels when cathode inlet RH is 50% (cell No. 3) (a) experimental results; (b) modeling results when current density is 0.1 A/cm^2 ; (c) modeling results when current density is 0.6 A/cm^2

In Figure 4-16(b), at low current density the RH in the cathode channels also shows similar results as experimental data. However, at high current density in Figure 4-16(c), the RH in the down stream area shows 100% in modeling results but shows around 60% in experimental data. A possible reason is that we assumed that in our model liquid water moves at the same velocity as gas, so there is some liquid water in the downstream area of the cathode channels. However, because channel number is reduced from twelve to six, gas velocity in the downstream channels increases, resulting in quick removal of liquid water. Besides, the under-saturated cathode gas also contributes to lower RH in the downstream channels.

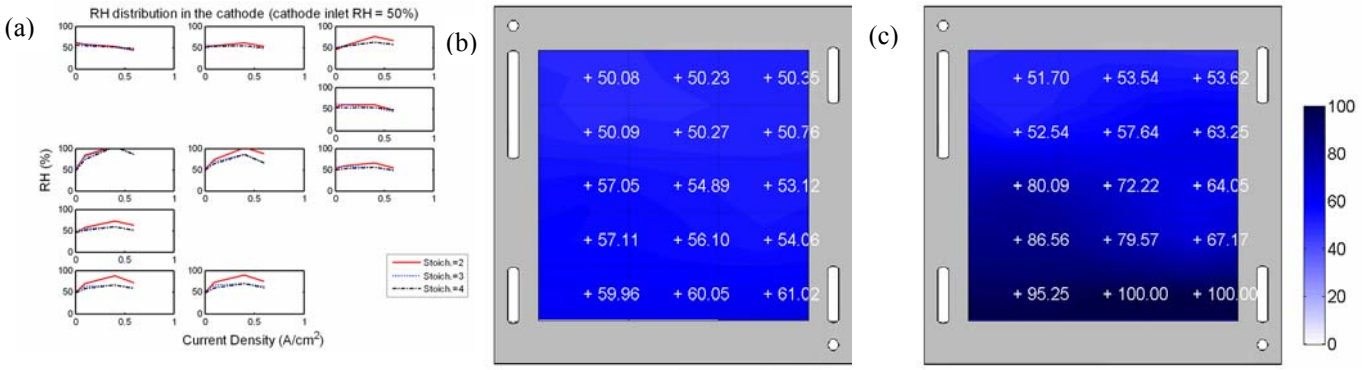

Figure 4-16: RH in the cathode flow channels when cathode inlet RH is 50% (cell No. 3) (a) experimental results; (b) modeling results when current density is 0.1 A/cm^2 ; (c) modeling results when current density is 0.6 A/cm^2

Figure 4-17 and Figure 4-18 compare modeling results and experimental data of water distribution for cells No. 2 and No. 3, respectively. In Figure 4-17, modeling results agree with experimental data for most of the operating conditions, except for low current densities. In Figure 4-18, this model successfully predicts water accumulation in the majority of segments for most of the operating conditions. The variation between modeling results and experimental data could be due to a few different reasons. First, the model parameters were calibrated based on the experimental data of cell No. 1. The influence of flow field patterns was not considered for the parameters. Second, the experimental data of water accumulation was quantified "indirectly" by using least-squares method. An improved experimental design to "directly" measure water accumulation in the GDL is needed for accuracy.

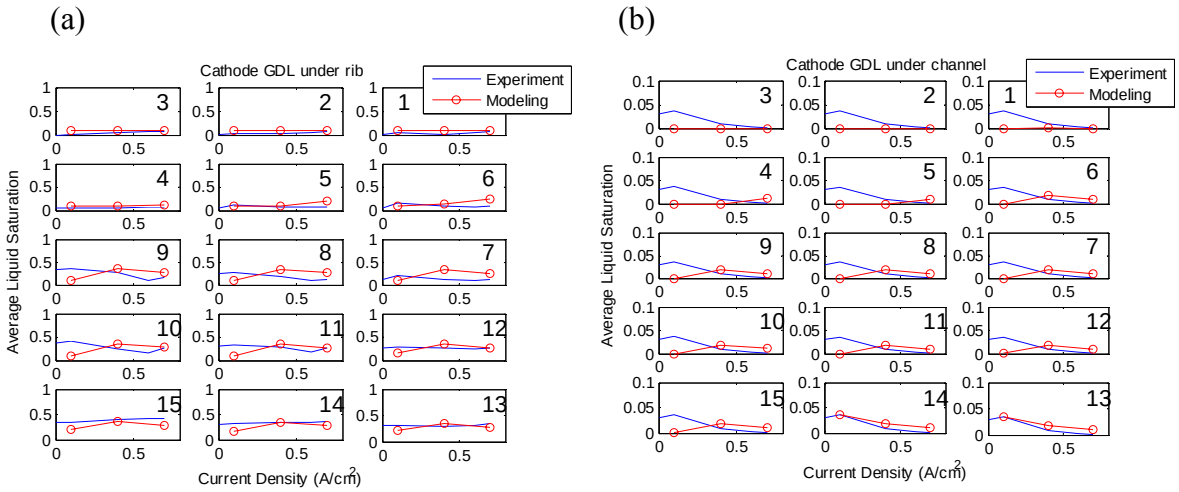

Figure 4-17: Comparison of modeling result and experimental data (Cell No.2)

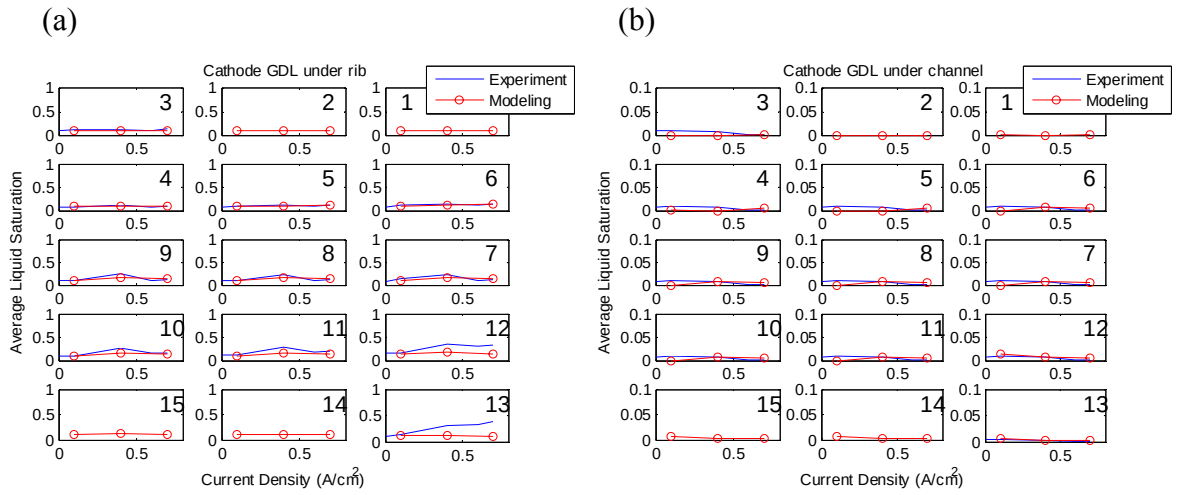

Figure 4-18: Comparison of modeling result and experimental data (Cell No.3)

When we developed the mathematical models for cells No. 2 and No. 3, we reconnected segments according to flow field patterns without changing parameter values listed in Table 4.3. However, some of these parameter values may vary from design to design. If we want to apply this model to a fuel cell with different materials or designs, these parameter values need to be calibrated according to materials or designs. In Table 4.3 the contact resistance R_{contact} is mainly influenced by compression force and contacting surface roughness of components of fuel cells [88-89]. The compression force also affects porosities of GDLs, which influences values of α, β, and γ. GDLs with

different materials, porosities, and hydrophobicity also have different values of α, β, and γ. In this model, b_{11}, b_{12}, and b_{13} are calibrated to calculate membrane conductivity. If a different membrane is used in a fuel cell, b_{11}, b_{12}, and b_{13} need to be readjusted. Accordingly, the values of R_{contact}, α, β, γ, b_{11}, b_{12}, and b_{13} are MEA dependant. If we want to apply this model to describe the performance of fuel cells with different MEAs, we need to calibrate the values of R_{contact}, α, β, γ, b_{11}, b_{12}, and b_{13}. If we use this model to describe fuel cells with the same MEA but different flow field designs, there is no need to adjust these values; e.g., models of cells No. 2 and No. 3 in this study.

In summary, this segmented single cell model provides distributed information of current density, water accumulation, water content in the membrane, and relative humidity in the flow channels. Durability of PEMFCs and life of the membrane depend on the level of flooding and drying within a fuel cell. They can be improved by appropriate flow field design. The concept of this model can be used to investigate the performance or distributed properties of different flow field designs by reconnecting the segments.

CHAPTER 5
CONCLUSIONS AND FUTURE WORKS

In this study, we developed a segmented model to study water transport in a PEM fuel cell. This model captures the distributions of current density, water accumulation in the GDL, water content in the membrane, and RH in the flow channels. To calibrate this model, we conducted experiments under selected operating conditions. We designed three single cells each with 20 embedded miniature temperature and relative humidity sensors. The results have been reported in the earlier chapters and the major conclusions are summarized below.

5.1 Conclusions of Neutron Experiments

Neutron radiography provides a non-destructive and valuable measurement technique to quantify and visualize liquid water in a working PEMFC. Three single cells with shifted flow field designs as well as imaging mask techniques were used to differentiate liquid water in four types of channel/rib combinations, anode channel/cathode channel, anode rib/cathode rib, anode channel/cathode rib, and cathode channel/anode rib. By applying the least-squares method, we are able to calculate average liquid water thicknesses in the GDL under the channel, in the GDL under the ribs, and in the channels. In this study, both steady-state and transient behaviors of water accumulation were studied at different cathode inlet conditions.

The influence of cathode inlet RH and stoichiometry values on liquid water accumulation and distribution was investigated in this study. The RH of cathode inlet was shown to have a substantial effect on liquid water accumulation in the GDLs. The steady-state experimental results showed that liquid water has a tendency to accumulate in the GDL under the rib and the amount varies with current densities. The average liquid

saturation in the GDL under the rib was found to vary from 0.05 to 0.5 and that in the GDL under channel is about 0.02, which is lower than modeling results in the literature. The RH in each segment increases with increasing current density due to water generation. At high current density, RH values decrease slightly. This could be due to the high flow rate of unsaturated gas. Moreover, temperature difference between segments can be neglected regardless of the stoichiometric values and cathode inlet RH.

The transient behavior of water transport was studied by capturing neutron images and RH in the flow channels. The channel-reduced design in the cathode helps gas flow carry liquid water to the outlet without causing flooding in the GDLs. In addition, RH in the anode channel quickly increases with flow distance and reaches saturation even when the cathode RH is unsaturated. At high current density, RH in the anode channel decreases due to the higher dry anode gas flow rate. The temperature distributes uniformly within the active area and has large response time with respect to load change. The experimental results provide useful information for subsequent model calibration and validation.

5.2 Conclusions of Segmented Model

We developed the governing equations for a 15-segment fuel cell model. Each segment is viewed as a lumped element, which consists of six interacting sub-models, and is connected based on the reactant flow directions. This model is calibrated based on experimental results and is able to describe liquid water saturation in the GDL under the channel and in the GDL under the rib. The calibrated model was used to investigate distributions of current density, water content in the membrane, RH in the anode/cathode, and water accumulation in the GDL under the channel/rib as well as water transport in the MEA.

Modeling results show that cathode inlet RH has significant influence on the uniformity of water content in the membrane and current density. At low cathode inlet humidity and high load, the maximum local current density is twice that of the minimum local current density. Cathode humidity has less influence on the uniformity of current density at low current load. In this study, the influence of water accumulation on current

density is not obvious. That could be due to un-humidified hydrogen, short flow channels, and operating current density. In the GDL under the rib, the minimum liquid saturation is observed at segments near the cathode inlet, and increases toward the outlet. The maximum liquid saturation is near the cathode outlet and is approximately 0.4. The RH of anode flow gas also affects the liquid saturation in the cathode GDL under the rib. However, the cell performance is more significantly influenced by the cathode inlet RH.

The segments in this model can be reconnected according to flow field patterns to predict distributed properties within throughout the flow field, including water content in the membrane, water transport across the MEA, and liquid saturation in the GDLs. The results show current density and the amount of water transport influence with each other. This result also provides useful information in placing the inlet/oulet of anode/cathode when we design flow field patterns. Modeling results suggest that opposite flow direction improve the cell performance at low humidity conditions. Accordingly, this segmented model is useful in designing flow field patterns and comparing the influence of different flow field patterns before they are machined on the flow field plates. That reduces the cost of developing and designing a fuel cell.

5.3 Recommendations for Future Works

In this study relative humidity and temperature in the flow channels were detected by 20 embedded sensors. Relative humidity sensors cannot detect liquid water within the fuel cell, but they can imply the drying areas of the proton exchange membrane. In most cases drying is highly possible to happen near the gas inlet areas. Thus, for the future designs, we don't need to install so many sensors and they can be mainly placed near the inlet areas.

We designed a "shifted" flow field and used least-squares method to differentiate liquid water accumulation between the anode and cathode; however, this method "indirectly" quantified liquid water in both. The novel idea of an improved work is to specially design a slender single cell so the liquid water accumulation in the GDL under the ribs and in the GDL under the channels can be separately quantified in neutron imaging. The flow channels in this newly designed slender cell would be shorter in length.

A neutron beam is expected to go through this cell along the flow channel direction so the liquid water accumulation in the GDL under the ribs and under the channels can be separately detected. By conducting this experiment, we will expect to "directly" quantify water accumulation in the GDLs under the ribs and under the channels.

The maximum current density in our single cells is 0.7 A cm^{-2} regardless of flow field patterns. The shifted flow field design may be responsible for the low current density; however, cell No. 1, where there is no shifted design, shows the similar cell performance. Thus, another possible reason could be the MEAs themselves. If the maximum current density of MEAs could reach as high as 1.2 A cm^{-2}, the influence of flow field patterns would become notable. Since we don't have information regarding the contents and manufacturing process of the MEAs, for the fuel cell experiments in the future, we can test MEAs from different companies and picked the one with best performance.

Cell performance is also influenced by flow field patterns. In the fuel cells with larger active area, the influence is more significant. With appropriate flow field designs, generated liquid water can be utilized to humidify the membrane, resulting in increasing conductivity and cell performance. That can be achieved by counter-flow designs. When designing flow field patterns for fuel cell stacks with larger active areas, we also need to consider the coolant flow patterns.

In a fuel cell stack, in which many cells are connected in series, the heat flow of a MEA is influenced by other MEAs in neighboring cells. Thus, cell temperature cannot be assumed uniformly distributed. In the future, we could include a thermal model in our segmented model and extend our single cell model to fuel cell stack model. With the stack model, we should be able to analyze the flow distribution in a fuel cell stack, perform thermal analysis, and estimate the average cell temperature, localized hot and cold spots in a cell. This model is expected to provide useful information for the design of cooling system and control algorithms.

APPENDIX

Nomenclature

a	water vapor activity
A	area (m^2)
c	concentration (mol m^{-3})
d	hydraulic diameter (m)
D_{i-j}	diffusivity of gas pair *i-j* in a mixture (m^2 s^{-1})
F	Faraday's constant (96485 C equivalent^{-1})
H	channel depth (m)
i	current density (A cm^{-2})
I	current (A)
I_0	Exchange current (A)
K	permeability of GDL (m^2)
$K_{osmotic}$	electro osmotic drag coefficient
K_{diff}	back diffusion coefficient (mol s m^{-2})
K_{conv}	coefficient of convective mass transfer (mol s m^{-2})
L	channel length (m)
M	equivalent weight of a dry membrane (kg mol^{-1})
N	molar flow rate (mol s^{-1})
P	pressure (Pa)
Q	gas volume flow rate (m^3 s^{-1})
R	universal gas constant (8.314 J mol^{-1} K^{-1})
R_j	resistance of component *j* (Ω)
s	liquid saturation
Sh	Sherwood number
t	thickness (m)
T	temperature (K)
V	voltage (V)
W	channel or rib width (m)
x_j	mole fraction of species *j*
Z	channel number in a segment

Greek

α_c	cathodic transfer coefficient
ε	porosity of gas diffusion layer
ζ	stoichiometry of gas
λ	water content
μ	dynamic viscosity (kg m^{-1} s^{-1})
ρ	density (kg m^{-3})
σ	electrical conductivity (Ω^{-1} m^{-1})
φ	relative humidity

Subscripts

an	anode
act	activation
avg	average
c	critical
ca	cathode
c/g	channel and gas diffusion layer interface
ch	channel
contact	contact
conc	concentration
gdl	gas diffusion layer
g/m	gas diffusion layer and membrane interface
H_2	hydrogen
H_2O	water
in	inlet
limit	limit
N_2	nitrogen
ohm	ohmic
out	outlet
O_2	oxygen
p	pore

pem	proton exchange membrane
plate	plate
sat	saturation
seg	segment
v	water vapor
w	liquid water

BIBLIOGRAPHY

1. D.M. Bernardi and M.W. Verbrugge. Mathematical model of a gas diffusion electrode bonded to a polymer electrolyte. *AIChE J.*, 37 (1991) 1151-1163.
2. D.M. Bernardi and M.W. Verbrugge. A mathematical model of the solid-polymer-electrolyte fuel cell. *J. Electrochem. Soc*., 139 (1992) 2477-2491.
3. T. Okada, G. Xie, M. Meeg. Simulation for water management in membranes for polymer electrolyte fuel cells. *Electrochimica Acta*, 43 (1998) 2141-2155.
4. C. Marr, X. Li. Composition and performance modeling of catalyst layer in a proton exchange membrane fuel cell. *J. Power sources*, 77 (1999) 17-27.
5. T.E. Springer, T.A. Zawodzinski, S. Gottesfeld. Polymer electrolyte fuel cell model. *J. Electrochem. Soc*., 138 (1991) 2334-2342.
6. T.F. Fuller and J. Newman. Water and thermal management in solid-polymerelectrolyte fuel cells. *J. Electrochem. Soc*., 140 (1993) 1218-1225.
7. V. Gurau, H. Liu, S. Kakac. Two-dimensional model for proton exchange membrane fuel cells. *AIChE J.*, 44 (1998) 2410-2422.
8. C.Y. Wang, W.B. Gu, B.Y. Liaw. Micro-macroscopic coupled modeling of batteries and fuel cells. *J. Electrochem. Soc.*, 145 (1998) 3407-3417.
9. S. Um, C.Y. Wang, K.S. Chen. Computational Fluid Dynamics Modeling of Proton Exchange Membrane Fuel Cells. *J. Electrochem. Soc*., 147 (2000) 4485-4493.
10. S. Um, C.Y. Wang, K.S. Chen. Three-dimensional analysis of transport and electrochemical reactions in polymer electrolyte fuel cells. *J. Power sources*, 125 (2004) 40-51.
11. J.J. Baschuk, X. Li. Modeling of polymer electrolyte membrane fuel cells with variable degrees of water flooding. *J. Power Sources,* 86 (2000) 181-196.
12. Z.H. Wang, C.Y. Wang, K.S. Wang. Two-phase flow and transport in the air cathode of proton exchange membrane fuel cells. *J. Power Sources*, 94 (2001) 40-50.
13. U. Pasaogullari, C.Y. Wang. Liquid water transport in gas diffusion layer of polymer electrolyte fuel cells. *J. Electrochem. Soc*., 151 (2004) A399-A406.
14. D. Natarajan, T.V. Nguyen. A two-dimensional, two-phase, multicomponent, transient model for the cathode of a proton exchange membrane fuel cell using conventional gas distributor. *J. Electrochem. Soc*. 148 (2001) A1324-A1335.
15. D. Natarajan and T.V. Nguyen. Three-dimensional effects of liquid water flooding in

the cathode of a pem fuel cell. *J. Power Sources*, 115 (2003) 66-80.

16. G. Lin and T.V. Nguyen. A two-dimensional two-phase model of a pem fuel cell. *J. Electrochem. Soc*., 153 (2006) A372-A382.
17. A. Turhan, K. Heller, J.S. Brenizer, M.M. Mench. Quantification of liquid water accumulation and distribution in a polymer electrolyte fuel cell using neutron imaging. *J. Power Sources*, 160, (2006) 1195-1203.
18. J. Zhang, D. Kramer, R. Shimoi, Y. Ono, E. Lehmann, A. Wokaun, K. Shinohara and G. G. Scherer. In situ diagnostic of two-phase flow phenomena in polymer electrolyte fuel cells by neutron imaging Part B. Material variations. *Electrochim. Acta*, 51 (2006) 2715-2727.
19. S. Maharudrayya, S. Jayanti, A.P. Deshpande. Pressure drop and flow distribution in multiple parallel-channel configurations used in proton-exchange membrane fuel cell stacks. *J. Power Sources*, 157 (2006) 358-367.
20. S. Shimpalee, S. Greenway, J.W. Van Zee. The impact of channel path length on pemfc flow-field design. *J. Power Sources*, 160 (2006) 398-406.
21. X. Liu, H. Guo, F. Ye, C.F. Ma. Water flooding and pressure drop characteristics in flow channels of proton exchange membrane fuel cells. *Electrochim. Acta*, 52 (2007) 3607-3614.
22. W. Ying, T.-H. Yang,W.-Y. Lee, J. Ke, C.-S. Kim. Three-dimensional analysis for effect of channel configuration on the performance of a small air-breathing proton exchange membrane fuel cell (pemfc). *J. Power Sources*, 145 (2005) 572-581.
23. J.C. Amphlett, R.F. Mann, B.A. Peppley, P.R. Roberge, A. Rodrigues. A model predicting transient responses of proton exchange membrane fuel cells. *J. Power Sources*, 61 (1996) 183-188.
24. J. T. Pukrushpan, A. G. Stefanopoulou, H. Peng. Control of fuel cell breathing. *IEEE control Systems Magazine*, 24 (2004) 30-46.
25. Y. Shan, S.Y. Choe. A high dynamic PEM fuel cell model with temperature effects. *J. Power Sources*, 145 (2005) 30-39.
26. H. Nishikawa, R. Kurihara, S. Sukemori, T. Sugawara, H. Kobayasi, S. Abe, T. Aoki,Y. Ogami, A. Matsunaga. Measurements of humidity and current distribution in a pefc. *J. Power Sources*, 155 (2006) 213-218.

27. M.M. Mench, Q.L. Dong, C.Y. Wang. In situ water distribution measurements in a polymer electrolyte fuel cell. *J. Power Sources*, 124 (2003) 90-98.
28. K. Tüber, D. Pócza, C. Hebling. Visualization of water buildup in the cathode of a transparent pem fuel cell. *J. Power Sources*, 124 (2005) 403-414.
29. R.J. Bellows, M.Y. Lin, M. Arif, A.K. Thompson, D. Jacobson. Neutron imaging technique for in situ measurement of water transport gradients within nafion in polymer electrolyte fuel cells. *J. Electrochemical Society*, 146 (1999) 1099-1103.
30. R. Satija, D.L. Jacobson, M. Arif, S.A. Werner. In situ neutron imaging technique for evaluation of water management systems in operating pem fuel cells. *J. Power Sources*, 129 (2004) 238-245.
31. D. Kramer, J. Zhang, R. Shimoi, E. Lehmann, A. Wokaun, K. Shinohara, G.G. Scherer. In situ diagnostic of twophase flow phenomena in polymer electrolyte fuel cells by neutron imaging part a. experimental, data treatment, and quantification. *Electrochimica Acta*, 50 (2005) 2603-2614.
32. D. Kramer, E. Lehmann, G. Frei, P. Vontobel, A. Wokaun, G.G. Scherer. An online study of fuel cell behavior by thermal neutrons. *Nuclear Instruments and Methods in Physics Research*, A 542 (2005) 52-60.
33. N. Pekula, K. Heller, P.A. Chuang, A. Turhan, M.M. Mench, J.S. Brenizer, K. Ünlü, Study of water distribution and transport in a polymer electrolyte fuel cell using neutron imaging. *Nuclear Instruments and Methods in Physics Research*, A 542 (2005) 134-141.
34. P.A. Chuang, A. Turhan, A.K. Heller, J.S. Brenizer, T.A. Trabold, M.M. Mench. The nature of flooding and drying in polymer electrolyte fuel cells. *In Proceedings of FUELCELL*, 2005.
35. D.J. Ludlow, C.M. Calebrese, S.H. Yu, C.S. Dannehy, D.L. Jacobson, D.S. Hussey, M. Arif, M.K. Jensen, G.A. Eisman. PEM fuel cell membrane hydration measurement by neutron imaging. *J. Power Sources*, 162 (2006) 271-278.
36. A.B. Geiger, A. Tsukada, E. Lehmann, P. Vontobel, A. Wokaun, G.G. Scherer. In situ investigation of two-phase flow patterns in flow fields of pefcs using neutron radiography. *Fuel Cells*, 2 (2002) 92-98.
37. T.A. Trabold, J.P. Owejan, D.L. Jacobson, M. Arif, P.R. Huffman. In situ

investigation of water transport in an operating pem fuel cell using neutron radiography: Part 1 - experimental method and serpentine flow field results. *Int. J. Heat and Mass Transfer*, 49 (2006) 4712-4720.

38. J.P. Owejan, T.A. Trabold, D.L. Jacobson, D.R. Baker, D.S. Hussey, and M. Arif. In situ investigation of water transport in an operating pem fuel cell using neutron radiography: Part 2 - transient water accumulation in an interdigitated cathode flow field. *Int. J. Heat and Mass Transfer*, 49 (2006) 4721-4731.
39. M.A. Hickner, N.P. Siegel, K.S. Chen, N.D. McBrayer, D.S. Hussey, D.L. Jacobson, M. Arif. Real-time imaging of liquid water in an operating proton exchange membrane fuel cell. *J. Electrochem. Soc*., 153 (2006) A902-A908.
40. J. T. Pukrushpan. Modeling and Control of PEM Fuel Cell Systems and Fuel Processors. *Ph.D. Dissertation*. University of Michigan, 2003.
41. M. Ceraolo, C. Miulli, A. Pozio. Modelling static and dynamic behaviour of proton exchange membrane fuel cells on the basis of electro-chemical description. *J. Power Sources*, 113 (2003) 131-144.
42. P.R. Pathapati, X. Xue and J. Tang. A new dynamic model for predicting transient phenomena in a PEM fuel cell system. *Renewable Energy*, 30 (2005) 1-22.
43. J. Golbert and D.R. Lewin. Model-based control of fuel cells: (1) Regulatory control. *J. Power Sources*, 135 (2004) 135-151.
44. US Patent: 5981098. 1999.
45. US Patent: 5776624. 1998.
46. A.S. Aricò, P. Cretì, V. Baglio, E. Modica, V. Antonucci. Influence of flow field design on the performance of a direct methanol fuel cell. *J. Power Sources*, 91 (2000) 202-209.
47. H. Dohle, T. Bewer, J. Mergel, R. Hetzel, D. Stolten. Evaluation of flow field designs for use in pem and dmfc fuel cells. In Proceedings of fuel cell seminar, pp 130-133, Portland, OR, 2000.
48. T. Bewer, T Beckmann, H. Dohle, J Mergel, D. Stolten. Evaluation and optimisation of flow distribution in pem and dmfc fuel cells. In Proceedings of the First European PEFC forum (EFCF), pp 321-330, 2001.
49. T. Bewer, T Beckmann, H. Dohle, J Mergel, D. Stolten. Novel method for

investigation of two-phase flow in liquid feed direct methanol fuel cells using an aqueous H_2O_2 solution. *J. Power Sources*, 125 (2004) 1-9.

50. R.G. Reddy A. Kumar. Effect of gas flow-field design in the bipolar/end plates on the steady and transient state performance of polymer electrolyte membrane fuel cells. *J. Power Sources*, 155 (2006) 264-271.
51. M. Wang, H. Guo, C. Ma, J. Power Sources, 157 (2006) 181-187.
52. R.E. Sonntag, C. Borgnakke, G.J. Van Wylen. *Fundamentals of Thermodynamics*. John Wiley & Sons Inc, sixth edition, 2002.
53. R.W. Fox, A.T. McDonald. Introduction to Fluid Mechanics. John Wiley & Sons, Inc, New York, USA, 1994.
54. J. Benitez. Principles and Modern Applications of Mass Transfer Operations. John Wiley & Sons, Inc, New York, USA, 2002.
55. T. E. Springer, M. S. Wilson, and S. Gottesfeld. Modeling and Experimental Diagnostics in Polymer Electrolyte Fuel Cells. *J. Electrochem. Soc.*, 140 (1993) 3513-3526.
56. W.M. Rohsenow, J.P. Hartnett, Y.I. Cho. Handbook of Heat Transfer. McGraw-Hill, New York, 3rd edition, 1998.
57. J.S. Yi, T.V. Nguyen, Multicomponent transport in porous electrodes of proton exchange membrane fuel cells using the interdigitated gas distributors, *J. Electrochem. Soc*. 146 (1999) 38-45.
58. W.H. He, J.S. Yi, T.V. Nguyen. Two-phase flow of the cathode of pem fuel cells using interdigitated flow fields, *AIChE J*. 46 (2000) 2053-2064.
59. G. Lin, W. He, T.V. Nguyen, Modeling Liquid Water Effects in the Gas Diffusion and Catalyst Layers of the Cathode of a PEM Fuel Cell, *J. Electrochemical Soc.* 151 (2004) A1999-A2006.
60. G. Squadrito, G. Maggio, E. Passalacqua, F. Lufrano and A. Patti. An empirical equation for polymer electrolyte fuel cell (PEFC) behaviour. *J. of Applied Electrochemistry*. 29 (1999) 1449-1455.
61. M.M. Mezedur, M. Kaviany, W. Moore, Effect of pore structure, randomness and size on effective mass diffusivity, *AIChE J*. 48 (2002) 15-24.
62. J.H. Nam and M. Kavinay. Effective diffusivity and water-saturation distribution in

single- and two-layer PEMFC diffusion medium. *Int. J. Heat and Mass Transfer*. 46 (2003) 4595-4661.

63. T.F. Fuller, J. Newman. Water and thermal management in solid-polymer-electrolyte fuel cells. *J. Electrochem. Soc*., 139 (1992) 1332-1339.
64. T.A. Zawodzinski, S. Radzinski, R.J. Sherman, V.T. Smith, T.E. Springer, S. Gottesfeld. Water uptake by and transport through nafion 117 membranes. *J. Electrochem. Soc*., 140 (1993) 1041-1047.
65. G. Xie, T. Okada. Water transport behavior in nafion 117 membranes. *J. Electrochem. Soc*., 142 (1995) 3057-3062.
66. T.A. Zawodzinski, J. Davey, J. Valerio, S. Gottesfeld. The water content dependence of electro-osmotic drag in proton-conducting polymer electrolytes. *Electrochim. Acta*, 40 (1995) 297-302.
67. S. Dutta, S. Shimpalee, J.W. Van Zee. Numerical prediction of massexchange between cathode and anode channels in a pem fuel cell. International *Int. J. Heat and Mass Transfer*, 44 (2001) 2029-2042.
68. J. Larminie and A. Dicks, Fuel cell Systems Explained, Wiley, 2003.
69. A.J. Appleby and F.R. Foulkes, Fuel Cell Handbook, Van Nostrand Reinhold, New York, 1989.
70. S. Miachon and P. Aldebert, Internal Hydration H_2/O_2 100 cm^2 polymer electrolyte membrane fuel cell, *J. Power Sources*, 56 (1995) 31-36.
71. J.H. Lee, T.R. Lalk, A.J. Appleby. Modeling electrochemical performance in large scale proton exchange membrane fuel cell stacks. *J. Power Sources*, 70 (1998) 258-268.
72. H. Xi. Dynamic Modeling and Control Planar SOFC Power Systems. *Ph.D. Dissertation*. University of Michigan, 2006.
73. D. S. Hussey, D.L. Jacobson, M. Arif, P. R. Huffman, R. E. Williams, J. C. Cook. New neutron imaging facility at the NIST. *Nucl. Instrum. Meth. Phys. Res. A*, 542 (2005) 9-15.
74. Z. Liu, Z. Mao, B. Wu, L. Wang, V. M. Schmidt. Current density distribution in PEFC. *J. Power Sources*, 141 (2005) 205-210.
75. I.A. Schneider, D. Kramer, A. Wokaun, G.G. Scherer. Spatially resolved

characterization of PEFCs using simultaneously neutron radiography and locally resolved impedance spectroscopy. *Electrochemistry Communications,* 7 (2005) 1393-1397.

76. M.Y. El-Sharkh, A. Rahman, M.S. Alam, P.C. Byrne, A.A. Sakla, T. Thomas. A dynamic model for a stand-alone PEM fuel cell power plant for residential applications. *J. Power Sources*, 138 (2004) 199-204.
77. S. Yoshioka, A. Yoshimura, H. Fukumoto, O. Hiroi, H. Yoshiyasu. Development of a PEFC under low humidified conditions. *J. Power Sources*, 144 (2005) 146-151.
78. P.C. Ghosh, T. Wüster,H. Dohle, N. Kimiaie, J. Mergel, D. Stolten. In situ approach for current distribution measurement in fuel cells. *J. Power Sources*, 154 (2006) 184-191.
79. N. Rajalakshmi, M. Raja, K.S. Dhathathreyan. Evaluation of current distribution in a proton exchange membrane fuel cell by segmented cell approach. *J. Power Sources*, 112 (2002) 331-336.
80. X.-G. Yang, N. Burke, C.-Y. Wang, K. Tajiri, K. Shinoharab. Simultaneous Measurements of Species and Current Distributions in a PEFC under Low-Humidity Operation. *J. Electrochem. Soc*., 152 (2005) A759-A766.
81. M. M. Mench, C. Y. Wang, M. Ishikawa. In Situ Current Distribution Measurements in Polymer Electrolyte Fuel Cells. *J. Electrochem. Soc*., 150 (2003) A1052-A1059.
82. R. Mukundan, J.R. Davey, T. Rockward, J.S. Spendelow, B.S. Pivovar, D.S. Hussey, D.L. Jacobson, M. Arif, R.L. Borup. Imaging of water profiles in pem fuel cells using neutron radiography: Effect of operating conditions and gdl composition. *ECS Transactions*, 11 (2007) 411-422.
83. A. Turhan, K. Heller, J.S. Brenizer, M.M. Mench. Passive control of liquid water storage and distribution in a PEFC through flow-field design. *J. Power Sources*, 180 (2008) 773-783.
84. S.-H. Ge, B.-L. Yi. A mathematical model for PEMFC in different flow modes. *J. of Power Sources*, 124 (2003) 1-11.
85. E. Birgersson, M. Vynnycky. A quantitative study of the effect of flow-distributor geometry in the cathode of a PEM fuel cell. *J. Power Sources*, 153 (2006) 76-88.
86. J.J. Hwang, C.H. Chaob, W.Y. Hoa, C.L. Changa, D.Y. Wang. Effect of flow

orientation on thermal-electrochemical transports in a PEM fuel cell. *J. Power Sources*, 157 (2006) 85-97.

87. P. Berg, K. Promislow, J. St. Pierre, J. Stumper, B. Wetton. Water management in PEM Fuel Cells. *J. Electrochem. Soc*., 151 (2004) A341-A353.
88. W.-K. Lee, C.-H. Ho, J.W. Van Zee, M. Murthy. The effects of compression and gas diffusion layers on the performance of a PEM fuel cell. *J. Power Sources*, 84 (1999) 45-51.
89. Y. Zhou, G. Lin, A.J. Shih, S.J. Hu. A micro-scale model for predicting contact resistance between bipolar plate and gas diffusion layer in PEM fuel cells. *J. Power Sources*, 163 (2007) 777-783.